

Investigation of Ultrafast Carrier Dynamics within Specific Regions of a Single ZnO Rod Using  
Two-Photon Microscopy

Ralph Lee House

A dissertation submitted to the faculty of the University of North Carolina at Chapel Hill in  
partial fulfillment of the requirements for the degree of Doctor of Philosophy in the Department  
of Chemistry.

Chapel Hill  
2010

Approved by  
John Papanikolas  
Nancy Thompson  
Chris Fecko  
Dorothy Erie  
Richard Superfine

## Abstract

Ralph Lee House: Investigation of Ultrafast Carrier Dynamics within Specific Regions of a Single ZnO Rod Using Two-Photon Microscopy  
(Under the direction of John M. Papanikolas)

The demand for novel optoelectronic and photonic technologies has fueled an intense research effort to synthesize and characterize nanostructured semiconductor materials with unique characteristics that lend themselves to technological innovation. However, the persistence of defects in these materials can have far reaching effects on their overall properties and remains a controversial subject. The controversy is due in part to different synthetic methods and the effect of size and shape between single structures in a population. These differences are well characterized but the effect of changing shape and size within a single structure is not. The question thus arises: Can similar heterogeneous behaviors be observed at spatially distinct locations in a single object? This dissertation is a methodical exploration of this question and our overall results show that changes in an object's shape can give rise to different behaviors within different regions of a single structure.

Zinc Oxide has emerged as an attractive candidate for a variety of applications due in part to a large second order nonlinear susceptibility, its wide band-gap and large exciton binding energy. Several other properties make it amenable to the experiments described herein and it is therefore the focus of our studies. We have used time-resolved nonlinear two-photon emission microscopy to characterize the optical properties and excited state dynamics at different locations within individual ZnO rods. We characterize the trap-emission signatures in these structures and the spatial dependence of band-edge and trap emission

within a single structure. Collectively, the results from these experiments further our understanding of how defect states affect semiconducting materials and how they differ, not only *between*, but *within* single structures. Eventually, these results will prove to be fundamentally important to many problems in nanoscience and nanotechnology and will prove useful to those wishing to understand and exploit nanoscience.

To my parents, my wife and my children.

## Acknowledgements

It is with deep gratitude that I acknowledge my mentor Dr. John Papanikolas. I have learned so much, and your contribution to my growth as a scientist has been great. Thanks also to Dr. Kyle Brennaman for answering many questions and helping out whenever needed.

Thanks to my colleagues on the project. Brian, the microscopy project has taken leaps and bounds because you are a part of it. Your contribution has been incredible and I am very appreciative. Justin, the work you have done on the software development will add so many more dimensions to our current capabilities, your contribution too, has been invaluable.

I have also had the great pleasure to work with incredibly gifted and curious undergraduates. Thanks to Abhineet Uppal for help in setting up the microscope and spearheading the initial software development. The work conducted by Chuan Zhang took our synthetic efforts to a new level and have laid the foundation for new and exciting developments. Scott Barnes has successfully refined our synthetic capabilities, giving us better insight into the growth mechanisms of our ZnO structures.

Brittany, although our projects never really overlapped, I cannot imagine what graduate school would have been without you, you are a wonderful person and I am lucky to have worked with you from the start. Stephanie, in the short time you have been in lab, you have somehow managed to make it a better place, I'm really glad you decided to join our group. Ryan, you are off to a great start, your sense of dedication will carry you far.

How lucky I am to have had the opportunity to work with such a great group of people.

## Table of Contents

List of Figures.....	ix
List of Abbreviations and Symbols.....	xviii
<u>Chapter 1</u> Introduction .....	1
1.1 Motivation.....	2
1.2 ZnO Background.....	4
1.2.1 <i>Defect Definitions and Categories</i> .....	5
1.2.2 <i>Exciton Dynamics and Free Carrier Interactions</i> .....	8
1.3 Chapter Overview .....	10
1.4 References.....	13
<u>Chapter 2</u> An Introduction to Two-Photon and Second Harmonic Generation Microscopy..	16
2.1 Two-Photon Fluorescence .....	17
2.1.1 <i>Two-photon microscopy</i> .....	19
2.1.2 <i>Comparison of two-photon and confocal microscopy</i> .....	21
2.1.3 <i>Determining a Microscope's Resolution</i> .....	22
2.2 Second Harmonic Generation .....	24
2.2.1 <i>Noncentrosymmetry and Optical Susceptibility</i> .....	25
2.2.2 <i>Phase Matching</i> .....	28

2.2.3	<i>Second Harmonic Generation Microscopy</i> .....	29
2.2.4	<i>The Nonlinear Susceptibility Tensor Microscopy</i> .....	29
2.3	References.....	33
 <u>Chapter 3</u> Experimental Description.....		35
3.1	Microscope design .....	36
3.2	Major Components and their Specifications.....	39
3.2.1	<i>Laser Operation</i> .....	39
3.2.2	<i>The Laser System</i> .....	43
3.2.3	<i>Mode-Locking</i> .....	45
3.2.4	<i>Group Velocity Dispersion and Prism Compression</i> .....	47
3.2.5	<i>The Faraday Rotator</i> .....	48
3.2.6	<i>Pulse Compression Outside the Laser</i> .....	49
3.2.7	<i>The Variable Attenuator</i> .....	50
3.2.8	<i>Beam Expansion</i> .....	51
3.2.9	<i>The Objective</i> .....	52
3.2.9.1	<i>Working Distance and Depth of Field</i> .....	52
3.2.9.2	<i>Beam Truncation</i> .....	53
3.2.9.3	<i>Objective Alignment Procedure</i> .....	54
3.2.10	<i>Empirical Determination of Microscope Resolution</i> .....	55
3.2.11	<i>Brightfield imaging</i> .....	57
3.2.11.1	<i>The Tube Lens</i> .....	57
3.2.11.2	<i>Image Magnification</i> .....	58

3.2.12	<i>Fluorescence detection</i>	62
3.2.12.1	<i>The Monochromator</i>	62
3.2.12.2	<i>The Photomultiplier Tube</i>	66
3.2.13	<i>Data Acquisition</i>	66
3.3	ZnO synthesis	68
3.3.11	<i>Hydrothermal Synthesis</i>	69
3.3.12	<i>Chemical Vapor Deposition (CVD)</i>	71
3.3.13	<i>Solution phase synthesis</i>	72
3.4	References	75
 <u>Chapter 4</u> Characterizing Charge Carrier Trapping in Single ZnO Rods		76
4.1	Introduction	77
4.2	Experimental	80
4.3	Results and Discussion	83
4.3.1	<i>Two-Photon Imaging</i>	83
4.3.2	<i>Photoluminescence Spectra</i>	88
4.3.3	<i>Time Resolved Photoluminescence</i>	91
4.3.4	<i>Trapping Dynamics</i>	95
4.4	Conclusions	103
4.5	References	105
 <u>Chapter 5</u> Characterization of Spatially Specific Carrier Behavior along a Single ZnO Rod		108



5.1 Introduction.....	109
5.2 Experimental.....	110
5.3 Results and Discussion .....	112
5.3.1 <i>Effect of annealing temperature on the steady-state spectrum</i> .....	114
5.3.2 <i>Effect of annealing temperature on the time-dependent kinetics</i> .....	119
5.3.3 <i>Comparison of the photophysics from different structural regions</i> .....	122
5.4 Conclusions.....	126
5.5 References.....	127
 <u>Chapter 6</u> Spatially Specific Electron-Hole Plasma Formation in a Single ZnO Rod.....	130
6.1 Introduction.....	131
6.2 Experimental.....	131
6.3 Results and Discussion .....	133
6.5 Conclusion .....	142
6.5 References.....	143
 <u>Chapter 7</u> Conclusion.....	146

## List of Figures

- Figure 1.1.** ZnO energy diagram. Upon photoexcitation an electron is promoted from the valence to conduction band. It can then either relax into an excitonic state, giving rise to near-UV emission (390 nm), or fall into a trap state and emit around 550 nm. The trap states are due to defects in the lattice and lie throughout the band gap, giving rise to a broad visible emission band.....4
- Figure 1.2.** Schematic depiction of the defects that generally occur in semiconductor crystals (a hexagonal rod is shown here). Common point defects include vacancies where an atom is missing from the lattice, substitutions where an atom is the wrong lattice site, and interstitials where an atom is embedded in the lattice. Non-bonded electrons on the crystal surface can also trap carriers and are commonly referred to as dangling bonds .....5
- Figure 1.3.** The excess negative charge created by dangling bond on the surface repels electrons in the conduction band and attracts holes in the valence band. This is represented by the bands bending upward at the surface. The resulting low concentration of mobile electrons at the surface is commonly referred to as a depletion zone .....6
- Figure 1.4.** Schematic depiction of the processes that give rise to an electron-hole plasma (EHP). Under low excitation intensity, fluorescence is generated by simple excitonic recombination. As the excitation intensity increases the exciton density gets larger with an increasing presence of free carriers. The increased density causes excitonic collisions and scattering processes that broaden the emission band and weaken the exciton binding energy, drawing the charges further away from each other. This should lead to a blue-shift of the spectrum; however, this is masked by the increasing density of free carriers and exciton dissociation, and is therefore not observed in our data. As the excitation intensity is increased further, the excitons dissociate completely and the high free carrier concentration gives rise to the formation of an electron-hole plasma. Exchange interactions and correlated effects (described in the text) stabilize the plasma, decreasing the size of the band-gap and causing a red-shift in the emission spectrum. Figure is adapted from Klingshirn<sup>7</sup> .....8
- Figure 2.1.** Jablonski diagram showing a one and two-photon excitation transition. Two-photon absorption occurs almost simultaneously. The absorption of the first photon promotes the electron to a virtual state (VS) followed by the second photon that completes the transition to the excited state. The emission frequency is the same for both processes.....17

<b>Figure 2.2.</b>	Schematic depicting the increasing probability of two-photon absorption at the focal point of the objective .....	19
<b>Figure 2.3.</b>	Example of the optical sectioning capability in two-photon microscopy. The two-photon emission image on the left is of 2 $\mu\text{m}$ beads infused with Nile-Red. The two beads in the center appear dimmer and have a smaller diameter, suggesting they are above the other beads as depicted on the right.....	20
<b>Figure 2.4.</b>	Schematic depiction of second harmonic generation in birefringent crystals. Here BBO is beta barium borate, KTP is potassium titanyl phosphate and LiNbO <sub>3</sub> is lithium niobate .....	24
<b>Figure 2.5.</b>	The atomic polarization response in the presence of a moderate and strong driving force (i.e. the electric field). The example of a ball on a spring is used to illustrate the dipole displacement in symmetric and asymmetric oscillations (as would be expected in noncentrosymmetric materials). The oscillations are described in terms of harmonic oscillator potentials (center) and the associated waveforms are shown on the right .....	25
<b>Figure 2.6.</b>	In microscopy the intensity of the focal spot takes on a Gaussian distribution. There is a phase shift close to focal center which leads to an increase in wavelength in that region. The SHG is therefore generated in two symmetric lobes to maintain a phase-matching condition.....	30
<b>Figure 3.1.</b>	Schematic overview of our nonlinear microscope system. Excitation light is generated by a pulsed, femtosecond laser that is pumped by a CW diode-pumped laser (532 nm). The system generates pulses with an 80 fs width at a 76 MHz repetition rate. The output is sent through a Faraday rotator to prevent reflections from reaching the laser system. A prism compressor is used to correct for pulse dispersion. The power entering the microscope is controlled with a variable attenuator that consists of a waveplate and a polarization beam-splitter cube. Light is the expanded 2x, to overfill the input aperture of the objective. The sample is raster scanned across the objective focal point and the resulting fluorescence/SHG is collected back through the objective, focused into the slit of a monochromator and detected by a photomultiplier tube.....	36
<b>Figure 3.2.</b>	Photograph of our optical setup. The beam path is shown in red, and the fluorescence in green. The large red spot indicates beam expansion and the green spot indicates the objective focal point. An image of the prism compressor is shown in the upper right .....	37

- Figure 3.3.** Four-level energy diagram depicting a population inversion condition that is a requirement for lasing.  $R_p$  is correlated with the pumping efficiency. As long as the relaxation from  $E_1$  to  $E_0$  is faster than  $E_2$  to  $E_1$  the number of carriers in  $E_2$  will be greater than  $E_1$ , creating the population inversion and enabling the amplification of stimulated emission (lasing). Adapted from Reference #3 ...40
- Figure 3.4.** Basic optical layout of the Ti:S laser. The beam from the pump laser is focused into the Ti:S crystal and stimulates emission. Mode-locking is facilitated by sending the resulting laser beam through a slit, which can be adjusted to select different output frequencies. A prism compressor, consisting of four prisms corrects for pulse dispersion. Light oscillates between the high reflector and output coupler. Occasionally, some light transmits through the output coupler which represents the laser output.....43
- Figure 3.5.** Passive mode-locking in the laser system occurs by a Kerr lens effect where the intensity across the beam wavefront causes a gradient in the index of refraction within the Ti:S crystal. Light generated at the focal point is the most intense and contributes to mode-locking. Light generated outside this area is in CW operation and is rejected by a slit, thereby enhancing the mode-locking process. Adapted from Reference # 4 .....45
- Figure 3.6.** Prism pair compressor, operated in a double pass configuration. The prisms are placed such that the longer wavelengths of light have to travel a further distance which compensates for pulse dispersion. The inset shows the placement of the prism must be placed at the angle of minimum deviation between the incident and refracted beams, to ensure the light is entering at Bragg's angle .....47
- Figure 3.7.** Algorithm for determining the width of the beam at the focal point of the objective using  $2\ \mu\text{m}$   $\varnothing$  Nile Red beads. Given the  $\text{IPSF}^2$  has a Gaussian profile and the intensity of the bead has a semi-circular profile, the two functions can be convoluted to yield our theoretical resolution. The data is fit to the convolution and the resulting FWHM is directly correlated to the width of the beam.....55
- Figure 3.8.** Optical layout for brightfield and CCD imaging. The area between the objective and tube lens represents infinity space where the light rays are parallel to each other. Light is focused into the CCD camera with a lens commonly referred to as the eyepiece. In our setup this is a simple plano-convex lens. Adapted from Reference #7 .....57
- Figure 3.9.** Lens magnification, which can be described as the ratio between the image distance ( $s''$ ) and the object distance ( $s$ ).....58

- Figure 3.10.** The distance between the lens and the image plane changes as the object gets closer to the lens. In our setup, this requires that the CCD camera be moved to account for the change .....59
- Figure 3.11.** (*left*) Brightfield images of a single structure collected with increasing magnification. The reduction in intensity is due to the increasingly divergent light and indicates the inverse relation between S/N ratio and magnification. The graph on the right is a comparison of the relative magnification as a function of actual (squares) and theoretical object distances (connected circles).....60
- Figure 3.12.** Czerny-Turner monochromator. Light entering the monochromator is collimated by the first mirror and directed to the diffraction grating. Each frequency of light is diffracted off the grating at different angles and focused by the second mirror. The angle of this mirror determines which frequencies of light will be permitted through the exit slit. The monochromator in our setup follows a similar design except that the slits are on opposing faces of the monochromator .....62
- Figure 3.13.** Schematic depiction of a photomultiplier tube (PMT). If light incident on the photocathode is greater than its work function, then an electron will be released and accelerated towards a dynode. Each dynode is held at successively greater potentials so that as electrons accelerate and reflect off them, they release another electron. The result is a rapid amplification of the signal into a readily detectable current .....64
- Figure 3.14.** Data acquisition process. Light detected by the PMT is sent to a discriminator that filters noise and outputs 5 V TTL pulses. Each pulse is counted by a data acquisition card. Since each pulse is from one photon, higher counts correspond to higher intensity emission. This process continues along every step in the x-direction. Once the stage has reached the end of a line, the data is placed into a two-dimensional array, and the process is repeated for the next line. The resulting two-dimensional array represents the image intensity profile.....66
- Figure 3.15.** Typical structures obtained using hydrothermal synthetic methods. The experiments described herein were conducted on structures like those shown in (A) and (B). The needle-shaped rods have a hexagonal cross-section and range between 5 and 20  $\mu\text{m}$ . We have also obtained similar rods with flat ends (C) and flower-like structures (D) with this method.....68
- Figure 3.16.** Nanorod growth using CVD occurs in patches on the substrate surface. This may be due to rough areas that trap nuclei which initiates structure growth...70

- Figure 3.17.** The images in (A), (B) and (C) are of tetrapods with differing end morphologies grown using CVD. (D) is an example of ribbon structures .....71
- Figure 3.18.** Results from solution phase synthesis give rise to dumbbell shaped structures, both solid (A) and hollow (B). This same reaction, conducted at a lower temperature, yields the ribbons shown in (C) .....72
- Figure 4.1.** Band-diagram depicting the photophysical transitions that give rise to the emission bands in ZnO following a two-photon excitation. Electrons can either relax into excitonic states and recombine with a hole in the valence band, giving rise to band-edge emission centered around 390 nm, or fall into trap states localized within the band-gap giving rise to low-energy emission centered around 550 nm. A) Depicts recombination between an electron in the conduction band and a hole localized on an acceptor trap state. B) Depicts recombination between an electron localized on a shallow donor trap state and an electron bound to an acceptor trap state .....78
- Figure 4.2.** Schematic depiction of the two-photon microscope setup. Pulsed light exiting the laser system is sent through a prism compressor to control pulse dispersion. Excitation light is reflected off a dichroic mirror and excites the sample at the focal point of the objective. The resulting fluorescence is collected back through the objective, focused into the entrance slit of a monochromator and detected using a photomultiplier tube .....80
- Figure 4.3.** (*Left*) A scanning electron microscopy image of a typical ZnO rod used in our experiments. The structure is  $\sim 10\ \mu\text{m}$  in length and  $\sim 1.5\ \mu\text{m}$  in the center, tapering down to  $\sim 500\ \text{nm}$  at the end. (*Middle*) Band-edge emission (390 nm) and (*Right*) trap (550 nm) emission images. Each image shows enhanced intensity at the ends of the structure, due to a greater propensity for light to couple into optical cavity modes at that location (see text). The dark area in the center is attributed to the presence of a grain boundary. The enhanced intensity at the facet vertices may be due to light coupling into whisper gallery modes (see Figure 4.4 and text) .....84
- Figure 4.4.** (*Left*) A second harmonic image of the ZnO rod shown in the lower panel. The image in the center represents the results of modeling the process giving rise to the periodic pattern. The rod's cross-sections supports Fabry-Perot and whispering gallery modes. The degree of coupling into the modes depends on cross-sectional diameter which changes as the rod taper from the middle to the ends. Refer to Mehl et al. for further detail .....84
- Figure 4.5.** (A) Brightfield and corresponding fluorescence image (350 nm) collected using a CCD camera. The bright spot in the fluorescence image represents emission from the excitation region. Fluorescence emanating from the ends of

the structure may be due to light coupling into wave-guiding modes in the cavity. (B) This observation is supported by two rods in close proximity at one end. Emission generated at one structure propagates and couples into the nearby structure, where it is further wave-guided to the opposing end. While wave-guiding is evident, the dominating process appears to be due to light coupling into the cavity at the excitation region .....86

**Figure 4.6.** ZnO emission spectrum following a two photon excitation in the center of the rod shown in Figure 4.3. The sharp feature centered around 365 nm corresponds to second harmonic generation. The emission band centered around 390 nm represents exciton and free-carrier recombination between the valence and conduction bands. The broad emission centered around 560 nm corresponds to recombination events involving trap states that are localized within the band-gap and arise due to defects in the crystal lattice.....88

**Figure 4.7.** Polarization character of the band-edge and trap emission. Band-edge emission is predominantly generated perpendicular to the *c*-axis of the rod, with a -0.43 polarization ratio of. The trap emission shows no dependence on polarization .....89

**Figure 4.8.** Time-resolved photoluminescence measurements collected using a streak camera (*top panel*) and time-correlated single-photon counting (TCSPC) instrumentation. The streak-camera time resolution is ~20 ps (shown in the inset) enabling us to time resolve the band-edge emission. Although a delayed rise in the trap-emission band appears to exist in the TCSPC data, the streak camera data suggests it does not. Convolution of the TCSPC trap emission transient with the instrument response function confirmed the appearance of the delayed rise is an experimental artifact (shown in the inset with the TCSPC data). The transients are consistent with reports in the literature that report the band-edge emission decays within 50-100 ps. The trap emission bands are multi-exponential, displaying a fast sub-nanosecond component, followed by slower components that decay in 10-100's of nanoseconds. The data were collected from the center of the structure shown above, as indicated by a white circle .....91

**Figure 4.9.** Defect emission kinetics depend on local structural region. Examples of data collected from the middle, left middle and end of structures with (*top*) and without (*bottom*) a grain boundary in the center are shown. In the structure with a grain boundary the emission decays faster in the center consistent with an increase in the non-radiative rate due to the increased defect density around the grain boundary. The kinetics from the left-middle resembles the transient from the middle at early times, and the end position at later times. The structure with no grain boundary displays different behavior. Here the kinetics from the end is faster than the middle, consistent with a lower defect density in the middle of the structure .....93

**Figure 4.10.** Time-resolved data before annealing. The top panel shows the emission kinetics, with a faster decay observed at higher energies. The time-dependent

spectra shown in the middle row reveals an 8-10 nm red-shift before annealing. The rate of the shift from 16 rods is displayed in the bottom panel. The red shift varies in magnitude between 4 and 10 nm and occurs within the first 4-6 ns following photoexcitation .....94

**Figure 4.11.** Steady-state spectrum from the same position in the same rod, collected before and after annealing. The graphs are normalized to the maximum of the band-edge emission. We observe an ~40 nm blue-shift in the spectrum following annealing, in addition to a drastic reduction in the overall intensity of the trap emission band. The magnitude of the spectral shift from four other structures is displayed by a series of arrows originating at the spectral maximum before annealing and terminating at the maximum following annealing .....96

**Figure 4.12.** Time-resolved data taken after annealing. The top panel shows the emission kinetics have a faster decay at lower energies, in contrast to our observations before annealing. The time-dependent spectra shown in the middle row reveals an ~15 nm blue-shift. The rate of the shift from 5 rods is displayed in the bottom panel. There is an ~15 nm blue shift in each structure that occurs within the first 2 ns following photoexcitation .....98

**Figure 4.13.** Schematic depiction of the proposed models that give rise to the time-dependent blue-shift. Follow photoexcitation, the excess free carriers that are generated cause a renormalization of the band gap. As the carriers begin to recombine, the band-gap recovers to its initial state (dashed line), and gives rise to a time-dependent blue-shift. Note the shift shown here is exaggerated for clarity. Additionally, those photoexcited carriers that migrate to the structure surface will move higher in energy as the bands bend upwards. This transition will only occur occasionally because of the depletion region at the surface. Therefore those carriers in the bulk will tend to recombine first, followed by the higher energy transitions on the surface .....102

**Figure 5.1.** Examples of band-edge and trap emission images (scale bar 1  $\mu\text{m}$ ). The band-edge emission represent exciton or free carrier recombination between the valence and conduction bands. This correlates with the narrow band in the emission spectrum that is centered around 390 nm. The trap emission arises due to defects in the structure whose energy states are localized within the band-gap. The distribution of these state gives rise to a broad low energy band centered around 550 nm. Both images show areas of high intensity at the ends of the structure and low intensity in the middle. The emission patterns are discussed further in the text .....113

**Figure 5.2.** (*Top*) A scanning electron microscopy image of a rod annealed at 550°C. The rod is typical of the structures used in our experiments and shows no signs of thermal damage (Scale bar is 1  $\mu\text{m}$ ). The trap emission spectrum collected between the end and middle corresponds to the 550°C spectrum shown in the



middle panel. (*Middle*) Comparison of time-integrated spectra collected before (grey) and after annealing. The spectra are normalized to their overall area to facilitate comparison. The remarkable agreement in the spectra before annealing indicates little variation in defect signatures between each rod. A gradual blue-shift is observed with increasing annealing temperature. The analysis was conducted on approximately 15 structures at three different locations, per annealing temperature. The magnitude of the blue-shift from each structure was determined by subtracting the spectral maximum following annealing, from the value before annealing. The distribution of results is shown in the bottom panel and indicates that the structures generally follow the same trend show in the spectra above .....115

**Figure 5.3.** Emission (550 nm) decay kinetics before and after annealing at 450°C. Each transient displays multiexponential kinetics, but the lifetimes differ drastically. Before annealing, the emission decays to zero in 100 ns, after annealing, the decay lengthens to 2  $\mu$ s. This is attributed to increased trapping time following annealing as discussed further in the text .....120

**Figure 5.4.** Time-dependent shift in the spectral maximum collected from the end and middle of five rods. The data corresponding to the rod shown above are displayed as grey lines with every 25<sup>th</sup> point marked in black. The scale bar corresponds to 1  $\mu$ m. The data shows that the blue-shift is greatest in the middle of the structure and least at the end. Interestingly we occasionally observe a rapid red-shift in the spectrum at the end of the structure. Mechanisms for this behavior are discussed in detail in the text.....122

**Figure 5.5.** Comparison of the steady-state spectra collected from different focal planes between the interior and surface of a single structure. Data collected before annealing (*left*) shows no shift in the spectral maximum with position. However, the data after annealing at 450°C shows that the spectra in the interior is blue-shifted by ~30 nm, relative to either surface. Note that the data was taken from two separate structures .....125

**Figure 6.1.** (*Top*) Band-edge (BE) and trap (T) emission images of the rod shown in the scanning electron microscopy image (Scale bar corresponds to 1  $\mu$ m). The images show areas of enhanced intensity at the end of the structure and along the facet vertices. This behavior has been attributed to coupling into various transverse and longitudinal optical modes. (*Middle*) ZnO emission spectrum taken from the interior of the structure shown above. The narrow peak centered around 390 nm corresponds to BE emission, and the broad peak in the visible region is due to trap states that arise from lattice defects. (*Bottom*) ZnO emission spectrum collected at increasing excitation intensities. The BE

emission broadens and shifts to lower energies with an increase in the BE:T emission ratio. The inset shows that this relation is linear with the square of the excitation power. Here the excitation is squared to account for the quadratic dependence of emission on two-photon excitation intensity .....134

**Figure 6.2.** Spectra collected from the end, interior and middle of a single structure, as indicated by the schematic juxtaposed with each graph. Spectra were collected at increasing excitation power (here  $P_0$  corresponds to 5 mW average power). The shift is largest at the end of the structure (~16 nm) with only a minor shift in the middle (~2 nm). This is attributed to the smaller dimensions at the end of the structure, as well as a greater propensity for light to couple into optical cavity modes in that region .....136

**Figure 6.3.** A similar experiment to Figure 6.2 conducted at a 7.6 MHz repetition rate (here  $P_0$  corresponds to 2 mW average power). We observe similar behavior to that shown in Figure 6.2. The shift is largest at the end of the structure (~14 nm) with only a minor shift in the middle (~2 nm). This is agreement with the formation of an electron hole plasma and shows the shift in our structures is not due to local heating effects .....137

**Figure 6.4.** Time-resolved spectra collected with a nitrogen-cooled CCD camera with 100 ms resolution. We observe no shift in the emission band with time (corroborated by the normalized spectra in the inset). This indicates that the shift occurs within the first 100 ms, consistent with EHP formation and in stark contrast to reports that attribute the red-shift to local heating effects...139

**Figure 6.5.** Band-edge emission images collected using a CCD camera. The bright spot in each image represents fluorescence emanating from the focal volume. Apparent in each image are regions of enhanced intensity at the ends of the structure. A longitudinal cross-section from the rod following increasing excitation is shown in the graph (the plots are normalized to the maximum intensity). We do not observe an increase in the emission from the end opposite to the excitation which suggests we are observing spontaneous and not stimulated EHP emission .....140

**Figure 6.6.** Power-dependent BE emission spectra collected at a 7.6 MHz repetition rate (here  $P_0$  corresponds to 2 mW). The spectrum decreases at the highest intensity, correlated with increased band broadening and BE:T emission ratio. The decreased emission may be due to stimulated emission propagating along the longitudinal axis. Given our experimental geometry, this would direct light away from the objective and not be detected by our system, consistent with the observed decrease .....141

## List of Abbreviations and Symbols

A	angular modulation
$A \rightarrow e^-$	acceptor recombination with conduction band
BE	band edge
BE:T	band edge to trap emission ratio
BGR	band-gap recombination
BW	band width
$c$	speed of light
CB	conduction band
<i>c.c.</i>	complex conjugate
$(CH_2)_6N_4$	Methenamine
CM	confocal microscopy
CVD	chemical vapor deposition
CW	continuous wave
$d$	distance
D	diameter
$D'$	dispersion
DAP	donor-acceptor pair
DAQ	data acquisition
$e^-$	electron
$E_A$	acceptor energy
$E_D$	donor energy
$E_F$	Fermi energy

$E_g$	band-gap energy
EHP	electron-hole plasma
$E(t)$	applied optical field
$E_0$	lower energy state
$E_3$	highest energy state
$f(x)$	fluorescence intensity of a bead
$f$	focal length
FP	Fabrey Perot
FWPH	full width at half maximum
F/#	F-number
g/mm	grooves per mm
$(h^+)_{VB}$	hole at Valence Band edge
HeNe	Helium:Neon
I	intensity
$I_L$	focused laser spot
$k$	wave vector
K	indicates a constant
$L$	length of the cavity
$M$	magnification
$n$	refractive index
$n(t)$	photon density of applied signal
$N$	represents a number variable
NA	numerical aperture
NSOM	near-field scanning optical microscope

OPM	one-photon microscopy
PMT	photon multiplier tube
$P(t)$	polarization as a function of time
$P_L$	power loss
$q$	integer number
$s$	object distance
$s''$	image distance
$S$	slit
SEM	scanning electron microscopy
SHG	second harmonic generation
SHGM	second harmonic generation microscopy
S/N	signal to noise ratio
T	truncation ratio
TCSPC	Time-correlated single-photon counting instrumentation
Ti:S	titanium: sapphire
TPM	two-photon microscopy
V	excitation volume
$V_O$	oxygen vacancy
$V_{Zn}$	zinc vacancy
VLS	vapor-liquid-solid
VS	vapor-solid
$w_x$	beam waist in axial dimension
$w_y$	beam waist in lateral dimension

WHM	whispering gallery mode
$\gamma_2$	spontaneous energy decay rate from higher energy rate
$\delta$	diameter of excitation region
$\Delta E$	transition energy
$\epsilon_0$	vacuum permittivity in free space
$\eta_p$	fraction of electrons populating an energy state
$\theta$	corresponds to an angle
$\phi_F$	fluorescence quantum yield
$\phi_c$	radiant flux
$\lambda$	wavelength
$\Delta\lambda$	change in wavelength
$\lambda_t$	wavelength at time (t)
$\lambda_i$	initial wavelength
$\xi$	phase shift
$\rho$	polarization ratio
$\sigma_{2p}$	two-photon ‘action’ cross section
$\tau$	round trip time through the laser cavity
$\varphi$	corresponds to an angle
$\chi^{(1)}$	linear susceptibility tensor
$\chi^{(2)}$	second-order nonlinear susceptibility tensor
$\omega$	frequency
$\frac{1}{e}$	corresponds to the width of the IPSF <sup>2</sup>

# **CHAPTER 1**

## **Introduction**

## 1.1 Motivation

To date, a greater part of scientific discovery has been drawn from experimental analyses on entire populations, or ensembles, of molecular complexes. The implicit assumption is that every member within the population behaves identically. Such an assumption may be valid for simple molecules such as benzene, where few differences in dynamics and structure could arise between each molecule. However, as systems become more complex this assumption becomes increasingly erroneous. In nanoscale materials, this heterogeneity often stems from structural factors that are introduced during material preparation; for example, within a population of nanoparticles one would expect each particle to vary in size, resulting in a largely heterogeneous population. Additionally, the integration of defects in the crystal lattice is inevitable, and could arise in different locations and concentration between each structure. Therefore, as the complexity of the system and the environment increases, the heterogeneity within a population becomes more pronounced. This is a hallmark of complexity that is evident in experiments ranging from single-structure conductivity measurements to single-molecule spectroscopy.<sup>1-6</sup>

As technology continues to move towards smaller scales, differences between structures becomes increasingly important and poses a major challenge to those wishing to understand and exploit nanoscience. The implication is that results obtained from ensemble averaging become less representative of the sample population, and it becomes necessary to study the system at the level of individual structures. Indeed, these experiments have been done, and show that objects with dissimilar shapes exhibit different dynamics, giving rise to inter-object heterogeneity.<sup>8-10</sup> There is, therefore, a direct correlation between the shape of an object and its electronic and photophysical character. The question thus arises: Can similar



heterogeneous behaviors be observed at spatially distinct locations in a single object? In the work described herein, we show that intra-object heterogeneity does exist and a chief objective of this project is the methodical exploration of this phenomenon.

The characterization of intra-object heterogeneity is fundamentally important to many problems in nanoscience and nanotechnology and will ultimately have broad implications to the understanding of nanodevice performance. It is specifically relevant to the incorporation of different morphologies (wires, rods, tubes, needles, ribbons, belts, helices, tetrapods, etc.) into electronic and optoelectronic device applications, where the exploitation of shape dependent phenomena is beginning to translate into novel functionalities.<sup>11-17</sup> Understanding these issues requires that we forge a connection between the dynamics exhibited by an object and its underlying shape.

Before this project, much of the work conducted in our laboratory employed techniques that average over the entire ensemble. To broaden our capabilities so that we may characterize systems with single structure resolution we constructed an inverted fluorescence microscope (Chapter 3). Constructing a microscope enabled us to readily incorporate equipment already available to us in the laboratory to develop techniques such as two-photon and second harmonic generation microscopy (Chapter 2). These nonlinear methods are used extensively in a broad range of disciplines. They provide advantages and yield information about a system's characteristics that conventional microscopy techniques cannot. Here, we utilize the unique properties of these methods to obtain detailed information from single ZnO structures that enable us to correlate system dynamics with changes in local shape. A brief background on ZnO and the reasons we chose to focus on it are described in the following section.

## 1.2 ZnO Background

ZnO is a wide band-gap (3.4 eV) semiconductor with near UV absorption and emission bands. Its strong exciton binding energy (60 meV) means excitons will be stable at room temperature making it an attractive candidate for potential use in UV-blue optoelectronic, photovoltaic, and laser-based applications.<sup>15, 18, 19</sup> Additionally, ZnO has several key qualities that make it an ideal initial target for this project: 1) It has a high potential for synthetic manipulation, with a variety of nano- and micro-scale shapes, including nanoparticles, nanowires, ribbons and more complicated tetrapod and flower-shaped structures.<sup>8, 14, 20, 21</sup> 2) Single crystal wires can be synthesized with nanometer-sized diameters and length scales ranging from nanometers to microns, the larger of which are well-matched for the microscopy projects described herein. 3) ZnO nanowires have a large second-order nonlinear susceptibility ( $\chi^{(2)}$ ), resulting in efficient SHG, a large two-photon cross-section that provides flexibility in experimental design, and are photochemically robust enabling them to withstand intense optical fields.<sup>19, 22-24</sup>

A band diagram depicting the ZnO energy states is shown in Figure 1.1. Photoexcitation of ZnO nanostructures above the band gap ( $\lambda < 360$  nm) produces free carriers whose dynamics have been followed in a range of ZnO structures using a variety of time-resolved absorption, emission, and non-linear optical techniques. Carriers can relax into excitonic states resulting in band edge emission at 390 nm.<sup>14, 25-27</sup> Exciton lifetimes obtained from time-resolved emission studies are in the 100's of picoseconds, and depend upon the size and shape of the ZnO structure.<sup>19, 28, 29</sup> In addition to exciton formation, carriers can become trapped in defect sites located either inside the structure or at its surface, resulting in a broad, 550 nm visible emission band with a nanosecond lifetime.<sup>26, 27</sup>

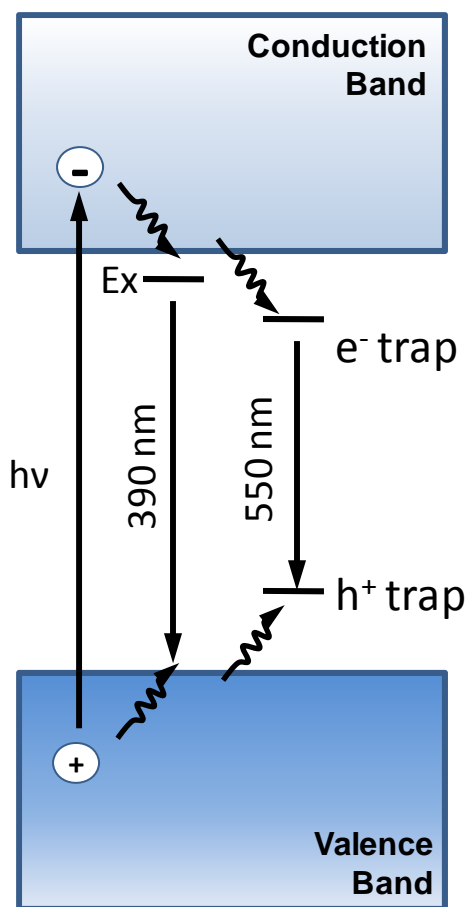


**Figure 1.1:** ZnO energy diagram. Upon photoexcitation an electron is promoted from the valence to conduction band. It can then either relax into an excitonic state, giving rise to near-UV emission (390 nm), or fall into a trap state and emit around 550 nm. The trap states are due to defects in the lattice and lie throughout the band gap, giving rise to a broad visible emission band.

### 1.2.1 Defect Definitions and Categories

The interactions between carriers and defect states are the central theme in Chapters 4 and 5, and so afford some mentioning here. Defects are an intrinsic property of every crystalline material, that arise during the growth process. They can have a profound effect on carrier dynamics and must be taken into consideration during device development and design. While defect chemistry is a broad topic, we focus our discussion on point and surface defects. Point defects represent single atom defects in the crystal lattice and can be categorized as either interstitial, vacancy, or substitutional defects.<sup>30</sup> Interstitial defects arise when an atom is embedded in a unit cell, vacancies are missing atoms in the lattice, and substitutions are due to atoms in the wrong lattice site (e.g. in ZnO, an O occupying a Zn site and vice versa) (Figure 1.2). The energetic states associated with these defects are localized throughout the band-gap (Figure 1.1). Their precise location within the gap is dictated by their ionization energy. States

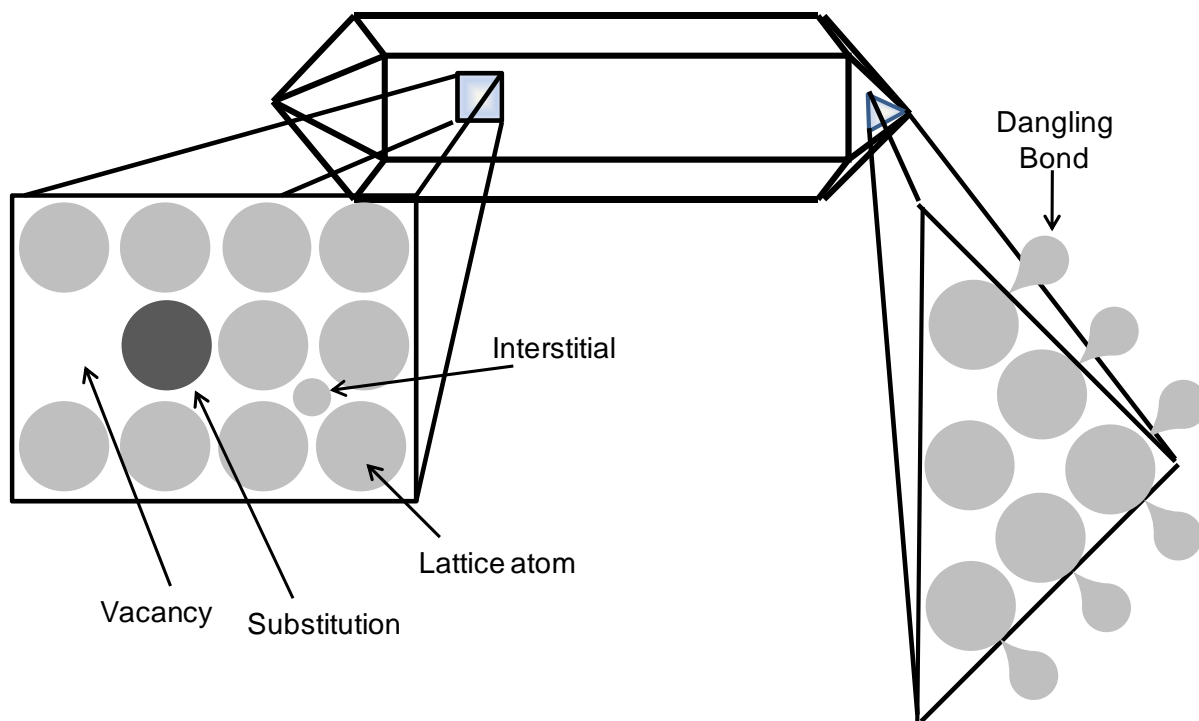


**Figure 1.2:** Schematic depiction of the defects that generally occur in semiconductor crystals (a hexagonal rod is shown here). Common point defects include vacancies where an atom is missing from the lattice, substitutions where an atom is the wrong lattice site, and interstitials where an atom is embedded in the lattice. Non-bonded electrons on the crystal surface can also trap carriers and are commonly referred to as dangling bonds.

lying higher in energy tend to donate their electrons to the conduction band and those lying lower in energy tend to accept electrons, thus they are termed ‘donor’ and ‘acceptor’ defects, respectively. Charges associated with donors and acceptors in sufficient proximity can recombine with each other and release a photon, in what is described as “donor-acceptor pair” emission. The energy of these transitions is inversely proportional to the spatial proximity of the donor and acceptor<sup>31</sup>, and has important implications in the interpretation of our results in Chapter 4.

Surface defects can arise for a number of reasons, but the ones most relevant to our experiments arise from the non-bonded electrons on the crystal surface. These are generally

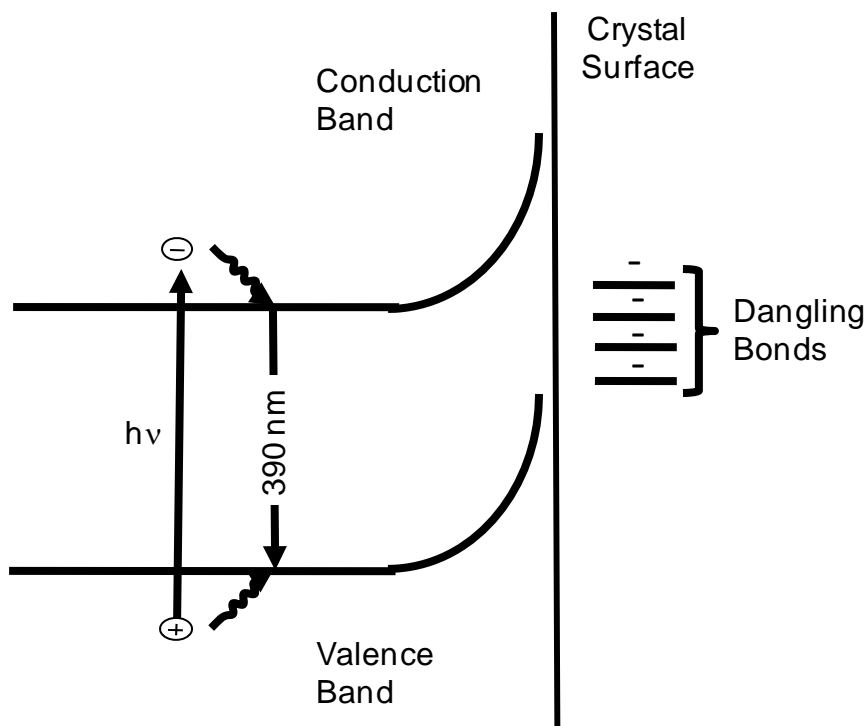


**Figure 1.3:** The excess negative charge created by dangling bond on the surface repels electrons in the conduction band and attracts holes in the valence band. This is represented by the bands bending upward at the surface. The resulting low concentration of mobile electrons at the surface is commonly referred to as a depletion zone.

referred to as dangling bonds (Figure 1.2).<sup>30</sup> In n-type (electron rich) materials the excess negative charge on the surface increases the repulsive force with electrons and the attractive force with holes approaching the surface. This causes the conduction and valence bands to bend upwards in energy Figure 1.3. Since holes relax upwards, this increases their affinity for the surface. However, the electron favors lower energy and the band bending causes them to migrate away from the surface. This phenomenon results in an electron depletion region near the surface of the structure<sup>30</sup> and has important implications in the interpretation of our results in Chapter 5.

Despite having been studied for decades, there is no consensus in the literature as to the precise defect types that give rise to the broad green emission band in ZnO. This is due in part to the different methods that can be used to synthesize ZnO structures, which are characterized by different reaction environments and growth mechanisms. A discussion on the types of defects that give rise to our observations is included in each chapter. Several detailed articles on the subject have also recently been published that comprehensively review the subject.<sup>11, 16, 32, 33</sup>

### 1.2.2 Exciton Dynamics and Free Carrier Interactions

There have now been several studies that suggest the UV emission in ZnO can couple into longitudinal optical cavity modes and wave-guide to the ends of the structure.<sup>9, 18, 27</sup> We observe similar behavior (Chapter 4-6) and, given our experimental geometry, attribute it to a stronger propensity for light to couple into transverse optical cavity modes in that region of the structure (Chapter 6). Under high excitation intensities the UV emission mechanism begins to change. The resulting processes can give rise to stimulated emission and lasing. Recent studies<sup>25, 34-37</sup> have explored the ultrafast exciton dynamics under lasing conditions achieved with intense excitation using both harmonic generation and stimulated emission pumping.

The mechanisms giving rise to these observations are depicted in Figure 1.4. At low intensity the band-edge (BE) emission arises due to excitons that exist in a low density regime. As the excitation intensity increases the exciton density gets larger, causing them to begin interacting with each other. Elastic and inelastic scattering processes result in collision-broadening of the exciton resonances, giving rise to an increase in the width of the BE emission spectrum.<sup>7</sup> As the intensity is increased further, free carriers begin to

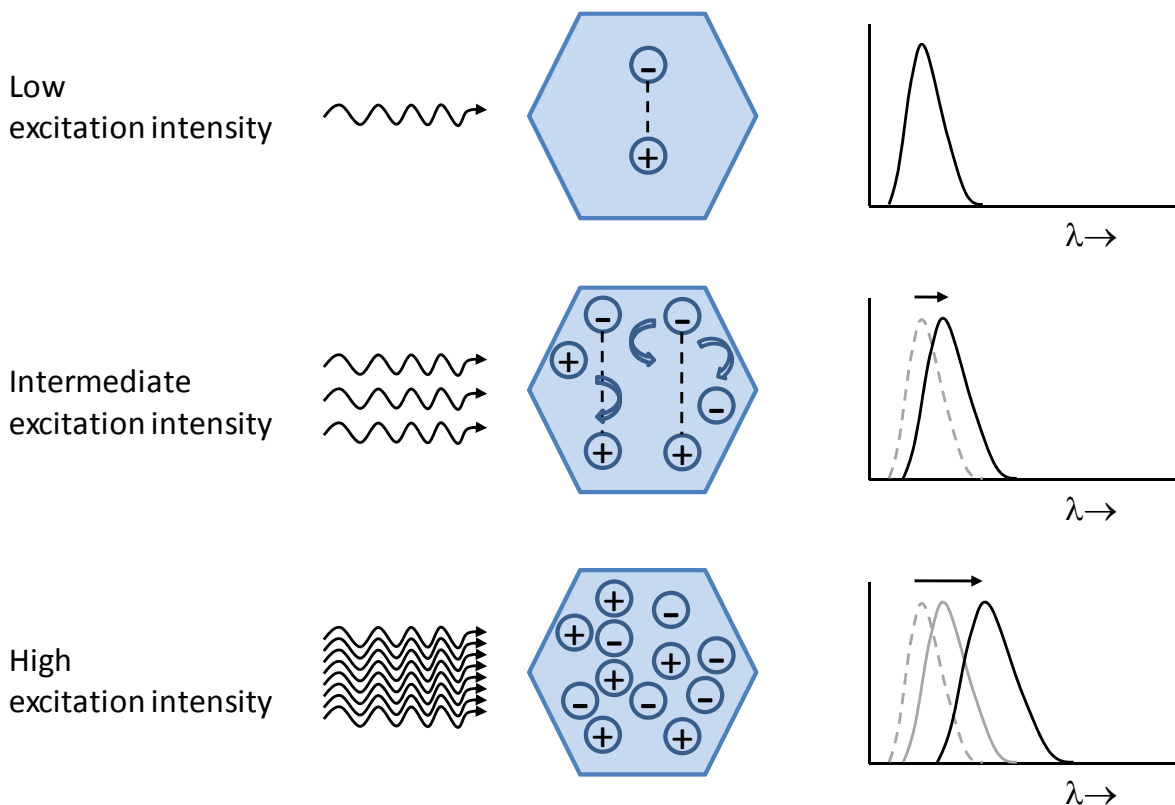


**Figure 1.4:** Schematic depiction of the processes that give rise to an electron-hole plasma (EHP). Under low excitation intensity, fluorescence is generated by simple excitonic recombination. As the excitation intensity increases the exciton density gets larger with an increasing presence of free carriers. The increased density causes excitonic collisions and scattering processes that broaden the emission band and weaken the exciton binding energy, drawing the charges further away from each other. This should lead to a blue-shift of the spectrum; however, this is masked by the increasing density of free carriers and exciton dissociation, and is therefore not observed in our data. As the excitation intensity is increased further, the excitons dissociate completely and the high free carrier concentration gives rise to the formation of an electron-hole plasma. Exchange interactions and correlated effects (described in the text) stabilize the plasma, decreasing the size of the band-gap and causing a red-shift in the emission spectrum. Figure is adapted from Klingshirn.<sup>7</sup>

form and interact with the excitons. This begins to screen the Coulombic attractive force binding the electron hole pair. The weakening of the Coulombic potential expands the exciton orbital wavefunction, so that the charges are spaced energetically further apart. The

net result is a blue-shift in the emission spectrum.<sup>38</sup> This shift is much smaller than the exciton binding energy, and quickly reverses as the excitation intensity increases.

The increasing free carrier concentration screens the excitonic binding energy and leads to the formation of an electron-hole plasma (EHP). When the carrier concentration reaches a critical density (termed the Mott Density), the screening length approaches the exciton Bohr radius and the excitons ionize and become free carriers.<sup>7</sup> This represents the density where the system transitions from an exciton to an EHP regime, and the result is an overall shift of the band to lower energy. This occurs in part, because the Pauli principle forbids electrons with parallel spin to occupy the same unit cell.<sup>38</sup> The distance between those electrons thus increases, reducing the Coulombic repulsive energy between them, and lowering the total energy of the system. Furthermore, the probability of finding an electron near a hole (and vice versa) is higher than finding two like charges in the same vicinity. The result is a stabilization of the plasma and a further decrease of the system energy. This process is collectively known as band-gap renormalization (BGR).<sup>7</sup>

With the increase in the band-edge emission due to EHP formation, there is a corresponding decrease in defect emission. This is due to charges ionizing out of the defects in the presence of the EHP.

### **1.3 Chapter Overview**

**Chapter 1** contains a brief overview of the relevant processes to the results discussed in the experimental chapters.

The primary methods used in the experiments described herein are two-photon and second harmonic generation microscopy. While both are nonlinear processes, they are



fundamentally different. A detailed introduction on the physical processes associated with these techniques followed by their implementation in microscopy is provided in **Chapter 2**.

The instrument utilized in our experiments is home-built and its development represents a major portion of the efforts described in this dissertation. **Chapter 3** presents a brief overview of the optical setup, followed by a detailed discussion of each major component. Specifically, the laser system, optical isolation, pulse dispersion control, variable attenuation and beam expansion represent the discussion of the major components preceding the objective. A discussion of the optical properties of the objective follow; including numerical aperture, working distance and depth of field, as well as theoretical and empirical determination of the resolution, in the presence and absence of beam truncation. The components of the emission detection setup are discussed next. This includes magnification for CCD camera imaging, a discussion of the monochromator and photomultiplier tube, and the data acquisition process. The chapter ends with a discussion of our efforts to synthesize different ZnO shapes, including hydrothermal, solution phase and chemical vapor deposition methods.

**Chapter 4** details the results of our analysis on carrier dynamics in the presence and absence of a high defect density in a single ZnO rod. Our observations in the steady state and time-dependent spectra before and after sample annealing are presented. We also consider the conflicting reports on defect chemistry in ZnO and suggest which mechanisms are giving rise to our observation.

In **Chapter 5** we consider the differences in carrier behavior at specific regions within a single structure. Defect annealing is conducted at a series of temperatures to probe the effect of a changing defect density on carrier dynamics. A comparison of the results from

different regions indicates a dependence on structure location. We discuss the physical processes that give rise to these observations.

**Chapter 6** presents the results from experiments that test if there is a dependence on electron-hole plasma formation with structure location. We find that the efficiency is higher for this process at the end of the rod and consider the possible mechanisms.

## 1.4 References

1. E. Barkai, G. Margolin, *Israel Journal of Chemistry* **2004**, 44, 353.
2. F. Kulzer, M. Orrit, *Annual Review of Physical Chemistry* **2004**, 55, 585.
3. X. Michalet, A. N. Kapanidis, T. Laurence, F. Pinaud, S. Doose, M. Pflughoeft, S. Weiss, *Annual Review of Biophysics and Biomolecular Structure* **2003**, 32, 161.
4. B. Schuler, *Chemphyschem* **2005**, 6, 1206.
5. T. Plakhotnik, E. A. Donley, U. P. Wild, *Annual Review of Physical Chemistry* **1997**, 48, 181.
6. X. S. Xie, J. K. Trautman, *Annual Review of Physical Chemistry* **1998**, 49, 441.
7. C. Klingshirn, *Semiconductor Optics*, Third ed., Springer-Verlag, Berlin, **2007**.
8. A. B. Djuricic, Y. H. Leung, *Small* **2006**, 2, 944.
9. J. C. Johnson, H. Q. Yan, P. D. Yang, R. J. Saykally, *Journal of Physical Chemistry B* **2003**, 107, 8816.
10. L. K. van Vugt, S. Ruhle, P. Ravindran, H. C. Gerritsen, L. Kuipers, D. Vanmaekelbergh, *Physical Review Letters* **2006**, 97.
11. L. Schmidt-Mende, J. L. MacManus-Driscoll, *Materials Today* **2007**, 10, 40.
12. S. M. Al-Hilli, M. Willander, A. Ost, P. Stralfors, *Journal of Applied Physics* **2007**, 102.
13. M. Grundmann, H. Frenzel, A. Lajn, M. Lorenz, F. Schein, H. von Wenckstern, *Physica Status Solidi a-Applications and Materials Science*, 207, 1437.
14. U. Ozgur, Y. I. Alivov, C. Liu, A. Teke, M. A. Reshchikov, S. Dogan, V. Avrutin, S. J. Cho, H. Morkoc, *Journal of Applied Physics* **2005**, 98.
15. D. M. Bagnall, Y. F. Chen, Z. Zhu, T. Yao, S. Koyama, M. Y. Shen, T. Goto, *Applied Physics Letters* **1997**, 70, 2230.
16. D. C. Look, *Materials Science and Engineering B-Solid State Materials for Advanced Technology* **2001**, 80, 383.
17. M. Law, L. E. Greene, J. C. Johnson, R. Saykally, P. D. Yang, *Nature Materials* **2005**, 4, 455.

18. J. K. Song, U. Willer, J. M. Szarko, S. R. Leone, S. Li, Y. Zhao, *Journal of Physical Chemistry C* **2008**, *112*, 1679.
19. J. C. Johnson, K. P. Knutsen, H. Q. Yan, M. Law, Y. F. Zhang, P. D. Yang, R. J. Saykally, *Nano Letters* **2004**, *4*, 197.
20. Z. L. Wang, *Journal of Physics-Condensed Matter* **2004**, *16*, R829.
21. Z. Y. Fan, J. G. Lu, *Journal of Nanoscience and Nanotechnology* **2005**, *5*, 1561.
22. S. W. Liu, H. J. Zhou, A. Ricca, R. Tian, M. Xiao, *Physical Review B* **2008**, *77*.
23. S. K. Kurtz, T. T. Perry, *Journal of Applied Physics* **1968**, *39*, 3798.
24. U. Neumann, R. Grunwald, U. Griebner, G. Steinmeyer, W. Seeber, *Applied Physics Letters* **2004**, *84*, 170.
25. A. B. Djuricic, W. M. Kwok, Y. H. Leung, D. L. Phillips, W. K. Chan, *Journal of Physical Chemistry B* **2005**, *109*, 19228.
26. R. Prasanth, L. K. Van Vugt, D. A. M. Vanmaekelbergh, H. C. Gerritsen, *Applied Physics Letters* **2006**, *88*.
27. A. van Dijken, E. A. Meulenkaamp, D. Vanmaekelbergh, A. Meijerink, *Journal of Luminescence* **2000**, *87-9*, 454.
28. T. Matsumoto, H. Kato, K. Miyamoto, M. Sano, E. A. Zhukov, T. Yao, *Applied Physics Letters* **2002**, *81*, 1231.
29. S. S. Hong, T. Joo, W. I. Park, Y. H. Jun, G. C. Yi, *Applied Physics Letters* **2003**, *83*, 4157.
30. E. Irene, *Electronic Materials Science*, John Wiley & Sons, Hoboken, **2005**.
31. F. Williams, *Physica Status Solidi* **1968**, *25*, 493.
32. A. Janotti, C. G. Van de Walle, *Physical Review B* **2007**, *76*.
33. M. D. McCluskey, S. J. Jokela, *Journal of Applied Physics* **2009**, *106*.
34. U. Siegner, M. Achermann, U. Keller, *Measurement Science & Technology* **2001**, *12*, 1847.
35. J. M. Szarko, J. K. Song, C. W. Blackledge, I. Swart, S. R. Leone, S. H. Li, Y. P. Zhao, *Chemical Physics Letters* **2005**, *404*, 171.

36. N. Arai, J. Takeda, H. J. Ko, T. Yao, *Journal of Luminescence* **2006**, *119*, 346.
37. Y. H. Leung, W. M. Kwok, A. B. Djurisic, D. L. Phillips, W. K. Chan, *Nanotechnology* **2005**, *16*, 579.
38. H. Ando, H. Oohashi, H. Kanbe, *Journal of Applied Physics* **1991**, *70*, 7024.

## **CHAPTER 2**

### **An Introduction to Two-Photon and Second Harmonic Generation Microscopy**

The utilization and probing of fluorescence as a tool in scientific experimentation has been revolutionary. Applications to microscopy enable the visualization of microscopic processes rendered otherwise invisible. In spectroscopy, monitoring the changes in microscopic absorption and emission signatures leads to detailed descriptions of electronic and molecular dynamics. However, the use of fluorescence in spectroscopy and microscopy is not new and improvements in the technique are constantly being made.

Over the past decade, there has been a flurry of research in the application of non-linear optical techniques to microscopy. These methods provide many advantages over conventional techniques and can yield novel information from a variety of systems. While the different types of methods abound, the focus of the work described herein is on two-photon and second harmonic generation microscopy. Coupling the two techniques (microscopy and spectroscopy) to study fluorescence yields a powerful tool for visualizing the changes in electronic dynamics as they occur in real time, and is one of the main themes in this dissertation. Therefore this chapter will be split into two sections. Section 2.1 will describe the theory and techniques of two-photon microscopy (TPM), and Section 2.2 will be a similar overview of second-harmonic generation microscopy (SHGM).

## **2.1 Two-Photon Fluorescence**

In 1931 Marie Goppert-Mayer predicted that an atom or molecule should be able to simultaneously (within  $10^{-16}$ - $10^{-17}$ s) absorb two or more photons whose combined energy is equivalent to a one-photon absorption (Figure 2.1).<sup>1, 2</sup> Physically, this occurs with the promotion of an electron from the ground state to a virtual intermediate state following the first photon absorption.<sup>3,4</sup> Here, the virtual level is defined as the combined energy of the

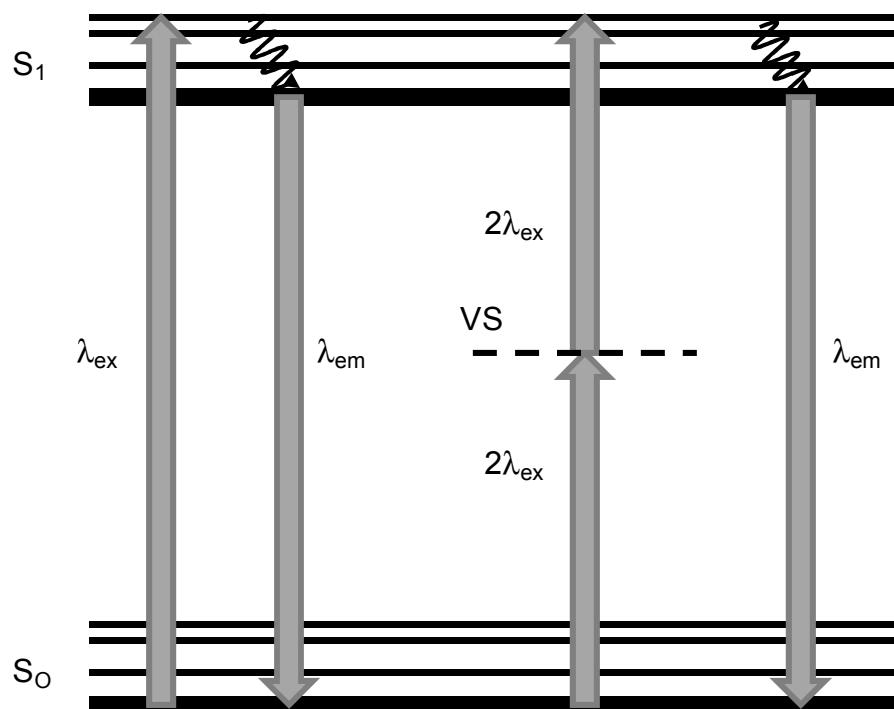


**Figure 2.1:** Jablonski diagram showing a one and two-photon excitation transition. Two-photon absorption occurs almost simultaneously. The absorption of the first photon promotes the electron to a virtual state (VS) followed by the second photon that completes the transition to the excited state. The emission frequency is the same for both processes.

photon with the energy states of the atom.<sup>5</sup> Promotion to the excited state occurs with absorption of the second photon through a vibronic coupling interaction.<sup>6</sup> Assuming the atom or molecule is fluorescent, it will emit a single photon whose energy is not dependent on the method of excitation (Figure 2.1). In TPM, the precondition that two photons must be absorbed simultaneously leads to a quadratic dependence of the emission intensity on the strength of the excitation (i.e. doubling the excitation intensity increases emission four-fold).<sup>2, 6-8</sup> This has important consequences for applications in TPM as shall be discussed in further detail later.



The process of fluorescence excitation can be described as the interaction between a radiative system and an electromagnetic field of sufficient energy to induce an electronic transition (i.e. greater than or equal to the energetic distance between the ground and first excited states). While the emission energy is the same for one and two-photon processes, the selection rules governing their excited state transitions are different. This arises because the transition moment in a one-photon excitation dictates that the initial and final states will have opposite parity (absorption changes the parity of the state), while the transition moment in a two-photon process dictates they will be equal.<sup>2</sup>

Practically, the different selection rules mean that one and two-photon excitation processes will result in different spectral absorption regions. However, a good estimate of the two-photon absorption spectrum is to double that of the one-photon, although deviations from this rule are not unusual.<sup>7</sup> In these cases the absorption spectrum is usually described by a two-photon ‘action’ cross-section ( $\sigma_{2p}$ ), which is the product of the fluorescence quantum yield ( $\phi_F$ ) and the temporal width of the laser pulse within the excitation volume.<sup>7</sup> Calculating  $\sigma_{2p}$  is not as simple as determining one-photon absorption spectra, because the probability of a two-photon absorption is so low. A detailed explanation can be found in a paper published by Xu et al.<sup>9</sup>

### *2.1.1 Two-photon microscopy*

In an experimental setup, the way to increase the two-photon absorption probability is to confine the photons both spatially and temporally. In microscopy the spatial constraints are achieved using an objective lens and the photons are temporally confined using a pulsed laser source. Increasing the probability by spatially focusing the beam to a diffraction limited spot gives rise to absorption that only occurs at the focal point of the objective (Figure 2.2). This

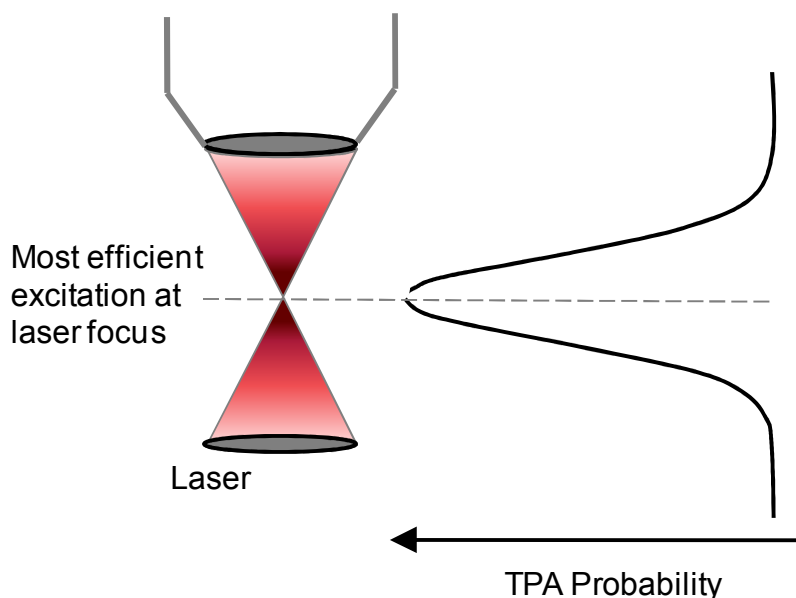


**Figure 2.2:** Schematic depicting the increasing probability of two-photon absorption at focal point of the objective.

contrasts with one-photon excitation experiments where absorption/emission occurs everywhere light interacts with the sample. An image contrasting the two processes can be found in reference #7.

The occurrence of absorption only at the objective focal point affords two-photon microscopy several advantages over other conventional techniques. Since no light is generated outside the objective focal point there is little to no background, leading to a high signal to noise ratio. Additionally, this can be useful for those interested in conducting optical sectioning experiments, where images can be collected at different focal planes along the z-axis.<sup>6, 8, 10-12</sup> The results from each focal plane can be combined to produce a three dimensional image. An example of this cross-sectioning capability can be seen in the two-photon fluorescence image of Nile Red beads (Invitrogen, Molecular Probes) ( $2\text{ }\mu\text{m}$  Ø) in Figure 2.3. The two beads in the center appear lower in intensity and have a smaller

diameter, implying they are sitting above the surrounding beads. An additional example of optical sectioning can be found in Chapter 4

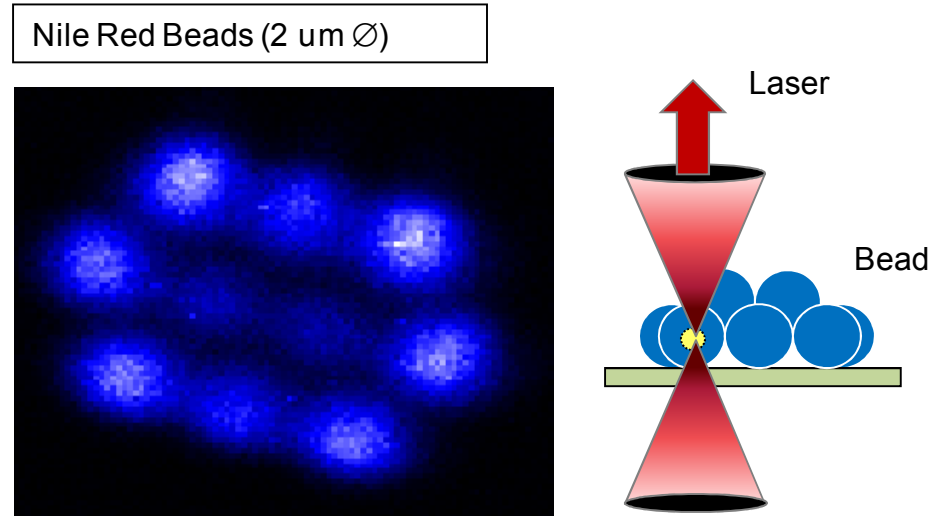


**Figure 2.3:** Example of the optical sectioning capability in two-photon microscopy. The two-photon emission image on the left is of 2  $\mu\text{m}$  beads infused with Nile-Red. The two beads in the center appear dimmer and have a smaller diameter, suggesting they are above the other beads as depicted on the right.

where steady-state spectra collected from different focal planes in a single ZnO rod are compared to each other.

### 2.1.2 Comparison of two-photon and confocal microscopy

Perhaps the technique that most closely matches this capability, and is often compared to TPM, is confocal microscopy (CM).<sup>6, 7</sup> This method is often utilized in optical sectioning experiments that employ a one-photon excitation. Fluorescence generated outside the objective focal point is eliminated by placement of an aperture along the emission path.<sup>13</sup> The aperture rejects out-of-plane fluorescence, transmitting only the light emanating from the objective focal point. While not the subject of this dissertation, a comparison of CM vs. TPM

is often discussed, so it is useful to briefly mention the advantages and disadvantages of each technique.

From an instrument development perspective, perhaps the clearest advantage of TPM is the elimination of the aperture since the only light generated is from the objective focal point. Placement of the aperture is critical in CM, otherwise the emission from the focal point could easily be rejected. Additionally, since each photon in a TPM experiment must be half the energy (twice the wavelength) of a one-photon technique, the excitation source is generally in the infrared. Experiments utilizing a UV excitation source require specialized optics (glass absorbs UV light) and a UV objective, which are generally more expensive. Ultraviolet light can also cause sample damaging because of the higher energy radiation (this is especially true for experiments with biological tissue), whereas the opposite is true for the lower energy infrared light in TPM.

Perhaps the most commonly cited disadvantage in TPM is the requirement of a pulsed laser source which is generally much greater in price than conventional illumination sources (such as low-cost, continuous wave lasers (i.e. HeNe lasers) and bulbs with filters) used in one-photon experiments.<sup>7</sup> Ultimately, there are no clear advantages that make one technique an obvious choice over the other. Careful consideration should be given in the context of the proposed experiment. For the experiments described herein, there was ready availability to a pulsed laser source and optics that operate in the visible and infrared regions of the spectrum. High signal to noise (S/N) ratio was also paramount for the detection regimes utilized.

### *2.1.3 Determining a Microscope's Resolution*

Another difference worth mentioning between the two techniques is the size of the focal volume. The resolution of a microscope is due in part to the size of the beam at the

focal point of the objective (also called the spot size), which is largely determined by the numerical aperture (NA) of the objective (discussed in more detail in Chapter 3). In a one-photon microscopy (OPM) experiment the morphology of the spot takes on an Airy disc pattern. The resolution is determined by the diameter (D) of the first minimum of the Airy pattern (Figure 2.4) and can be calculated using:<sup>13</sup>

$$D = 2.44 \frac{\lambda}{2(NA)} \quad (1)$$

where  $\lambda$  is the wavelength of the excitation. The diameter of the spot represents the limit in which two separate objects can be accurately resolved. It is clear from this equation that as  $\lambda$  increases, so does the diameter of the spot. Therefore, the immediate implication is that the resolution of TPM will be twice as bad as a OPM technique (such as CM). This observation is based on the assumption that the pinhole used in the confocal system is infinitely small.<sup>12</sup> Practically the limit is much larger and as the aperture diameter is increased, the resolution of a confocal system starts to decrease.

The illumination point spread function (IPSF(x,y,z)), which is defined as the intensity at the objective focal point, needs to be determined to calculate the resolution of a TPM.<sup>7</sup> Since there is a quadratic dependence on illumination intensity, the resolution is more accurately described using an IPSF<sup>2</sup> function. The distribution of intensity at the focal point can be fit to a Gaussian function so that the following equations can be used to obtain the lateral (xy) and axial (z):<sup>7</sup>

$$\frac{1}{e_{xy}} = \frac{0.320\lambda}{\sqrt{2}NA} \quad NA \leq 0.7 \quad (2)$$

$$\frac{1}{e_{xy}} = \frac{0.320\lambda}{\sqrt{2}NA^{0.91}} \quad NA \geq 0.7 \quad (3)$$

$$\frac{1}{e_z} = \frac{0.532\lambda}{\sqrt{2}} \left[ \frac{1}{n - \sqrt{n^2 - NA^2}} \right] \quad (4)$$

Here  $1/e$  corresponds to the width of the  $IPSF^2$  function,  $\lambda$  is the excitation wavelength,  $NA$  is the objective numerical aperture and  $n$  is the refractive index of the medium between the sample and objective ( $n=1$  for dry objectives). Equation three can be utilized when the objective  $NA$  is below 0.7. Here the lateral resolution is inversely proportional to  $NA$ . However, as the  $NA$  is increased, there is a slight deviation from this relation and a more accurate result is obtained by assuming an inverse power dependence on  $NA$ .<sup>7</sup> Once these numbers have been obtained the excitation volume ( $V$ ) can be calculated using:<sup>7</sup>

$$V = \pi^{3/2} \gamma_{xy}^2 \gamma_z \quad (5)$$

The values obtained using these equations are good approximations but the actual resolution can be empirically determined by scanning an object smaller than the theoretical diffraction limit of the excitation wavelength. Lastly, these calculations are only accurate if the input aperture of the objective is completely overfilled with light. This phenomenon is true in any microscopy experiment and will be detailed later in Section 3.2.

TPM has become a popular technique and is utilized in many different areas of science.<sup>2, 8, 14-17</sup> Perhaps equally important is second harmonic generation microscopy.<sup>6, 18</sup> This non-linear technique affords many unique advantages and is detailed in the following section.

## 2.2 Second Harmonic Generation

In contrast to two-photon absorption processes, second-harmonic generation (SHG) is a non-absorption process and involves an interaction between an oscillating electro-magnetic

field (light) and matter. As the name implies, the process describes the generation of light at exactly twice the fundamental frequency:

$$k(2\omega) = 2k(\omega) \quad (6)$$

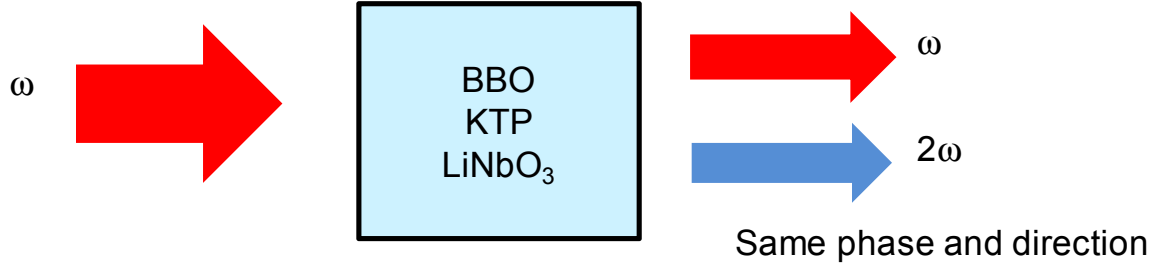


**Figure 2.4:** Schematic depiction of second harmonic generation in birefringent crystals. Here BBO is beta barium borate, KTP is potassium titanyl phosphate and LiNbO<sub>3</sub> is lithium niobate.

The physical process is depicted in Figure 2.4, and can be described as a photon exchange where fundamental photons of frequency  $\omega$  are annihilated, simultaneously giving rise to a photon with twice the fundamental frequency ( $2\omega$ ).<sup>5</sup>

The general properties of SHG are that it is generated at an orthogonal polarization to the fundamental, but propagates in the same phase and direction. The efficiency of the process is determined largely by properties of the material, which can be described using a second order susceptibility tensor ( $\chi^{(2)}$ ). The details of SHG and other pertinent non-linear phenomena is the subject of many good textbooks and the reader is referred to them for a rigorous explanation.<sup>3, 5, 19</sup> The purpose of the following section is to provide a brief overview of the conditions required for SHG, and its implementation in microscopy. Perhaps the best place to begin is with a discussion of the necessary properties of the material.

### 2.2.1 Noncentrosymmetry and Optical Susceptibility

Maxwell's equations dictate that when light of frequency  $\omega$  propagates through a medium, it will induce the dipoles in the medium to oscillate at the same frequency. A precondition to SHG is that the material must display non-centrosymmetry.<sup>5, 19</sup> In

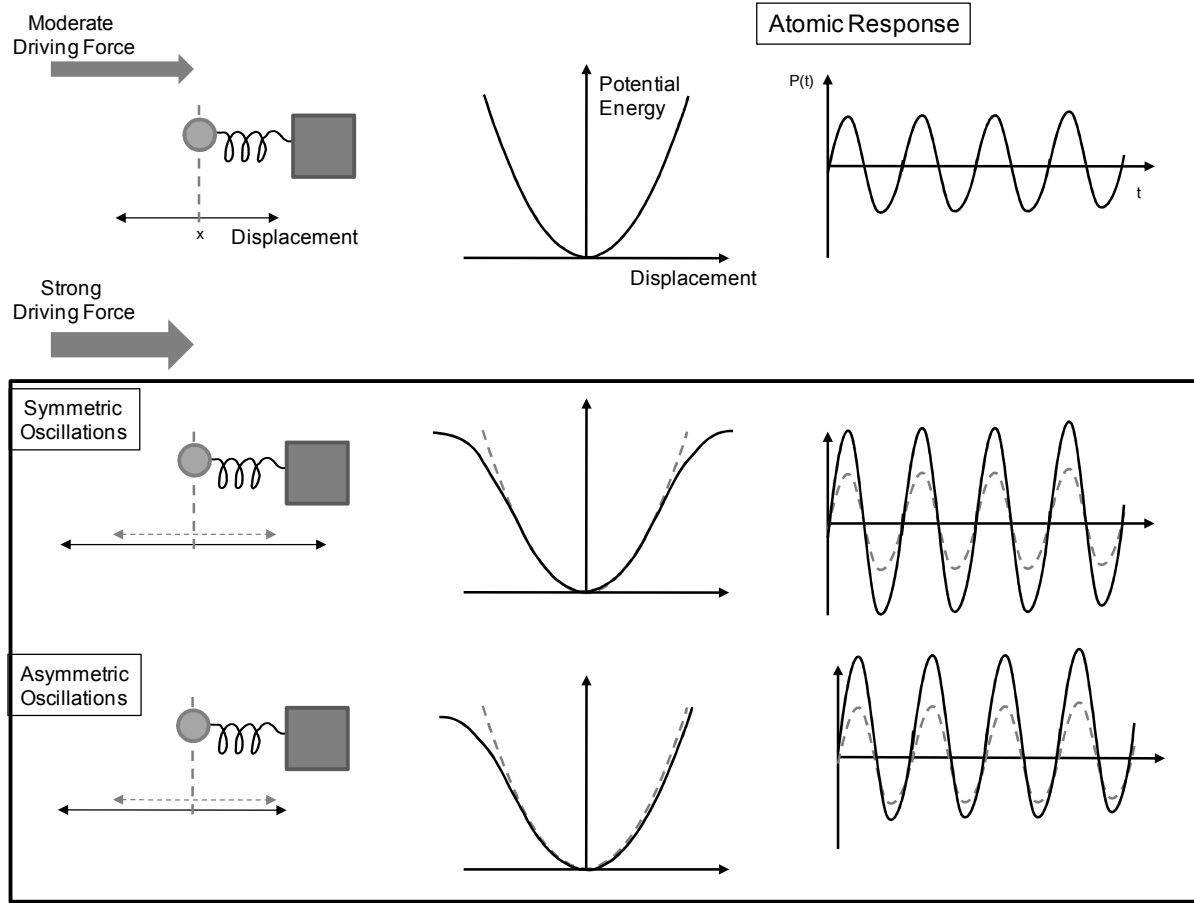


**Figure 2.5:** The atomic polarization response in the presence of a moderate and strong driving force (i.e. the electric field). The example of a ball on a spring is used to illustrate the dipole displacement in symmetric and asymmetric oscillations (as would be expected in noncentrosymmetric materials). The oscillations are described in terms of harmonic oscillator potentials (center) and the associated waveforms are shown on the right.

this case, the fundamental propagating through the material induces dipoles which respond by oscillating asymmetrically (in contrast to the symmetric oscillations of a centrosymmetric medium). As the intensity of the fundamental increases, the oscillations increase in magnitude and generate light that is exactly twice the fundamental frequency. Similar to two-



photon emission, there is a nonlinear dependence on the fundamental intensity that scales quadratically with the applied optical field.<sup>3, 5, 19</sup>

It can be instructive to think of the dipole oscillations as being analogous to a ball on a spring. In the symmetric case, as the spring is stretched to some initial point  $x$ , the oscillations around  $x$  are symmetric with equal sinusoidal amplitudes. In an asymmetric case, where the driving force is strong, there is a nonlinearity in the restoring force on the spring.<sup>5</sup> Consequently, the oscillations around  $x$  become unequal with asymmetric sinusoidal amplitudes. This would be analogous to an anharmonic oscillator potential where one side of the parabola has a different slope than the other (Figure 2.5). The non-linearity of a material is therefore a measure of its ability to generate second harmonic radiation, and is generally described by a second-order nonlinear optical susceptibility ( $\chi^{(2)}$ ).

To better describe the nonlinearity of a material, it is useful to consider how the dipole moment per unit volume, or polarization ( $P(t)$ ) of the material, depends on the strength of the applied optical field ( $E(t)$ ). In the case of linear optics,  $P(t)$  depends linearly on  $E(t)$  and can be described using:<sup>5</sup>

$$P(t) = \epsilon_0 \chi^{(1)} E(t) \quad (7)$$

where  $\epsilon_0$  is the vacuum permittivity in free space and  $\chi^{(1)}$  is the linear susceptibility tensor.

This equation can be represented by expressing  $P(t)$  as a power series:<sup>5</sup>

$$P(t) = \epsilon_0 [\chi^{(1)} E(t) + \chi^{(2)} E^2(t) + \chi^{(3)} E^3(t) + \dots] \quad (8)$$

where  $\chi^{(2)}$  is the second-order, and  $\chi^{(3)}$  is the third-order non-linear susceptibility tensors. The third order susceptibility can occur in centrosymmetric and noncentrosymmetric media. It gives rise to third harmonic generation and has also been utilized in microscopy experiments.<sup>20-24</sup> Higher order terms also give rise to higher order harmonics, but as they are

not the subject of the work described herein, our focus will be on SHG. The second-order non-linear polarization can therefore be described by:

$$P^{(2)}(t) = \epsilon_0 \chi^{(2)} E^2(t) \quad (9)$$

Given that the electric field strength of a laser beam can be represented by:<sup>5</sup>

$$E(t) = E e^{-i\omega t} + c.c. \quad (10)$$

where *c.c.* represents the complex conjugate. Equation 9 becomes:

$$P^{(2)}(t) = 2\epsilon_0 \chi^{(2)} EE + (\epsilon_0 \chi^{(2)} E^2 e^{-i2\omega t} + c.c.) \quad (11)$$

Note here that the frequency component ( $2\omega$ ), which gives rise to SHG, is only represented in the second term of the equation. The first term is associated with a static electrical field that is created within the nonlinear medium.<sup>5</sup> While the magnitude of  $\chi^{(2)}$  can describe a material's propensity to generate second harmonic light, ultimately, non-centrosymmetry is not the only requirement to achieving SHG. In order for the process to be efficient the fundamental and SHG must also be in phase.

### 2.2.2 Phase Matching

To get appreciable SHG, the polarization waves generated by the oscillating dipoles of each atom interacting with the fundamental must be in phase.<sup>3</sup> In this case, the intensity increases with the length of the interaction. However, the phase-matching condition can often be difficult to achieve because the refractive index ( $n$ ) of most materials increases with incident frequency (known as normal dispersion).<sup>5</sup> Non-centrosymmetric materials that are able to circumvent this problem and give rise to efficient SHG are negative birefringent uniaxial crystals. The refractive index of these materials depends on the polarization of the incident radiation,<sup>5, 19</sup> and phase matching is achieved when the highest frequency wave is polarized with the lower of the two refractive indices.

Negative birefringent uniaxial crystals have a directionality associated with them, known as the optic or  $c$ -axis. Light polarized perpendicular to this axis is termed ordinary, and light polarized parallel is extraordinary. In these materials, the extraordinary polarization experiences a refractive index that is dependent on the angle between the  $c$ -axis and the propagation vector (also known as the  $k$ -vector, which describes the direction and magnitude of a propagating light wave).<sup>3, 5, 19</sup> The angle of the crystal is therefore tuned till phase matching is achieved. Practically, this becomes evident when the intensity of the SHG is maximized.

In non-centrosymmetric materials that do not display these properties, the second-harmonic light that is generated eventually falls out of phase with the fundamental and is lost to destructive interference. The distance in which the two beams are initially in phase is termed the coherence length, and it differs depending on the material. In bulk materials the loss in efficiency can be significant; however, with the advent of nanostructured materials in the past decade, the dimensions of the crystals often fall below the coherence length, making efficient collection of SHG possible. In the case of nanostructured materials, this process is made more efficient through the use of a microscope. Indeed, SHG has successfully been implemented in our lab<sup>25</sup> and is the topic of the next section.

### *2.2.3 Second Harmonic Generation Microscopy*

Since the equipment required to generate SHG is identical to what is required for two-photon absorption, second-harmonic generation microscopy is easily integrated with a TPM setup. Since SHG depends on the properties of the material, studying its radiation patterns and intensity distributions can yield a tremendous amount of information about the structure

and properties of microscopic systems. As in bulk systems, the propensity to generate second harmonic light can be described by the magnitude of the nonlinear susceptibility ( $\chi^{(2)}$ ).

#### 2.2.4 The Nonlinear Susceptibility Tensor in Microscopy

In three dimensions,  $\chi^{(2)}$  contains 27 elements and is represented by a three dimensional matrix. Each element represents a dimensional component in the material under study. The dimensions or symmetry components of the material define which elements of the susceptibility contribute to the overall signal. For example in the ZnO rods studied in the experiments described in Chapters 4-6, the polarization occurs along the z-axis (or *c*-axis) of the rod,<sup>26</sup> and the tensor element that is therefore responsible for SHG is  $\chi^{(2)}_{zzz}$ . In the case of surface contributions, the tensor element is  $\chi^{(2)}_{zxx}$ . In the context of our experiment, the fundamental is linearly polarized and therefore parallel to the *c*-axis. When the NA of the objective is less than 0.8, there is no effect on the fundamental polarization due to focusing by the objective. In our experiment the NA of the objective is 0.8 and so we expect no distortions in the polarization at the focal point.<sup>27</sup> As the NA increases above 0.8, the SHG efficiency begins to decrease.<sup>28</sup> However, since the incident beam is being focused to a microscopic spot the radiation field can no longer be treated as a plane wave and the nonlinearity is better described by individual molecular hyperpolarizabilities.<sup>28, 29</sup>

A rigorous description of the effect of focusing and the molecular hyperpolarizability can be found in an article published by Moreaux et al.<sup>28</sup> What follows is a brief description of the process, highlighting the main differences compared to SHG in bulk materials. It has been shown, that for nonlinear interactions the beam at the objective focal point is Gaussian in both the lateral and axial directions, differing from a collimated beam in that there is both

an amplitude variation and phase shift in the vicinity of the focal center.<sup>28, 29</sup> It can be expressed using:

$$E_{\omega}(x, y) = -iE_{\omega} \exp\left(-\frac{x^2}{w_x^2} - \frac{y^2}{w_y^2} + i\xi k_{\omega} x\right) \quad (12)$$

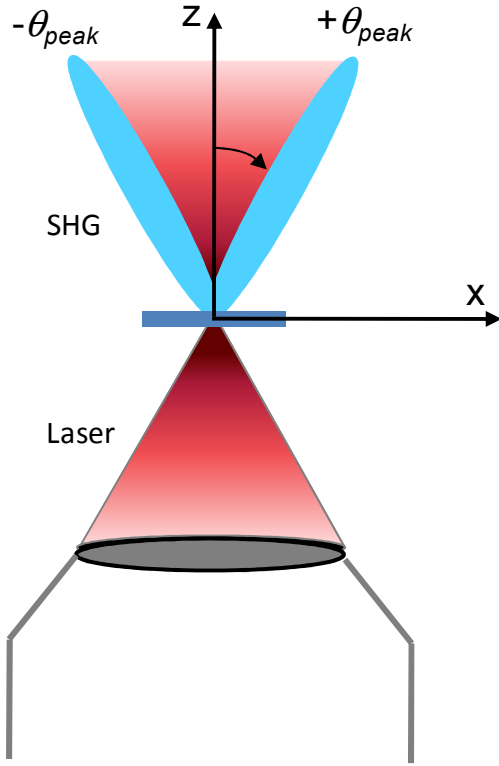


**Figure 2.6:** In microscopy the intensity of the focal spot takes on a Gaussian distribution. There is a phase shift close to focal center which leads to an increase in wavelength in that region. The SHG is therefore generated in two symmetric lobes to maintain a phase-matching condition.

where  $w_x$  and  $w_y$  are the beam waists in the axial and lateral dimensions, respectively,  $k_{\omega}$  is the wave vector and  $\xi$  describes the phase shift experienced by a Gaussian beam close to the focal center.<sup>28</sup> The resulting SHG represents a summation over all dipoles that interact with the incident electric field and can be represented by:

$$\mathbf{E}_{2\omega}(\theta, \varphi) = NA(\theta, \varphi) \mathbf{E}_{2\omega}^{(0)}(\theta, \varphi) \quad (13)$$

$$N = \frac{\pi}{2} w_x w_y N_D \quad (14)$$

$$A(\theta, \varphi) = \exp \left\{ -\frac{k_{2\omega}^2}{8} [w_x^2 (\cos \theta - \xi')^2 + w_y^2 (\sin \theta \sin \varphi)^2] \right\} \quad (15)$$

Here,  $\theta$  and  $\varphi$  are the angles used to describe the direction in which the SHG is radiated and  $\xi' = \xi n_\omega / n_{2\omega}$ . Physically,  $N$  is the total number of atoms or molecules that contribute to the overall SHG (where  $N_D$  is the molecular density within the focal volume), and  $A$  is an angular modulation term.<sup>28</sup> Of note in equation 13 is that the radiated SHG is a product of  $A(\theta, \varphi)$  and  $\mathbf{E}^{(0)}_{2\omega}(\theta, \varphi)$  (an elemental dipole radiator at the focal point). The incorporation of  $A(\theta, \varphi)$  gives rise to the SHG being radiated in two symmetric lobes at  $\theta_{\text{peak}} = \pm \cos^{-1}(\xi')$  (Figure 2.6). Physically, this arises because the phase shift in the vicinity of the focal center leads to an increase in wavelength and the SHG must be emitted at an angle to maintain a phase matching condition.<sup>29</sup> Practically, this must be taken into account in the construction of an SHGM to ensure that optics are placed close to the sample to account for the angles in which the SHG is radiated.

Two-photon and second-harmonic generation microscopy were the techniques utilized in the work described herein, and while the above explanations are by no means comprehensive, they provide a brief introduction to the science behind these techniques. What follows in Chapter 3 is a description of the microscope construction its major components.

## 2.3 References

1. M. Goppert-Mayer, *Annals of Physics* **1931**, 9, 273.
2. P. T. C. So, C. Y. Dong, B. R. Masters, K. M. Berland, *Annual Review of Biomedical Engineering* **2000**, 2, 399.
3. W. Demtroder, *Laser Spectroscopy*, 3rd ed., Springer, Berlin, **2003**.
4. J. R. Lakowicz, *Principles of Fluorescence Spectroscopy*, 3rd ed., Springer, New York, **2006**.
5. R. Boyd, *Nonlinear Optics*, 3rd ed., Elsevier, Oxford, **2008**.
6. A. Diaspro, G. Chirico, M. Collini, *Quarterly Reviews of Biophysics* **2005**, 38, 97.
7. W. R. Zipfel, R. M. Williams, W. W. Webb, *Nature Biotechnology* **2003**, 21, 1368.
8. K. König, *Journal of Microscopy-Oxford* **2000**, 200, 83.
9. C. Xu, J. Guild, W. W. Webb, W. Denk, *Optics Letters* **1995**, 20, 2372.
10. Y. Shao, J. Qu, H. Li, Y. Wang, J. Qi, G. Xu, H. Niu, *Applied Physics B-Lasers and Optics*, 99, 633.
11. A. Zoumi, A. Yeh, B. J. Tromberg, *Proceedings of the National Academy of Sciences of the United States of America* **2002**, 99, 11014.
12. M. Gu, C. J. R. Sheppard, *Journal of Microscopy-Oxford* **1995**, 177, 128.
13. P. Prasad, *Introduction to Biophotonics*, John Wiley & Sons, Hoboken, **2003**.
14. F. Helmchen, W. Denk, *Nature Methods* **2005**, 2, 932.
15. J. D. Bhawalkar, G. S. He, P. N. Prasad, *Reports on Progress in Physics* **1996**, 59, 1041.
16. T. Plakhotnik, E. A. Donley, U. P. Wild, *Annual Review of Physical Chemistry* **1997**, 48, 181.
17. G. Banfi, V. Degiorgio, D. Ricard, *Advances in Physics* **1998**, 47, 447.
18. R. D. Schaller, J. C. Johnson, K. R. Wilson, L. F. Lee, L. H. Haber, R. J. Saykally, *Journal of Physical Chemistry B* **2002**, 106, 5143.

19. D. M. Bagnall, Y. F. Chen, Z. Zhu, T. Yao, S. Koyama, M. Y. Shen, T. Goto, *Applied Physics Letters* **1997**, 70, 2230.
20. Y. Barad, H. Eisenberg, M. Horowitz, Y. Silberberg, *Applied Physics Letters* **1997**, 70, 922.
21. M. Muller, J. Squier, K. R. Wilson, G. J. Brakenhoff, *Journal of Microscopy-Oxford* **1998**, 191, 266.
22. J. A. Squier, M. Muller, G. J. Brakenhoff, K. R. Wilson, *Optics Express* **1998**, 3, 315.
23. D. Yelin, Y. Silberberg, *Optics Express* **1999**, 5, 169.
24. D. Debarre, W. Supatto, A. M. Pena, A. Fabre, T. Tordjmann, L. Combettes, M. C. Schanne-Klein, E. Beaurepaire, *Nature Methods* **2006**, 3, 47.
25. B. P. Mehl, R. L. House, A. Uppal, A. J. Reams, C. Zhang, J. R. Kirschbrown, J. M. Papanikolas, *Journal of Physical Chemistry A*, 114, 1241.
26. J. C. Johnson, H. Q. Yan, P. D. Yang, R. J. Saykally, *Journal of Physical Chemistry B* **2003**, 107, 8816.
27. R. M. Williams, W. R. Zipfel, W. W. Webb, *Biophysical Journal* **2005**, 88, 1377.
28. L. Moreaux, O. Sandre, J. Mertz, *Journal of the Optical Society of America B-Optical Physics* **2000**, 17, 1685.
29. J. Mertz, L. Moreaux, *Optics Communications* **2001**, 196, 325.



## **CHAPTER 3**

### **Experimental Description**

The purpose of this chapter is to describe the basic layout of the microscope and an explanation of the science behind each of the major components. It is intended as guide to our optical setup for new users and incoming graduate students to the laboratory. Section 3.1 will summarize the layout and design of the microscope and Section 3.2 will provide introductory descriptions of the major components and detail their specifications, beginning with the generation of light by the laser and ending with the emission detection system. Lastly, Section 3.3 describes the protocol development and results for ZnO synthesis experiments.

### **3.1 Microscope design**

A schematic diagram of the optical setup for the nonlinear microscope is shown in Figure 3.1. A picture of it is shown in Figure 3.2. Our setup consists of a modelocked Ti:Sapphire laser (Spectra Physics Tsunami) pumped by a 5W frequency doubled continuous-wave diode laser (Spectra Physics Millennia). The system produces pulses with an 80 fs width at a repetition rate of 76 MHz, and a tuning range between 720-850 nm with a maximum power output of approximately 1 W. The output is sent through a Faraday isolator to redirect reflected light away from the laser where it can extinguish mode locking. Light is then directed through a prism-pair compressor operated in a double pass configuration, to correct for pulse dispersion caused by spatial chirp and propagation through the objective. A half wave-plate and polarizing cube serve as a variable attenuator, enabling us to vary the average power to the microscope anywhere between 1 and 50 mW.

The microscope employs an inverted design with its objective located below the sample plane. The femtosecond laser beam is expanded by a lens pair, reflected off a dichroic mirror (R: 680-1000 nm, T: 360-650 nm) and then directed into the objective (Olympus

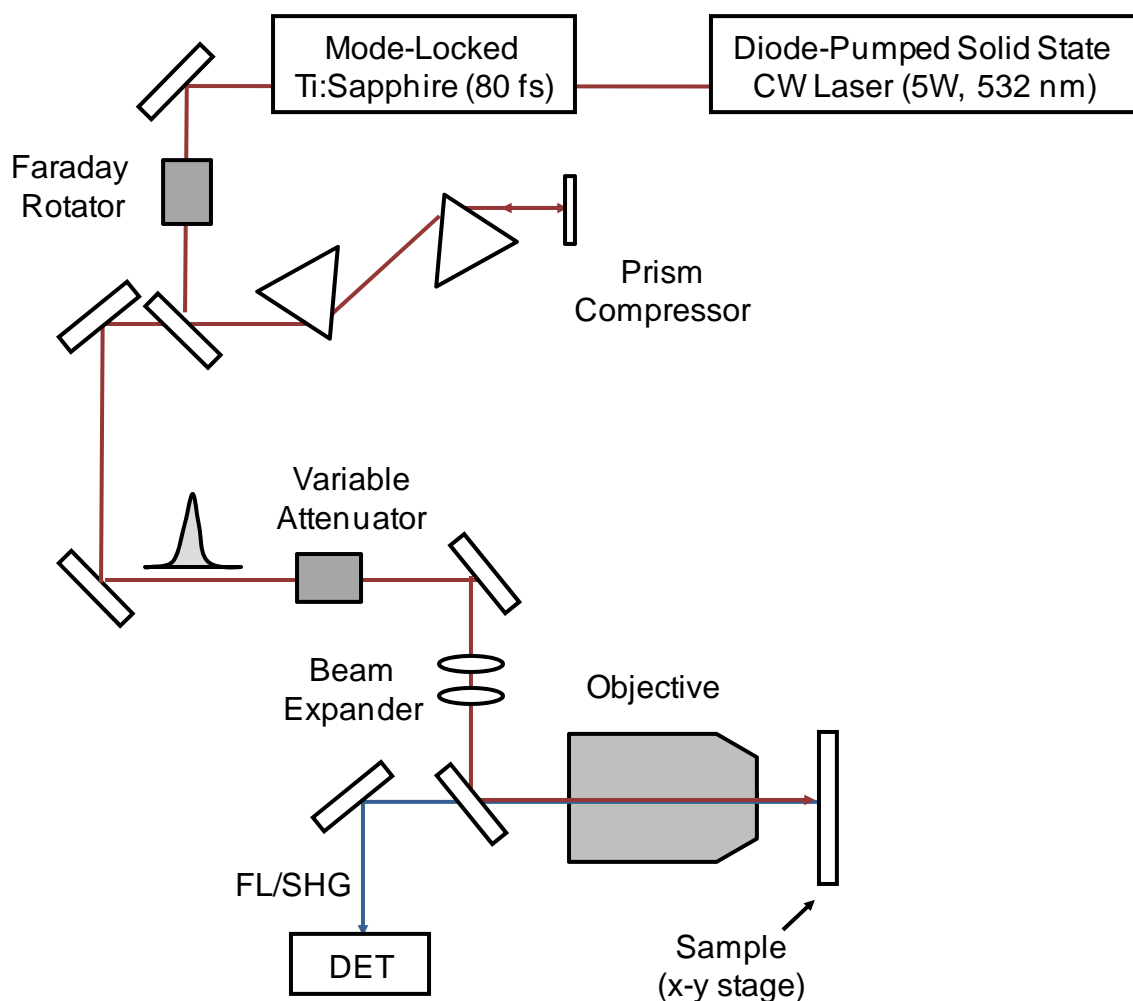


**Figure 3.1:** Schematic overview of our nonlinear microscope system. Excitation light is generated by a pulsed, femtosecond laser that is pumped by a CW diode-pumped laser (532 nm). The system generates pulses with an 80 fs width at a 76 MHz repetition rate. The output is sent through a Faraday rotator to prevent reflections from reaching the laser system. A prism compressor is used to correct for pulse dispersion. The power entering the microscope is controlled with a variable attenuator that consists of a waveplate and a polarization beam-splitter cube. Light is expanded 2x, to overfill the input aperture of the objective. The sample is raster scanned across the objective focal point and the resulting fluorescence/SHG is collected back through the objective, focused into the slit of a monochromator and detected by a photomultiplier tube.

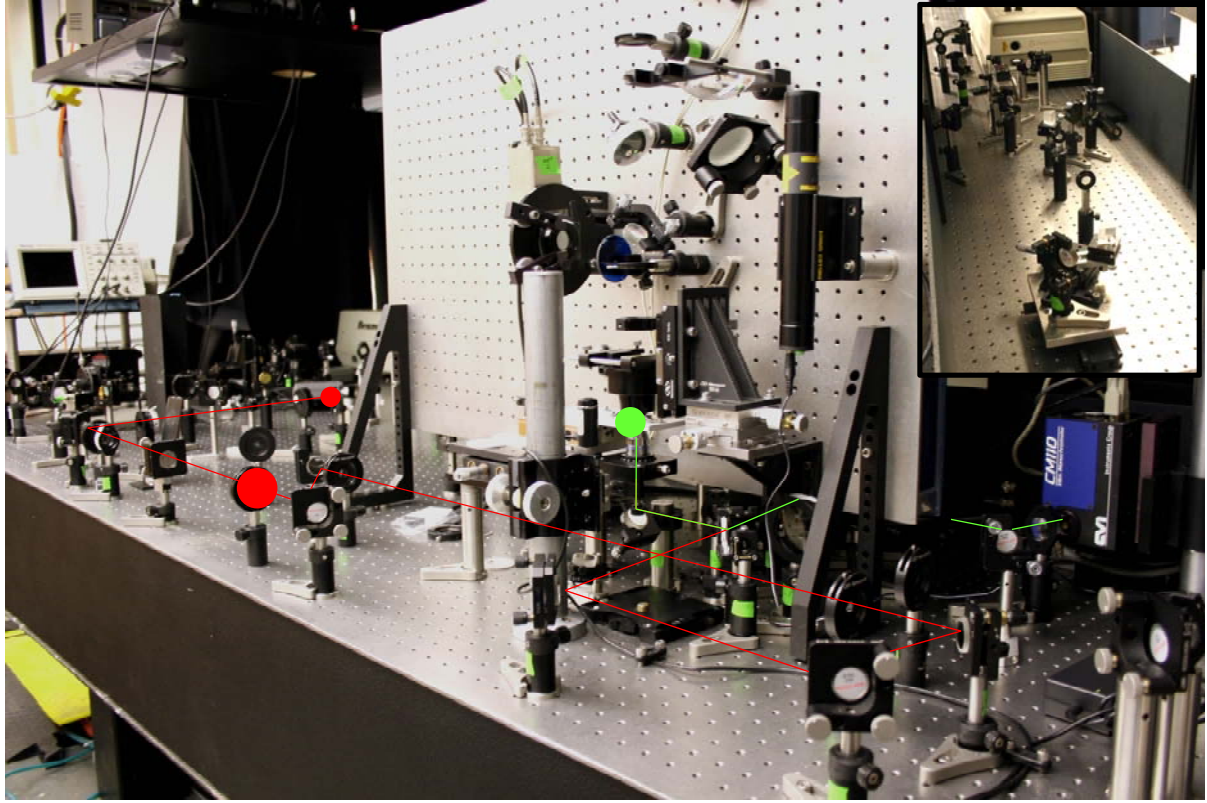


**Figure 3.2:** Photograph of our optical setup. The beam path is shown in red, and the fluorescence in green. The large red spot indicates beam expansion and the green spot indicates the objective focal point. An image of the prism compressor is shown in the upper right.

MSPlan 50x, NA 0.8), overfilling its input aperture. The sample is raster-scanned across the focal point of the objective using a piezoelectric x-y translation stage (Queensgate NPS3330 Controller/Stage System) with a step-size and reproducibility that are both less than 20 nm. Two-photon emission and second harmonic light emanating from the sample are collected by the objective. Light transmitted through the dichroic beamsplitter is focused onto the entrance slit of a monochromator (CVI CM110) and detected by a photomultiplier tube (PMT) (Hamamatsu) operated in a photon-counting mode. Under typical experimental conditions, the sample emits or generates a signal photon every 500 to 1000 laser pulses. The

PMT output is sent to a discriminator and a counter located on a data acquisition card (Model PCI 6602, National Instruments).

Samples are placed on a glass substrate with an etched grid so that individual structures examined in the optical microscope can be located in the scanning electron microscope (SEM), to obtain high-resolution structural images. In addition to the photon counting detection used for imaging, the emitted light can be directed into a time-correlated single-photon counting instrument<sup>1</sup> to obtain time-resolved emission data with an approximately 100 ps instrument response.

### **3.2 Major Components and their Specifications**

This section is laid out in the order of components the beam encounters, from the generation of excitation light from the laser, to the emission detection components and data acquisition.

#### *3.2.1 Laser Operation*

The term “laser” is an acronym for light amplification by stimulated emission of radiation. There are generally two types of emission, spontaneous and stimulated. Spontaneous emission involves the relaxation of an electron from a higher energy state to a lower one.<sup>2</sup> The energy that is given off in the process can either be emitted as heat in a non-radiative process or as a photon in a radiative transition. The rate that this occurs can be described by:

$$\frac{dN_2}{dt} = -\gamma_2 N_2 \quad (15)$$

where  $\gamma_2$  is the spontaneous energy decay rate from a higher energy state and  $N_2$  is the number of atoms in that state.<sup>3, 4</sup> Physically, atoms undergoing this process can be thought of

as an electric dipole antenna, radiating at the transition frequency. Each atom radiates independently with its own phase, the resulting emission is therefore incoherent.<sup>3</sup>

In contrast to this process, stimulated emission is characterized as being coherent in nature because the oscillations of each individual atom are defined by the applied signal.<sup>3</sup> In this process, atoms are first stimulated from a lower energy level into a higher one, at a rate that is proportional to the intensity (or photon density) of the signal. This is called stimulated absorption and can be described by:<sup>3,4</sup>

$$\frac{dN_2(t)}{dt} = Kn(t)N_1(t) \quad (16)$$

where  $n(t)$  is the photon density of the applied signal and  $K$  is a proportionality constant that represents the strength of the stimulated response. This will be greatest when the applied signal is tuned to the transition frequency.<sup>3</sup> In addition to stimulated absorption, the applied signal also stimulates atoms in a high energy state to relax into a lower state (stimulated emission). The dependence on photon density is the same and the energy that is released in the process goes into the applied signal, thereby amplifying it. This process is described by:

$$\frac{dN_2(t)}{dt} = -Kn(t)N_2(t) \quad (17)$$

In the case of stimulated absorption, energy is transferred from the applied signal to the atoms, thereby attenuating it. In stimulated emission, the opposite occurs and the signal is amplified. The change in the photon density can then be represented by:

$$\frac{dn}{dt} = -K[N_1(t) - N_2(t)]n(t) \quad (18)$$

where the dominating process (stimulated absorption or emission) will be indicated by the sign of the population difference,  $\Delta N(t) = N_1(t) - N_2(t)$ . When  $N_1(t) > N_2(t)$  it indicates stimulated absorption dominates, and vice versa. To achieve light amplification by stimulated

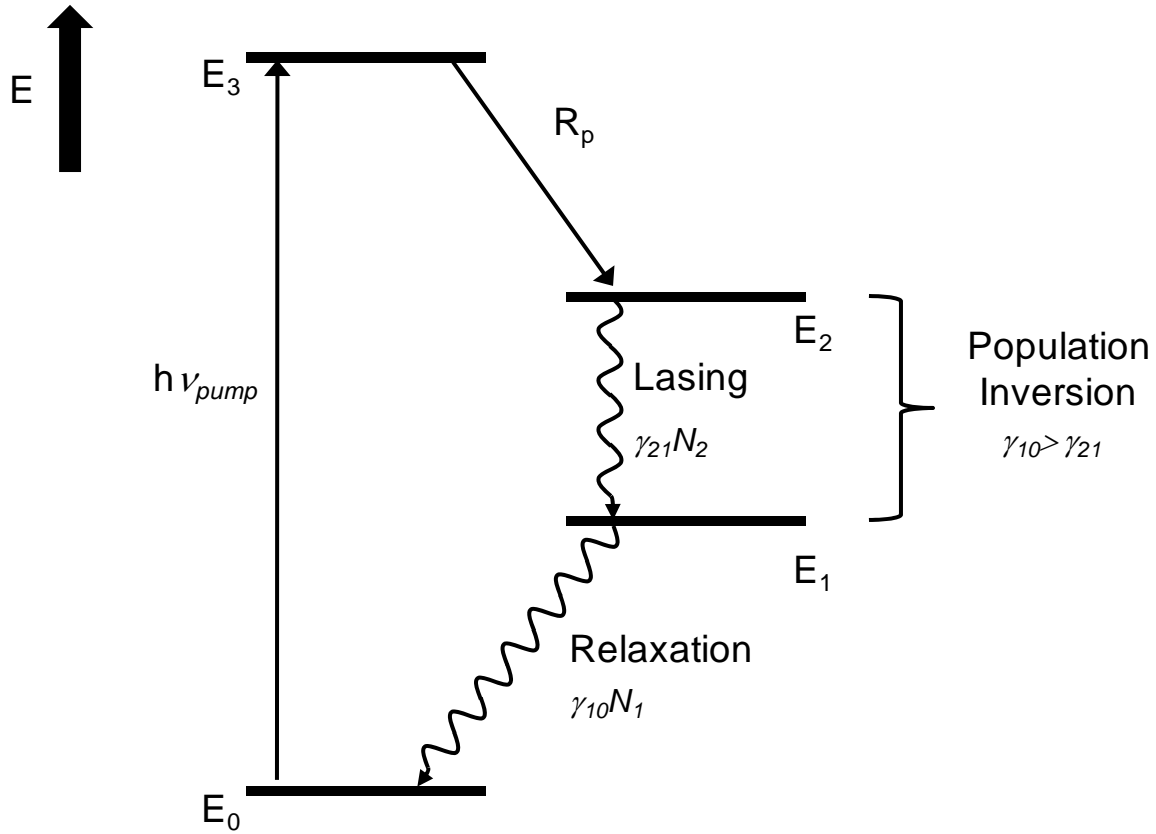


**Figure 3.3:** Four-level energy diagram depicting a population inversion condition that is a requirement for lasing.  $R_p$  is correlated with the pumping efficiency. As long as the relaxation from  $E_1$  to  $E_0$  is faster than  $E_2$  to  $E_1$  the number of carriers in  $E_2$  will be greater than  $E_1$ , creating the population inversion and enabling the amplification of stimulated emission (lasing). Adapted from Reference #3.

emission of radiation, the downward relaxation process must dominate over stimulated absorption ( $N_1(t) < N_2(t)$ ). This is achieved by creating a condition called population inversion, where the number of atoms in the higher energy state is greater than the lower. However, Boltzmann's Principle states that at thermal equilibrium, the higher energy state is always going to be less populated than the lower energy. Additionally, for every stimulated

absorption, there would be a corresponding stimulated emission, and the condition  $N_1(t) \geq N_2(t)$  cannot be overcome. It therefore becomes impossible to achieve a population inversion with just two states and a system with at least three states is required; in many cases the process is described using a four state system.

Shown in Figure 3.3 is a schematic of a four-level laser pumping system. According to Boltzmann's Principle, a majority of the atoms are going to exist in the lower energy state,  $E_0$ . If we then pump the medium at a rate  $R_{p0}$  with an energy source sufficient to promote electrons into the highest energy state ( $E_3$ ) (in our experiment, this source is the diode-pumped continuous-wave laser), we will create a population of which a fraction  $\eta_p$ , will eventually relax to  $E_2$ . The effective pumping rate can then be described by:<sup>3</sup>

$$R_p = \eta_p R_{p0} \quad (18)$$

and the rate equations governing relaxation into and out of level  $E_2$  and  $E_1$ :

$$\frac{dN_2}{dt} \approx R_p - \gamma_{21}N_2 \quad (19)$$

$$\frac{dN_1}{dt} \approx \gamma_{21}N_2 - \gamma_{10}N_1 \quad (20)$$

If the system reaches steady state equilibrium, the populations in each state can be solved by setting equations 19 and 20 equal to zero, yielding:

$$N_2 = \frac{R_p}{\gamma_{21}} \quad (21)$$

$$N_1 = \left( \frac{\gamma_{21}}{\gamma_{10}} \right) N_2 \quad (22)$$

The difference between the populations is then:



$$(N_2 - N_1) = \frac{R_p(\gamma_{10} - \gamma_{21})}{\gamma_{10}\gamma_{21}} \quad (23)$$

As can be seen from equation 23, when the rate of decay from  $E_1$  to  $E_0$  ( $\gamma_{10}$ ) is greater than the decay from  $E_2$  to  $E_1$  ( $\gamma_{21}$ ) the difference in populations is positive, indicating that a population inversion has been achieved. In essence, these are the requirements in order to stimulate emission and initiate lasing, the success of which is determined in part, by the pumping efficiency and power.<sup>3</sup>

### 3.2.2 The Laser System

The laser system used in our experiments consists of two lasers, a diode-pumped solid state laser (Spectra-Physics Millennia) and a Titanium: Sapphire (Ti:S) laser (Spectra-Physics Tsunami). The description of the pump laser's operation is relatively straightforward. Near-infrared light at 1064 nm is generated by pumping a neodymium yttrium vanadate (Nd:YVO<sub>4</sub>) crystal with two fiber-coupled diode bar modules. The resulting light is then frequency doubled by generating second-harmonic radiation in a Lithium Triborate crystal. The resulting continuous wave (CW) 532 nm light can be emitted at powers up to 6 W to pump a Sapphire crystal doped with Titanium (Ti:S).

The Ti:S crystal is at the heart of a mode-locked laser that generates pulses with an 80 fs width and 76 MHz repetition rate, which can be tuned between 720 and 850 nm. A basic diagram of the setup is shown in Figure 3.4. However, in its simplest form the laser cavity can be described as being composed of two end mirrors, the output coupler and high reflector. The high reflector is 100% reflective, and the output coupler is slightly transmissive, so with each round trip of the cavity a portion of the light transmits through the output coupler, representing the laser output. The length of the cavity is important because it determines the laser repetition rate, according to:

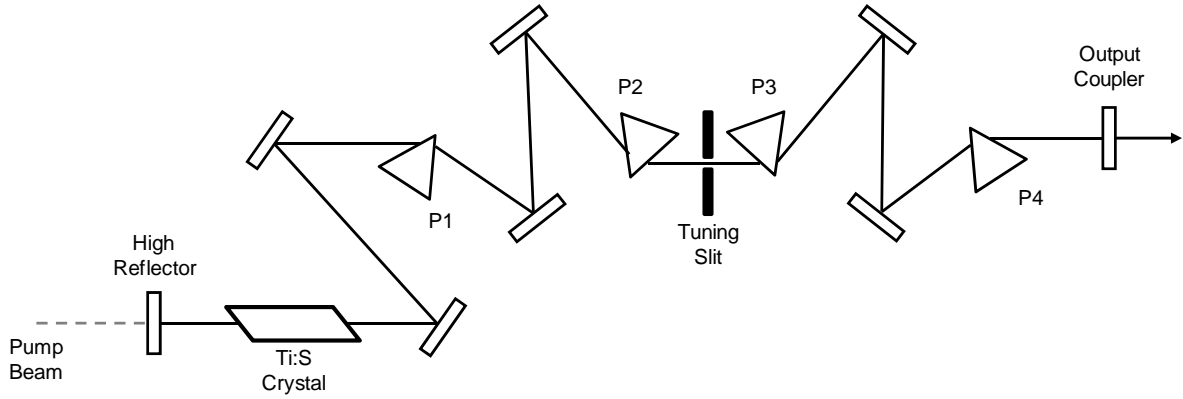


**Figure 3.4:** Basic optical layout of the Ti:S laser. The beam from the pump laser is focused into the Ti:S crystal and stimulates emission. Mode-locking is facilitated by sending the resulting laser beam through a slit, which can be adjusted to select different output frequencies. A prism compressor, consisting of four prisms corrects for pulse dispersion. Light oscillates between the high reflector and output coupler. Occasionally, some light transmits through the output coupler which represents the laser output.

$$\frac{2\omega L}{c} = q2\pi \quad (24)$$

where  $L$  is the length of the cavity,  $\omega$  is the laser frequency,  $c$  is the speed of light and  $q$  is an integer number. This equation dictates that the cavity length must be an integral multiple of the wavelengths at the oscillation frequency.<sup>3, 4</sup> The process creates a discrete set of resonant frequencies in the cavity that are spaced by:

$$\Delta\omega = 2\pi \frac{c}{2L} \quad (25)$$

The light generated by the Ti:S crystal consists of a range of different frequencies. As the frequencies oscillate in the cavity, those that don't meet the resonance condition are lost to destructive interference. Frequencies that match the resonance condition constructively

interfere with each other and are said to be “phase-locked” or “mode-locked,” creating a standing wave in the cavity.

### *3.2.3 Mode-Locking*

Mode-locking in the laser system used in our experiments is generally referred to as “passive mode-locking” meaning the process occurs within the cavity, independent of any external signal (in contrast to “active mode-locking”).<sup>3, 4</sup> As light is first produced in the cavity, all the components that are out of phase interfere with each other and create a lot of noise. Occasionally, an intense peak appears as a spike above the noise. These spikes are made up of several frequencies. Fourier relations dictate that temporal pulse width and frequency bandwidth (the number of modes contributing to a pulse) is inversely related. If the pulse width in time is very tight, then many different frequencies are contributing to that pulse. Conversely, if you only have a single mode, then the spread over time is large, constituting CW operation. Every time a spike occurs above the noise it removes gain from the medium and the overall loss of photons due to destructive interference starts to decrease. The spikes begin to be amplified at the expense of the other frequencies that are essentially running in CW operation. This continues until the only real frequencies that are being supported by the cavity are the mode-locked ones.

Mode-locking in our laser system is supported and enhanced by a Kerr-lens effect.<sup>4</sup> In this process the Ti:S rod acts as a focusing lens at high pump intensities. As the pump intensity increases, it changes the refractive index inside the Ti:S rod. Since the beam profile can be thought of as Gaussian in shape, this creates a refractive index gradient within the rod, which is essentially the definition of a lens. The process is illustrated in Figure 3.5. The emission from the focused region in the Ti:S rod is the most intense and therefore stimulates

emission and overall gain. However, those components not tightly focused essentially contribute to CW operation and need to be eliminated. The rejection of the unfocused light

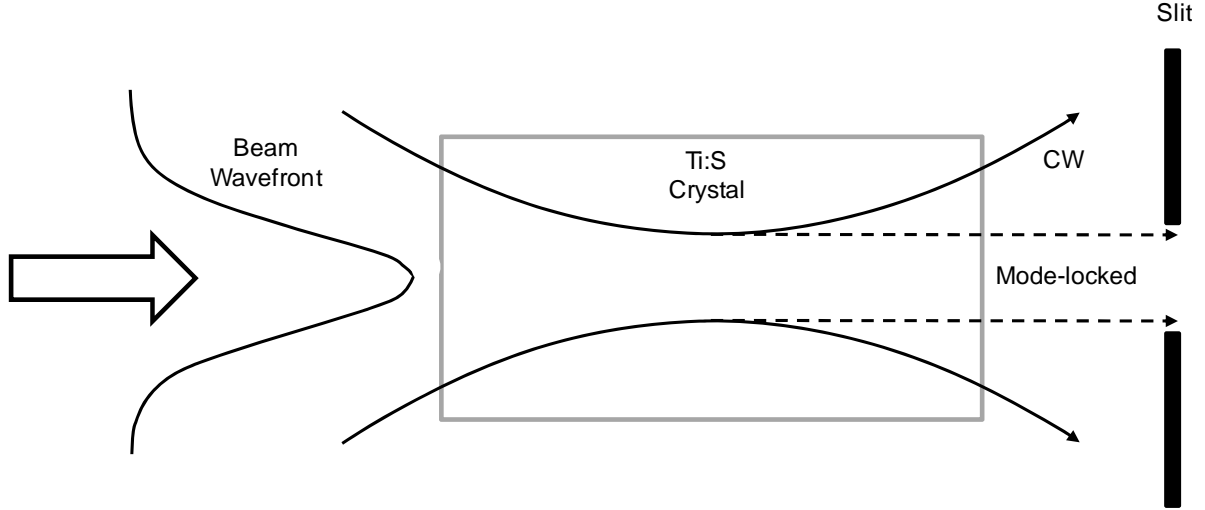


**Figure 3.5:** Passive mode-locking in the laser system occurs by a Kerr lens effect where the intensity across the beam wavefront causes a gradient in the index of refraction within the Ti:S crystal. Light generated at the focal point is the most intense and contributes to mode-locking. Light generated outside this area is in CW operation and is rejected by a slit, thereby enhancing the mode-locking process. Adapted from Reference # 4.

occurs by placing a slit within the laser cavity. By doing this, more photons contribute to stimulating emission and less loss in efficiency occurs because of CW operation.

The resulting pulses are separated in time according to:

$$\tau = \frac{2L}{c} \quad (25)$$

where  $\tau$  represents the amount of time it takes the pulse to make one round trip through the cavity.<sup>3, 4</sup> This value is directly related to the frequency spacing between the modes

$\left(\Delta\omega = \frac{1}{\tau}\right)$  As stated briefly above, the pulse width is determined by the number of modes

( $N$ ) that are oscillating in phase by the relation  $N\Delta\omega$ , which also represents the number of

frequency components (bandwidth) of the pulse. The width is also ultimately dictated by the pulse shape. For a Gaussian this relation can be represented as:

$$\Delta t = \frac{0.44}{N\Delta\omega} \quad (26)$$

The constant, 0.44, can vary with the width of the pulse according to the time-bandwidth product. This value is the result of multiplying the temporal and spectral pulse widths, and defines the minimum possible pulse duration for a given bandwidth.<sup>4</sup> Ultimately, as more and more frequencies contribute to the pulse, group velocity dispersion can begin to cause pulse broadening and become problematic.

#### *3.2.4 Group Velocity Dispersion and Prism Compression*

Group velocity dispersion defines the phenomenon where each frequency in a wave traveling through some medium has a different velocity.<sup>3</sup> This arises due to a decrease in medium's refractive index as the wavelength increases. Therefore, longer wavelengths generally travel faster than shorter ones, a condition known as positive dispersion (negative dispersion would be the opposite). The net effect is a broadening of the laser pulse, commonly referred to as a pulse chirp. This effect is generally more significant for shorter pulses (<100 fs). The broadening introduced by the positive dispersion can be reversed by introducing negative dispersion in the cavity, and this accomplished through the use of prisms.

A prism compressor made up of two prisms is depicted in Figure 3.6. Compressors can consist of up to six prisms, and the compressor used in the Ti:S laser is made up of four Figure 3.5. Light entering the first prism is dispersed at different angles and the second prism is placed so that the longer wavelengths have to travel a further distance.<sup>4</sup> By varying the amount of material the light travels through in the second prism, a negative dispersion can be

introduced such that when the light leaves the compressor, each frequency is overlapped in time, resulting in a pulse that is shorter than when it entered. Practically, when the

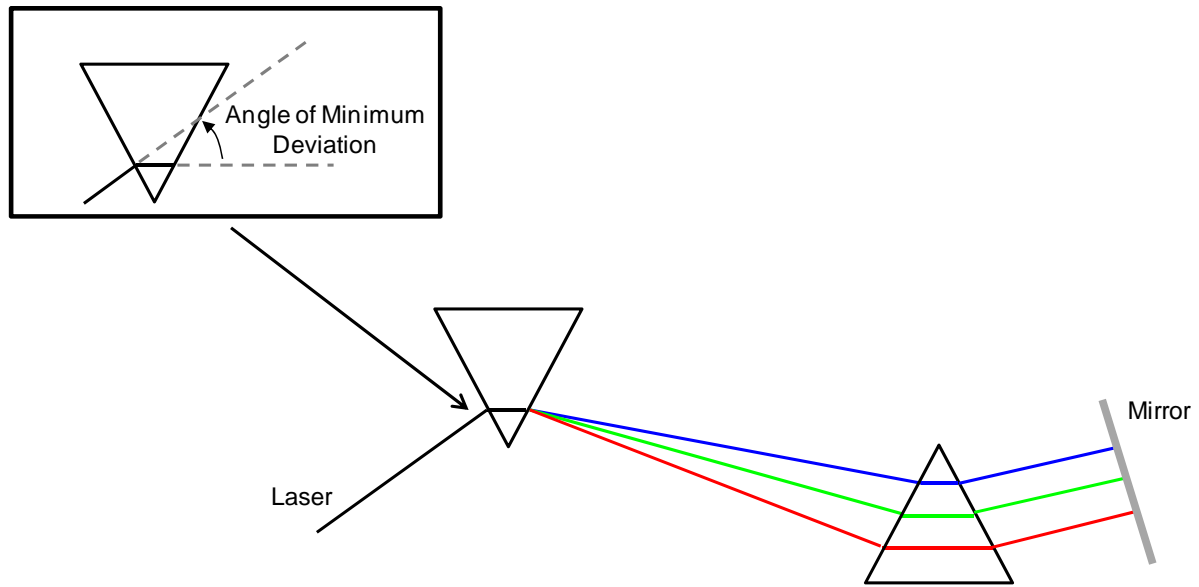


**Figure 3.6:** Prism pair compressor, operated in a double pass configuration. The prisms are placed such that the longer wavelengths of light have to travel a further distance which compensates for pulse dispersion. The inset shows the placement of the prism must be placed at the angle of minimum deviation between the incident and refracted beams, to ensure the light is entering at Bragg's angle.

compressor is being built, the prism angle is chosen such that the angle of the refracted and incident beams are minimized, this is called the angle of minimum deviation (Inset in Figure 3.6). At this angle the incident beam is entering at Brewster's angle, thereby minimizing reflection and maximizing transmission of the beam. Once the pulse has exited the prism compressor in the laser cavity, it is partially transmitted through the output coupler, and represents the laser output.

### 3.2.5 The Faraday Rotator

If all the optics used to send the beam to the microscope are perfectly aligned, then the forward and reverse direction of the optical path will be the same. This can become

problematic, because the reflected beam interferes with the frequency oscillations in the laser cavity and causes it to fall out of mode-locking. To prevent this from occurring, a Faraday rotator is placed directly after the laser output. Traditional Faraday rotators are magneto-optic devices that rotate the polarization of light by  $45^\circ$ , due to the interaction of light with the magnetic field.<sup>4, 5</sup> This occurs because one of the polarization components of the light is resonant with the magnetic field, causing it to have a higher phase velocity. For example, incident light that is vertically polarized is rotated by  $45^\circ$ ; on the return pass, the polarization is rotated by an additional  $45^\circ$  and is now polarized orthogonal (horizontal) to the incident light. If a polarization beam-splitter cube is placed in front of the isolator input, at an angle that transmits vertically polarized light, then the incident light will be transmitted but the reflected beam will be rejected.

The degree that the polarization is rotated by is sensitive to wavelength, and the spectral range of most isolators is therefore generally narrow. This can make application across different experiments complicated. To circumvent this limitation, we utilize a broadband Faraday rotator (EOT BB-8-05-I-090) that is compatible with the Ti:S laser's tuning range. The function is similar to the description above, except following the initial  $45^\circ$  rotation, a quartz reciprocal rotator rotates the beam polarization by an additional  $45^\circ$ . In the forward direction, the rotations are additive, so that light exiting the rotator is orthogonal to the input beam. In the reverse direction, the rotations are opposite to each other, resulting in no rotation of the polarization. Polarization beamsplitter cubes at orthogonal angles are placed on either side of the Faraday rotator, so that reflected light is rejected by the cube at the rotator input (identical to the description above). Practically, alignment of the isolator is

best achieved by first setting two mirrors to define a straight line. The isolator is then placed in the beam path and adjusted till the power coming from the output is maximized.

### *3.2.6 Pulse Compression Outside the Laser*

As the light pulse travels through air and various lenses and optics, it begins to broaden. This is exacerbated as it travels through and is focused by the objective. To correct for the dispersion at the focal point of the objective, a prism compressor (shown in Figure 3.6) is placed directly after the laser. We monitor the pulse width at the objective focal point by simply monitoring the SHG intensity through a lithium niobate crystal. The SHG efficiency is going to be greatest when the pulse width is shortest. The distance between the prisms and the amount of material that the light travels through in the second prism, is varied until the SHG intensity reaches a maximum. In this way the pulse-width at the focal point of the objective can be optimized without having to monitor the autocorrelation.

### *3.2.7 The Variable Attenuator*

Following the prism compressor, the beam is sent through a variable attenuator which serves as a method for controlling the average power to the microscope. The variable attenuator is made up of a half wave plate and polarizing beam-splitter cube. The half wave plate is essentially a birefringent crystal that has been cut such that the extraordinary axis (optic axis) is parallel to the surface. As light travels through the crystal, the polarization component that is along the extraordinary axis moves faster than light polarized along the ordinary axis. The result is a shift in the phase of the polarization components. A half wave plate retards one component  $180^\circ$  relative to the other and results in a beam that is orthogonally polarized.<sup>5</sup> Adjusting the angle of the wave plate therefore changes the polarization state, between vertical and horizontal. The amount of power reaching the



microscope can then be varied by placing a polarizing beam-splitter cube directly after the wave plate.

### *3.2.8 Beam Expansion*

Following transmission through the polarization cube, the light is sent through a beam expansion setup to increase the diameter of the laser spot. The purpose of doing this is to overfill the input aperture of the objective (discussed in further detail in the paragraph below describing the objective lens). The beam expander consists of two plano-convex lenses (50 and 200 mm focal lengths) that are placed at a distance from each other that equals the sum of their focal lengths. The magnitude of the expansion is equal to the ratio of the lens focal lengths.<sup>6</sup> For example, lenses with 50 mm and 200 mm focal lengths will yield a 4x increase in the width of the beam. The lens with the shorter focal length is placed preceding the other lens. In practice, the two are placed at the precise distance from each other where the light exiting the second lens is collimated (i.e. the light rays are parallel to each other). This condition is important, because any convergence or divergence in the light rays, no matter how subtle, will drastically change the focusing properties of the objective, and results in an overall reduction of the microscope resolution.

The alignment procedure consists of placing the lenses in a beam that is travelling along a straight line. The lenses are aligned by monitoring the transmission angle on a nearby aperture (such as an iris) and the reflection angle on an aperture preceding the lens (in the case of the second lens, this can be accomplished by roughly centering the reflection on the rear of the preceding lens). The lenses are properly aligned when the reflected and transmitted beams are exactly parallel with the laser propagation direction ( $0^\circ$ ). The degree to which the light is collimated exiting the second lens can be tested by placing a mirror directly

after the second lens and shunting the beam over a long distance. When the width of the spot exiting the beam expander matches the spot size over a long distance, the beam is collimated. Following the beam expander, the light is reflected off a dichroic beam splitter (Semrock FF01-370/36-25) and sent into the input aperture of the objective.

### 3.2.9 The Objective

The objective used in our experiments is an Olympus MSPlan 50. It was designed to be used without a coverslip and has a magnification of 50x. The objective is a series of lenses in close spatial proximity that focus the incoming beam to a diffraction limited spot; the diameter of which can be determined using Equation (2) and (3) for one and two-photon microscopy, respectively. Each of those equations is in part, a function of the numerical aperture (NA) of the objective which is defined as being a product of the refractive index ( $n$ ) between the objective and the sample, and the acceptance angle of light ( $\theta$ ):<sup>7</sup>

$$NA = n(\sin \theta) \quad (27)$$

Often, the NA can be increased by placing a medium such as oil or water, that has a higher index of refraction than air ( $n = 1$ ), between the sample and objective (thus necessitating a coverslip). We utilized a dry, air objective with a numerical aperture of 0.8.

#### 3.2.9.1 Working Distance and Depth of Field

In addition to the NA, other important specifications of the objective are the depth of field and the working distance. The depth of field is defined as the distance the objective can travel without losing resolution. With two-photon microscopy this is analogous to the height of the focal volume along the z-axis (Equation 5).<sup>8</sup> This value varies with the NA of the objective. For larger NAs the convergence angle of light is larger, resulting in a smaller spot size, but also a shallower depth of field.<sup>7</sup> The objective working distance is the distance

between the sample surface and the objective.<sup>7</sup> This follows the same inverse relationship with NA. With the objective used in our experiments, the working distance is approximately 500  $\mu\text{m}$ .

### 3.2.9.2 Beam Truncation

To ensure the spot size is diffraction limited at the focal point, the input aperture of the objective must be uniformly illuminated and overfilled, truncating the light. When the objective is overfilled, the beam profile at the focal point adopts an Airy disc pattern.<sup>7</sup> According to Equation 2, the diameter of the spot is measured from the first trough in the pattern. If the input aperture is not overfilled, the beam profile adopts a Gaussian shape and the intensity of the spot never falls to zero.<sup>9</sup> In this case it becomes necessary to redefine the resolution in terms of some other point of reference. This is commonly chosen as either the full-width at half-maximum (FWHM), which represents the width at the 50% intensity point, or the  $1/e^2$  point, which is the 13.5% intensity point.

The constant 2.44 in Equation 2, is derived under the assumption that the beam profile at the objective focal point adopts an Airy disc pattern. Since this is no longer valid in the absence of truncation, we replace the constant with a variable ( $K$ ) that depends on the truncation ratio, so that:<sup>6,9</sup>

$$D = K \frac{\lambda}{2NA} \quad (28)$$

The value of  $K$  at either the FWHM or  $1/e^2$  points can be evaluated using:

$$K_{FWHM} = 1.029 + \frac{0.7125}{(T - 0.2161)^{2.179}} - \frac{0.6445}{(T - 0.2161)^{2.221}} \quad (29)$$

$$K_{1/e^2} = 1.6449 + \frac{0.6460}{(T - 0.2816)^{1.821}} - \frac{0.5320}{(T - 0.2816)^{1.891}} \quad (30)$$

where  $T$  is the ratio of the Gaussian beam diameter at  $1/e^2$  ( $D_b$ ) entering the objective and the diameter of the input aperture of the objective ( $D_t$ ), also called the truncation ratio:

$$T = \frac{D_b}{D_t} \quad (31)$$

It follows then, that when  $T \geq 2$ , the objective aperture is overfilled and uniformly illuminated, and the beam profile takes on the familiar Airy disc pattern. When  $T = 1$ , the beam is truncated at the 13.5% intensity point and has both Airy disc and Gaussian character at the focal point. At  $T = 0.5$ , the spot intensity has a Gaussian profile.

It is necessary to find a balance between the loss of power due to truncation and the spot size. The power loss at the focal point can be calculated using:<sup>6,9</sup>

$$P_L = e^{-2(D_t/D_b)^2} \quad (32)$$

When  $T = 2$ , the power loss is ~60%. However, when  $T = 1$ , the power loss is only 13.5%, and the spot diameter is only about 8% larger than  $T = 2$ . It can therefore often be advantageous to use a truncation ration between 0.7 and 1.0. Doing so ensures both a minimum loss in power and overall resolution, due to spot size.

#### 3.2.9.3 Objective Alignment Procedure

The objective alignment is perhaps the most critical in the setup of the microscope. This was accomplished by using a Helium:Neon (HeNe) laser to define a line collinear with the excitation beam, but propagating in the reverse direction. The objective is then placed in the beam paths and each aperture aligned to the respective incident beam. We utilized a 6-axis kinematic mount that enable lateral translation along the x and y-axes as well as pitch and yaw control. Once the beams are centered on their respective apertures the objective is

parallel to the collinear beams and straight. Any deviation from this will cause the beam to focus at an angle and create a mismatch between the brightfield and fluorescence images.

### 3.2.10 Empirical Determination of Microscope Resolution

We initially tested the resolution of the objective using a one-photon excitation from a 532 nm frequency doubled Nd:YVO<sub>4</sub> laser. We developed an algorithm for estimating the resolution by scanning a single 2  $\mu$ m fluorescent bead with a 250 nm step size. The intensity profile along the diameter of the bead can be thought of as a convolution of the Gaussian intensity profile of the focused laser spot ( $I_L$ ), and the object shape. In the limit of an infinitely narrow spot, the fluorescence intensity of the bead ( $f(x)$ ) should follow a semi-circular distribution. The convolution integral could then be described by:

$$I_F(\lambda) = \int I_L(x, \lambda) \cdot f(x) dx \quad (33)$$

where  $I_L$  follows a Gaussian distribution:

$$I_L(x, \lambda) = \frac{1}{c\sqrt{2\pi}} \cdot e^{\frac{-(x-\lambda)^2}{2c^2}} \quad (34)$$

and  $f(x)$  is semi-circular function:

$$f(x) = r \cos\left(\sin^{-1}\left(\frac{(r-x)}{r}\right)\right) \quad (35)$$

The result of the convolution integral is superimposed onto the intensity profile of the bead, obtained experimentally (Figure 3.7). The full width at half maximum ( $c(2\sqrt{2\ln(2)})$ ) of  $I_L$  is then varied till a good fit of the data is obtained. The result represents the width of the beam at the focal point of the objective. This was repeated with seven beads and yielded a beam diameter of  $\sim 1.3 \mu$ m. Using Equation (2) to calculate the theoretical resolution at 532 nm yields a spot size of 810 nm.

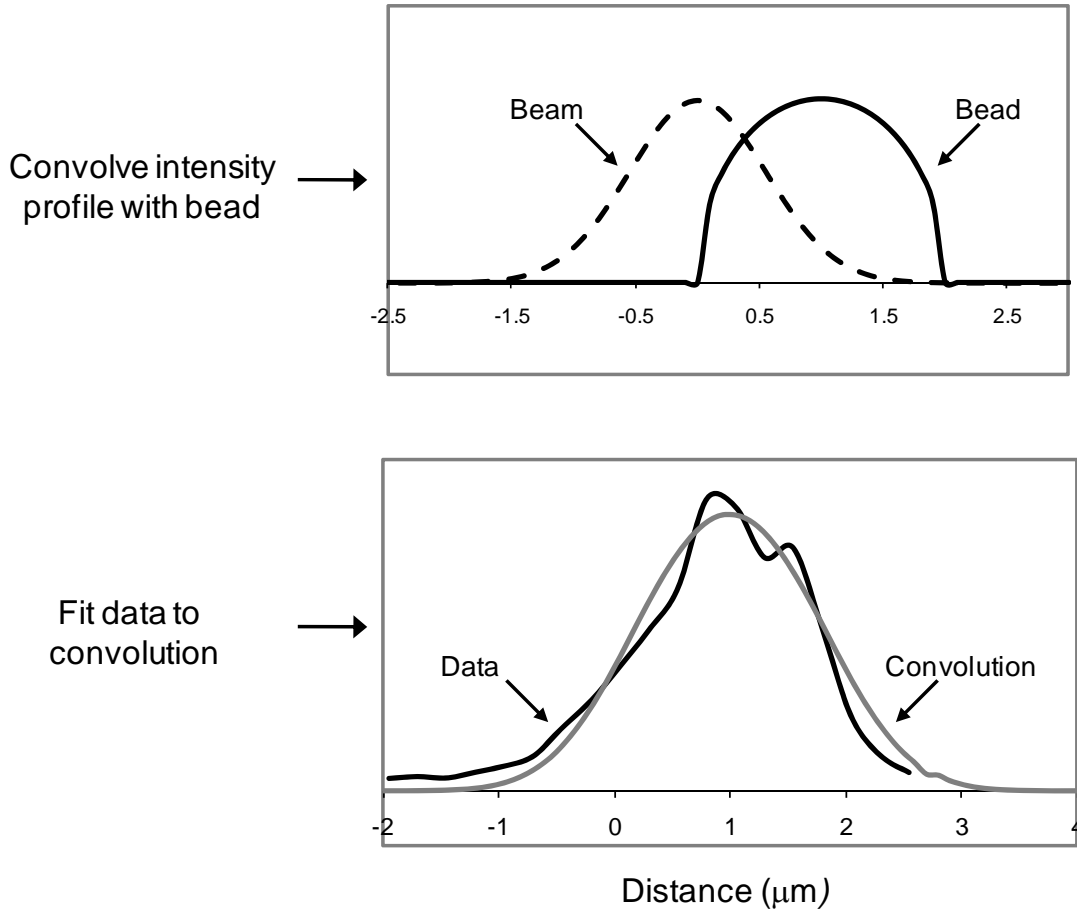


**Figure 3.7:** Algorithm for determining the width of the beam at the focal point of the objective using  $2\ \mu\text{m}$   $\varnothing$  Nile Red beads. Given the  $\text{IPSF}^2$  has a Gaussian profile and the intensity of the bead has a semi-circular profile, the two functions can be convoluted to yield our theoretical resolution. The data is fit to the convolution and the resulting FWHM is directly correlated to the width of the beam.

The theoretical resolution of using a two-photon excitation was found to be  $\sim 350\ \text{nm}$  using Equation (3). This was confirmed empirically by scanning  $100\ \text{nm}$  fluorescent beads and measuring the FWHM of the resulting intensity profile. Since the object size is below the diffraction limit of light, the image represents the size of our laser spot which has a diameter of  $\sim 450\ \text{nm}$ .

### *3.2.11 Brightfield imaging*

Brightfield imaging is a method in which the entire field of view is illuminated, using in our case, a halogen light source, coupled into a fiber optic cable. The purpose can take many forms, but in our experiments, the brightfield was used solely to scan the entire field of view and locate samples of interest for fluorescent second-harmonic studies. As such, the illumination setup is simple and achieves the desired result well. Light generated by the halogen light source is collected with a lens and directed onto the sample using two mirrors. However, the brightfield detection setup is less trivial and is detailed below. A general optical layout is also shown in Figure 3.8.

#### *3.2.11.1 The Tube Lens*

Our objective lens is infinity corrected; meaning light collected through the objective is collimated. An image is formed by placing a lens in the optical path, commonly called a tube lens. The standard tube lens focal length used with Olympus infinity corrected objectives is 180 mm ([www.olympusmicro.com](http://www.olympusmicro.com)). The magnification of the objective can be calculated by dividing the focal lengths of the tube lens and objective.<sup>7</sup> Given the objective magnification and tube lens focal length (fl), our objective is calculated have a 3.6 mm fl.

The position of the tube lens relative to the objective is critical. While it was not a major concern in our setup, if the tube lens is placed too close to the objective, then there is little room to place any desired optics. More importantly, if the lens is placed too far from the objective then there is a loss in overall collection efficiency because the peripheral light waves from the sample are no longer incident on the lens. However, in our experiments the ZnO rods are small relative to the entire field of view. If the object of interest is placed in the center of the field of view then the light rays emanating from it follow a nearly linear path

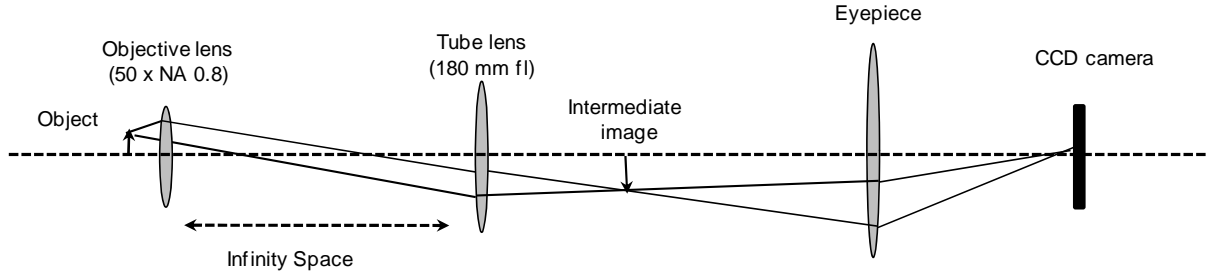


**Figure 3.8:** Optical layout for brightfield and CCD imaging. The area between the objective and tube lens represents infinity space where the light rays are parallel to each other. Light is focused into the CCD camera with a lens commonly referred to as the eyepiece. In our setup this is a simple plano-convex lens. Adapted from Reference #7.

(analogous the bottom of the arrow in Figure 3.8). The light rays emanating from the surrounding area travel at the peripheral angle (analogous to the top of the arrow in Figure 3.8), but since they do not contain the object of interest, collecting their light rays is of little consequence, and the distance between the tube lens and objective becomes less critical in our experiments. In addition to objective magnification, further magnification can be achieved by placing a lens (referred to as the eyepiece) between the tube lens and detector (which in our setup, is a CCD camera).

### 3.2.11.2 Image Magnification

In some experiments the CCD camera can be for two-photon emission or back-scattered SHG imaging. In these experiments it can be useful to vary the image magnification. This is accomplished by varying both the distance between the eyepiece and tube lens, and between the eyepiece and CCD camera. Magnification ( $M$ ) is simply the ratio of the image distance ( $s''$ ) to object distance ( $s$ ) (Figure 3.9):<sup>10</sup>

$$M = \frac{s''}{s} \quad (36)$$



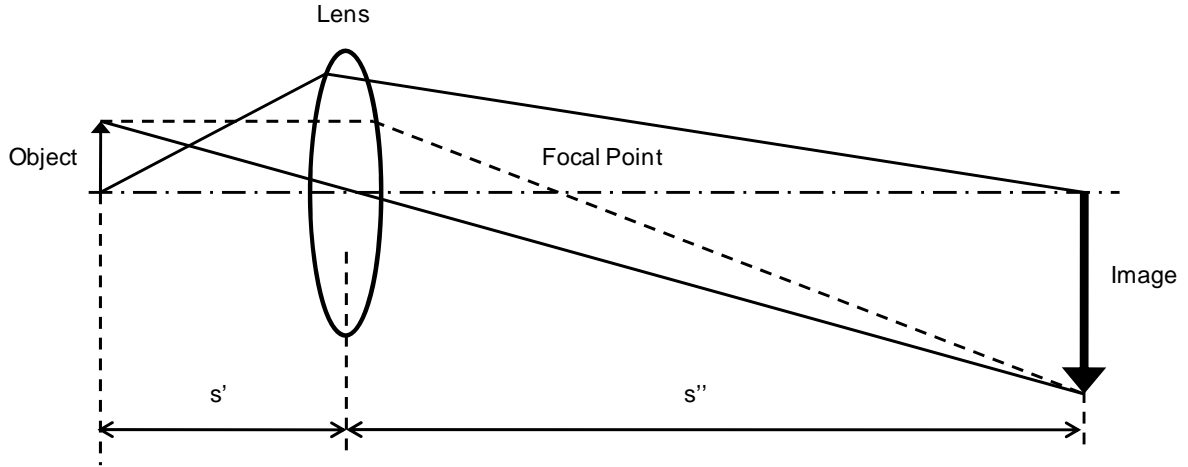


**Figure 3.9:** Lens magnification, which can be described as the ratio between the image distance ( $s''$ ) and the object distance ( $s$ ).

Since the objective and tube lens collectively determine the objective magnification, in our setup the distance from the tube lens focal point to the eyepiece is treated as the object distance ( $s$ ). Here, the divergence of the light from the eyepiece determines the magnification, and is controlled by changing the object distance. Doing so changes the distance between the image plane and eyepiece, and the CCD camera must be moved to compensate (Figure 3.10). The movement of the CCD camera could be prevented, but this would require the introduction of more lenses. Since the image brightness decreases with increasing magnification, the addition of more optics could exacerbate the loss in intensity. Also, practically, the camera could more simply be placed on a rail to ensure that movement along the optical axis could occur accurately.

Given the desired magnification and the focal length of the eyepiece, the object distance can be solved using the following equations. The focal length ( $f$ ) is related to the object and image distance by:<sup>10</sup>

$$\frac{1}{f} = \frac{1}{s} + \frac{1}{s''} \quad (37)$$

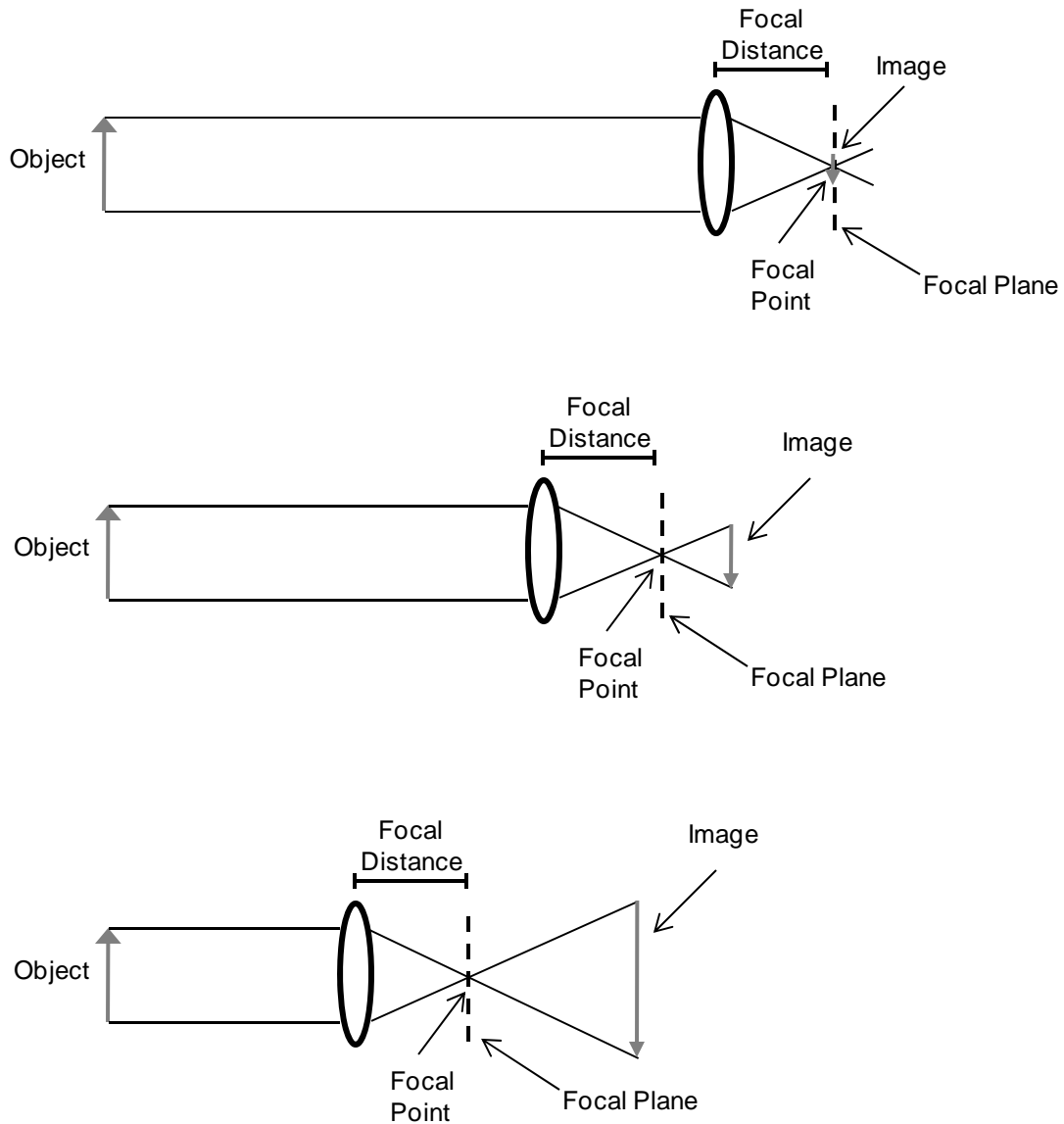


**Figure 3.10:** The distance between the lens and the image plane changes as the object gets closer to the lens. In our setup, this requires that the CCD camera be moved to account for the change.

Using Equation (33), the formula can be rearranged to show the relation to magnification:

$$f = \frac{sM}{M+1} \quad (38)$$

Solving for  $s$  yields:

$$s = f \left( 1 + \frac{1}{M} \right) \quad (39)$$

Once Equation (39) has been solved, Equation (36) can be used to solve for the image distance ( $s''$ ). The overall image magnification is then the product of the magnification of the objective and eyepiece. In this way, the overall magnification and relative distances between the lenses and detector that make-up the brightfield imaging system can be solved.

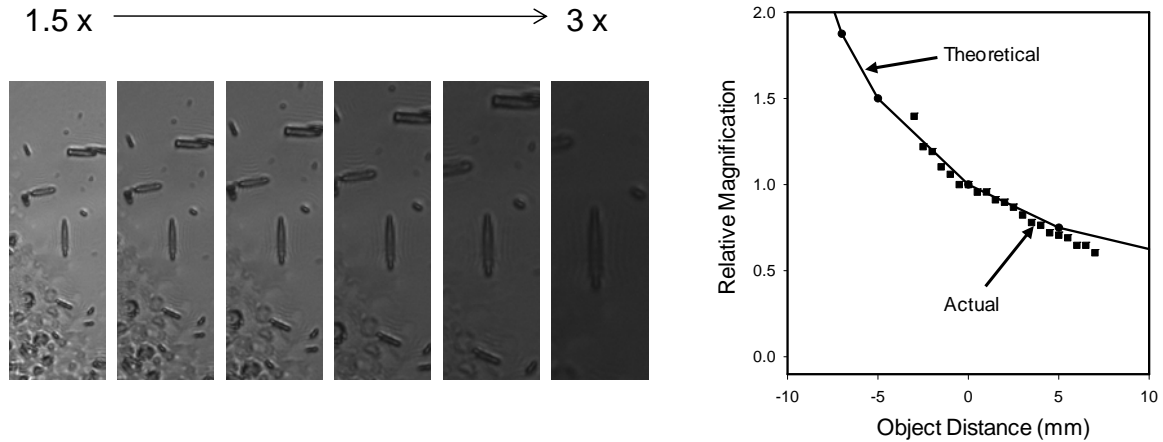


**Figure 3.11:** (*left*) Brightfield images of a single structure collected with increasing magnification. The reduction in intensity is due to the increasingly divergent light and indicates the inverse relation between S/N ratio and magnification. The graph on the right is a comparison of the relative magnification as a function of actual (squares) and theoretical object distances (connected circles).

Using the equation above, we calculated the theoretical magnification for a series of object distances ( $s$ ) and compared them to our empirical observations. The results, shown in Figure 3.11 are in agreement with each other. The CCD images collected at a series of

magnifications are shown below the graph. The decreasing image intensity with increasing magnification is due to the divergence of light from the eyepiece, and indicates the inverse relationship between image magnification and intensity.

### *3.2.12 Fluorescence detection*

Following sample excitation, light is collected back through the objective and transmitted through the dichroic beamsplitter. A mirror placed on a flip-mount is used to direct the light through a monochromator for detection with a photomultiplier tube (PMT). Detection of back-scattered SHG occurs in an identical path, with the only difference being the grating angle of the monochromator. For forward-scattered SHG, a condenser lens is placed above the sample to collect the generated light, and is directed to a PMT mounted above the objective (here filters are used in place of a monochromator).

#### *3.2.12.1 The Monochromator*

The monochromator used in our experiments follows a Czerny-Turner design, the layout of which is shown in Figure 3.12. The monochromator consists of two curved mirrors, a diffraction grating and an input and output aperture with controllable slit sizes. Light focused through the entrance slit is collimated by the first mirror and directed onto the diffraction grating.<sup>11</sup> The grating has a highly reflective surface that has lined grooves that resemble a saw-tooth pattern. Different wavelengths of light diffract off the grating at specific angles and are directed to the second mirror.<sup>6, 11</sup> Since the different wavelengths of light incident on the second mirror are propagating at different angles, they are focused at different positions in the monochromator. The angle of the grating can be adjusted to permit a certain wavelength of light to exit the monochromator through the output slit. Other light rays will be focused at different angles and rejected.

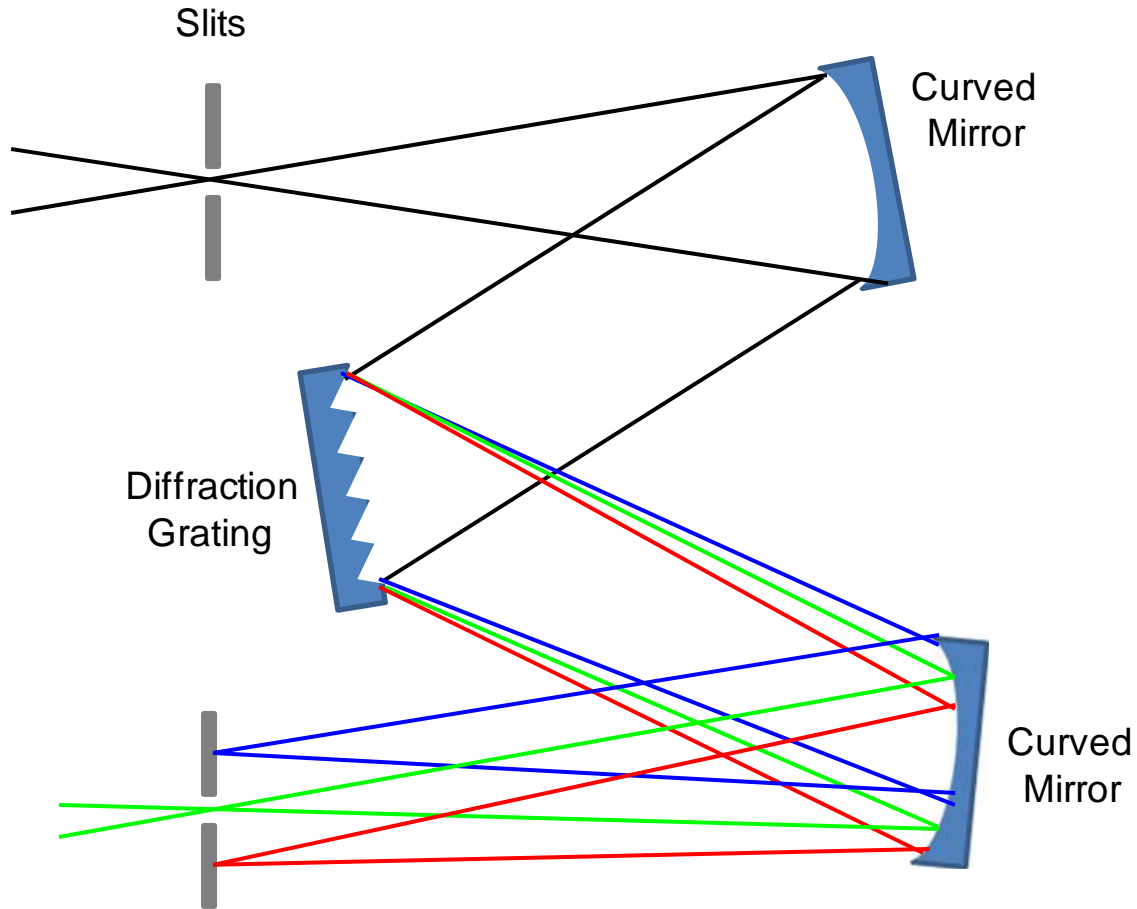


**Figure 3.12:** Czerny-Turner monochromator. Light entering the monochromator is collimated by the first mirror and directed to the diffraction grating. Each frequency of light is diffracted off the grating at different angles and focused by the second mirror. The angle of this mirror determines which frequencies of light will be permitted through the exit slit. The monochromator in our setup follows a similar design except that the slits are on opposing faces of the monochromator.

The spectral sensitivity of the monochromator is ultimately determined by the slit width at the input and output apertures and the dispersive characteristics of the grating. Given the dispersion ( $D'$ ) of the grating (its ability to separate each wavelength) and the width of the slit ( $S$ ), the allowable bandwidth ( $BW$ ) can be calculated using:<sup>6, 11</sup>

$$BW = S \times D' \quad (40)$$

Therefore, as the slit size is decreased the overall spectral resolution increases. However, reduction in slit width also decreases the light intensity entering the monochromator, thereby

decreasing the S/N ratio. A balance must therefore be found between spectral resolution and increased noise.

The monochromator's ability to disperse light is a function of how many grooves exist per millimeter on the grating; the greater the number of grooves/mm (g/mm) the greater the dispersion, which increases the overall monochromator resolution.<sup>4</sup> For example, the monochromator used in our setup (Digikrom CM110) has a grating with 1200 g/mm, and the dispersion is 7 nm/mm. The same monochromator with 2400 g/mm has a 3.5 nm/mm dispersion. When light is reflected off the grating it is diffracted in different directions, each of which is assigned an order. For example, 300 nm light may result from a first-order diffraction. A second order diffraction at exactly the same angle could occur for 150 nm light.<sup>4, 6</sup> This can sometimes cause problems with data collection, and care should be taken to use filters to eliminate light from higher order diffraction. Gratings can be tuned to efficiently select for first-order diffractions, but will be more efficient at certain wavelengths. The spectral efficiency curves can be tuned by changing the facet angles of the grooves on the grating. This process is called blazing, and the blaze wavelength is where the grating is maximally efficient.

Equally important to the grating efficiency is to ensure that the lens used to focus the light into the input slit, matches the F-number (F/#) of the monochromator. The F/# is a measure of a system's ability to collect light and is approximately equal to the focal length divided by the clear aperture. The amount of light collected by the system, or radiant flux ( $\phi_c$ ), increases with the inverse square of the F/#:<sup>4</sup>

$$\phi_c \propto \frac{1}{(F/\#)^2} \quad (41)$$

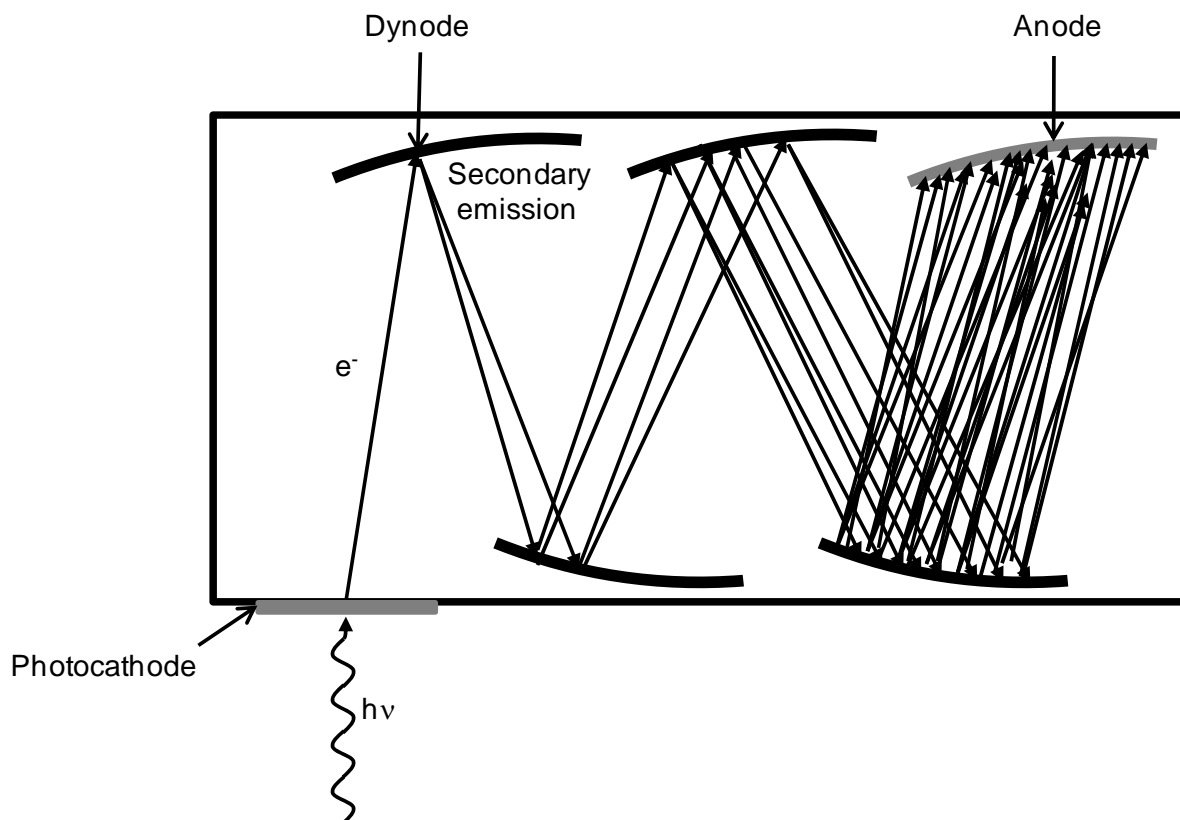


**Figure 3.13:** Schematic depiction of a photomultiplier tube (PMT). If light incident on the photocathode is greater than its work function, then an electron will be released and accelerated towards a dynode. Each dynode is held at successively greater potentials so that as electrons accelerate and reflect off them, they release another electron. The result is a rapid amplification of the signal into a readily detectable current.

Therefore, as the  $F/\#$  decreases,  $\phi_c$  increases. In the case of a monochromator, the  $F/\#$  is determined by the dimensions and relative positions of the internal components. If the  $F/\#$  of the lens ( $F/\#_l$ ) used to focus light in to the input slit equals the monochromator  $F/\#$  ( $F/\#_m$ ), then the grating will be optimally illuminated and efficient. If  $F/\#_l < F/\#_m$  then the grating is overfilled and overall intensity is reduced. In the opposite scenario, all the light is incident on the grating but will not be focused through the input slit, thus leading to a decrease in overall intensity.<sup>4</sup> The monochromator used in our setup has a 110 mm focal length and the  $F/\# = 3.3$ . Light exiting the monochromator is then detected using a photomultiplier tube.

### *3.2.12.2 The Photomultiplier Tube*

A photomultiplier tube (PMT) is a method of amplification that can convert a single electron into a readily detectable signal (Figure 3.13).<sup>4, 11</sup> It is composed of a photocathode, a series of dynodes and an anode. The process of amplification is initiated when a photon exiting the monochromator contacts the photocathode. If the photon energy is greater than the photocathode work function, then an electron will be released and directed towards the first dynode. Each dynode is held at successively larger positive potentials, accelerating the electrons as they approach. As each electron contacts the dynode it results in the release of another in a process called secondary emission.<sup>4</sup> The doubling effect at each dynode leads to a rapid amplification of electrons (generating  $\sim 10^5$  to  $10^7$  electrons/photon) that are directed towards the anode, giving rise to a readily detectable current.

Our experiments were conducted in a single photon counting regime. This condition is generally satisfied when one photon is generated every 1000 pulses. This can be calculated by monitoring the count rate relative to the laser repetition rate and determining how many counts (1 count = 1 photon) are being generated per laser pulse. Since there is no way of knowing how many photons contact the photocathode at any one time, if the experiment deviates from this regime then there is a risk of reducing the PMT sensitivity, and garnering inaccurate results.

### *3.2.13 Data Acquisition*

The analog signal generated by the PMT is amplified and sent to a discriminator. The discriminator filters out any signal that falls below a threshold voltage and converts “real” pulses into digital 5V TTL pulses which can be detected by a counter on a data acquisition (DAQ) card (Model PCI 6602, National Instruments). This process occurs till the scanning



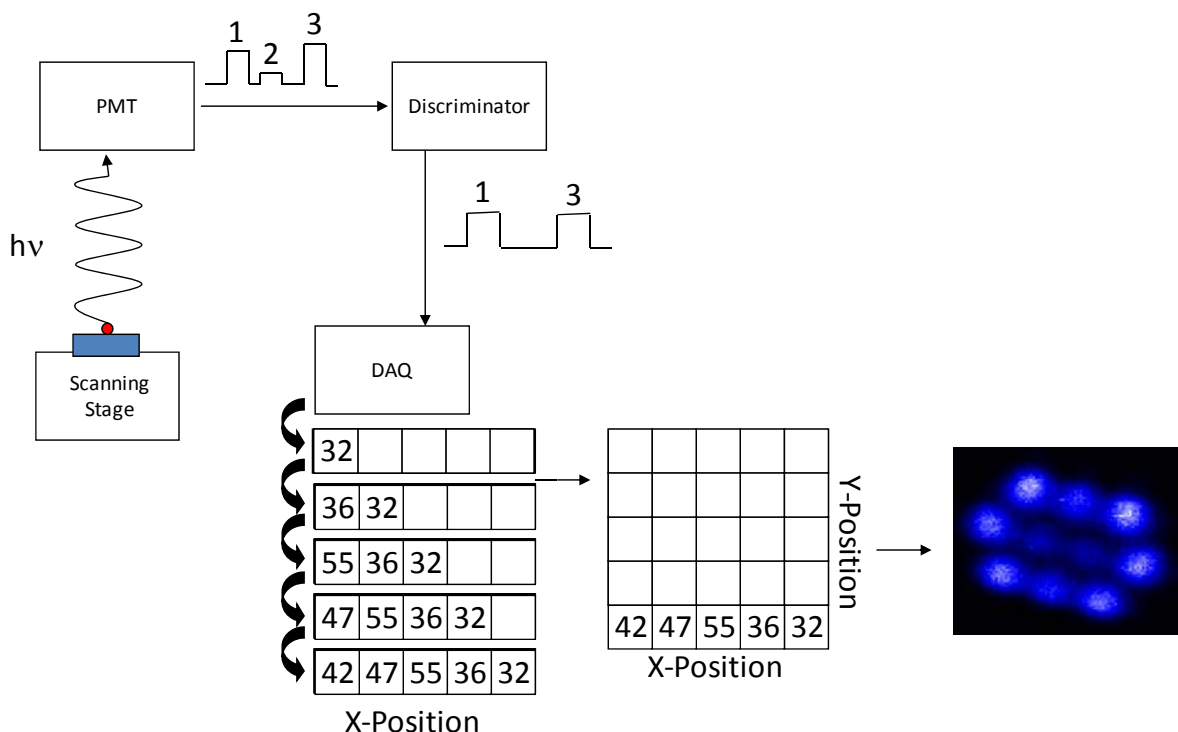


**Figure 3.14:** Data acquisition process. Light detected by the PMT is sent to a discriminator that filters noise and outputs 5 V TTL pulses. Each pulse is counted by a data acquisition card. Since each pulse is from one photon, higher counts correspond to higher intensity emission. This process continues along every step in the x-direction. Once the stage has reached the end of a line, the data is placed into a two-dimensional array, and the process is repeated for the next line. The resulting two-dimensional array represents the image intensity profile.

stage has dwelled at one sample coordinate for a user defined period, the stage proceeds to the next coordinate and the cycle is repeated until the entire line ( $x_0$  to  $x_{\max}$ ) has been scanned. At the end of each line scan the total number of counts per bin are accessed and recorded in the software as a one dimensional array which is displayed as a graph of number of counts versus position (analogous to fluorescence intensity vs. position). A two dimensional array is generated by the software incorporating each successive one dimensional array as it is received, eventually generating a two dimensional image of the sample. The relative intensity is depicted by assigning a different shade of color relative to

the number of counts per bin; generally a darker shade indicates areas of low fluorescence and a lighter shade, areas of high intensity. The two-dimensional array is also saved as a text file and accessed for further image processing using Matlab. The process is depicted in Figure 3.14.

Similarly, steady state emission spectra can be collected by scanning the monochromator grating and dwelling at each wavelength for a defined period of time. The data is stored as a one dimensional array and processed using a program designed in Matlab.

In addition to the monochromator/PMT detection described above, instrumentation for conducting time-correlated single-photon counting experiments was also incorporated with the microscope. This was accomplished by placing a mirror in the optical path that directed the emission to a different monochromator/PMT. While this experiment was conducted extensively in the work described in this dissertation, an excellent review of the instrumentation used and the science behind the technique can be found in a previous graduate student's (Dr. Kyle Brennaman) dissertation.<sup>12</sup>

### **3.3 ZnO Synthesis**

There are many different methods for synthesizing ZnO nanostructures. Of these, perhaps the two most often used are hydrothermal and chemical vapor deposition methods.<sup>13</sup> We have implemented these and also solution phase methods to develop a synthetic protocol that yields consistent results. Our laboratory is interested in synthesizing a multitude of shapes and sizes, to compare the photophysical properties between these structures, but to also analyze the differences within a single structure. Our methods and results are detailed below.

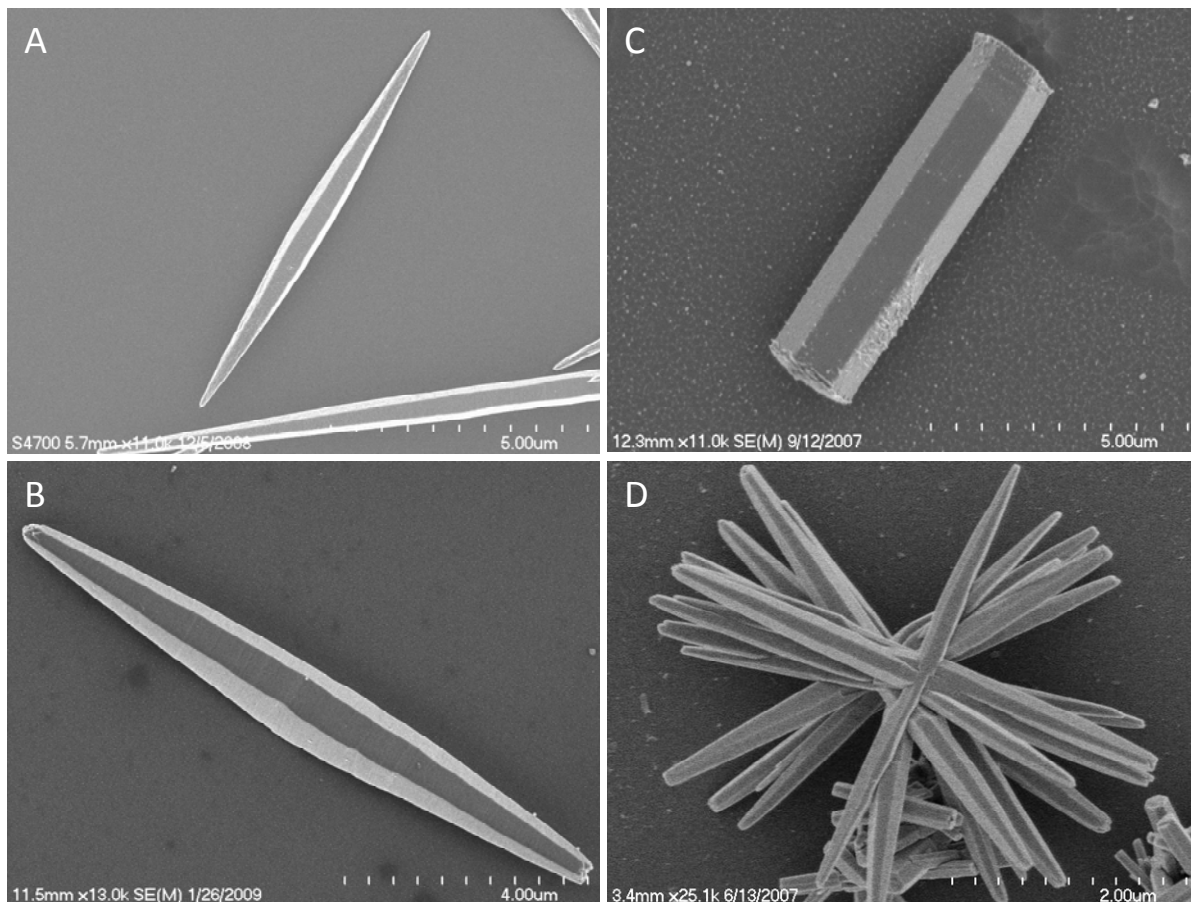


**Figure 3.15:** Typical structures obtained using hydrothermal synthetic methods. The experiments described herein were conducted on structures like those shown in (A) and (B). The needle-shaped rods have a hexagonal cross-section and range between 5 and 20  $\mu\text{m}$ . We have also obtained similar rods with flat ends (C) and flower-like structures (D) with this method.

### 3.3.1 Hydrothermal Synthesis

Of the methods used, hydrothermal synthesis has resulted in the most consistent results and represents the majority of our synthetic efforts. A precondition to probing different areas of a single nanostructure is that the size of the structure must be greater than the diameter of the laser spot at the focal point of the objective (empirically determined to be  $\sim 450$  nm with our setup). We therefore had to tailor our methods to synthesize structures with length scales in excess of a micron. Furthermore, to address the effects of nanostructure

morphology on carrier dynamics we explored several different synthetic methods. To date we have focused on hydrothermal and solution phase techniques; specifically, we have adapted our methods from work published by Cheng et al.<sup>14</sup>, Li et al.<sup>15</sup> and Yu et al.<sup>16</sup>. These methods represented a good starting point because of their relative simplicity, requiring no additives or templates and readily available substrates. We have found that varying temperature, reaction time and/or concentration enables us to synthesize a variety of shapes that range in length from 1 to 20  $\mu\text{m}$  (Figure 3.15).

In their work Cheng et al.<sup>14</sup> reported that nanorod size and density depended on whether the solution was concentrated with Zn salt<sup>14</sup>. Given that Zn salt is soluble in water, a solution concentrated with alcohol leads to Zn saturation. This favors the formation of nuclei, leading to a large number of small rods (scaling in the 10s to 100s of nm). Conversely, when the water concentration is high, nanorod growth is favored, leading to fewer, but larger structures<sup>14</sup>. We therefore increased the water concentration which resulted in the formation of nanorods that ranged from 1 to 5  $\mu\text{m}$  in length.

In their paper, Li et al. reported that formation of ZnO nanorods and flowers occurred over a series of steps which involved either the conglomeration of nuclei into quasi-spherical particles or their dispersion across a glass substrate. The quasi-spherical particles lead to the growth of nanoflowers, while the dispersed nuclei grew into single nanorods<sup>15</sup>. Therefore, modifying their procedure<sup>15</sup> by increasing the reaction temperature (to increase nanorod length), led to the formation of predominantly needle-like nanorods (Figure 3.15 A&B) and the presence of nanoflower-like structures shown in Figure 3.15 D. Changing the Zn salt and increasing the reaction time, led to the formation of nanorods with predominantly flat ends.

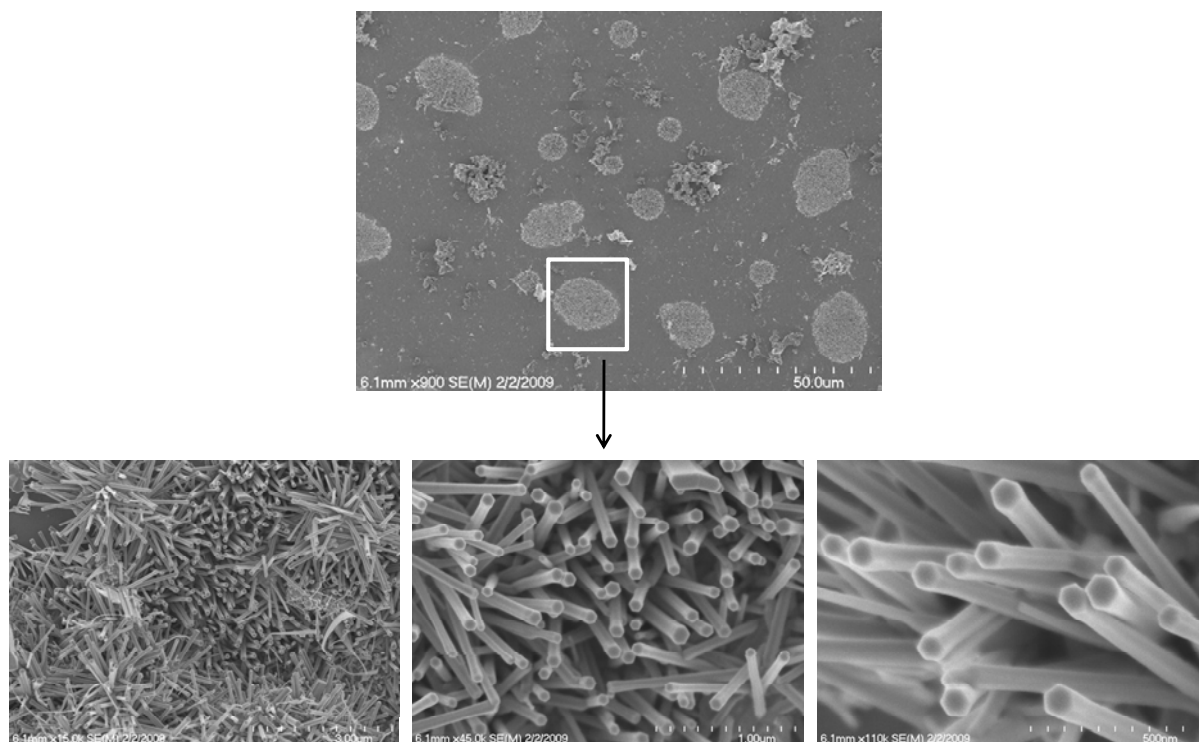


**Figure 3.16:** Nanorod growth using CVD occurs in patches on the substrate surface. This may be due to rough areas that trap nuclei which initiates structure growth.

### 3.3.2 Chemical Vapor Deposition (CVD)

There are two major CVD techniques that depend on either vapor-liquid-solid (VLS) or vapor-solid (VS) growth mechanisms. The fundamental difference between them is that VLS requires a metal catalyst (such as gold nanoparticles) that forms a liquid metal alloy with Zn to initiate nuclei formation and structure growth. In the VS method, Zn is vaporized and simply allowed to react with  $O_2$ . While this growth method is not generally well understood, it has been suggested that ZnO nucleation favors rough surfaces. Data from our syntheses yield results that appear to agree with this mechanism. Images obtained with a scanning electron microscope (SEM) show that growth of nanorods appears to occur in patches (Figure 3.16). However, we have also successfully grown tetrapods with differing end morphologies as well as ribbon structures (Figure 3.17). Analysis of these images with the SEM suggests the structures are growing in the vapor phase and precipitating onto the

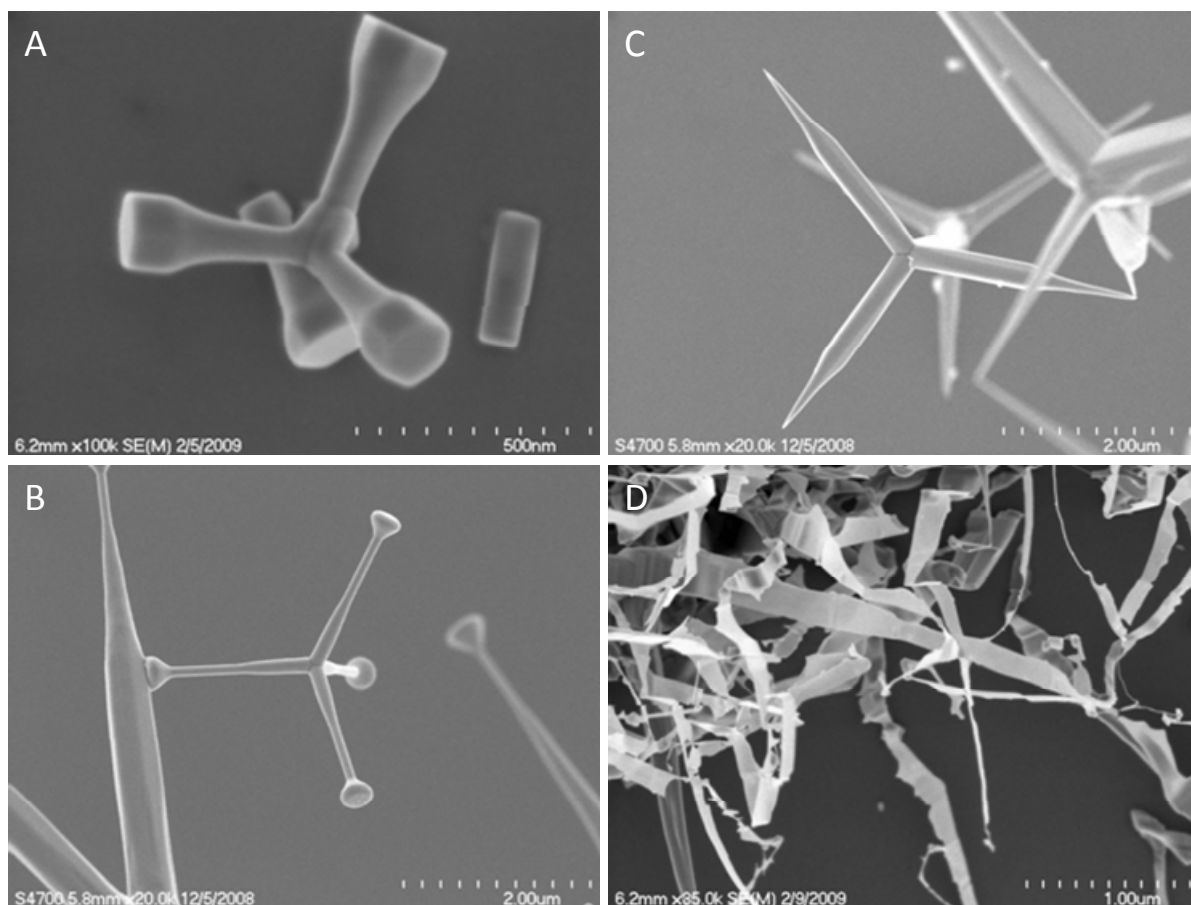


**Figure 3.17:** The images in (A), (B) and (C) are of tetrapods with differing end morphologies grown using CVD. (D) is an example of ribbon structures.

slide. Therefore, it appears nucleation on rough surfaces is not the sole method for structural growth. Of the synthetic methods we utilize, this yields the most inconsistent results. While we have obtained growth in certain patches, what gives rise to them still eludes us. The efforts of our work conducted thus far with this technique have been detailed in a thesis written by Chuan Zhang.<sup>17</sup>

### 3.3.3 Solution phase synthesis

We have obtained interesting results with solution phase synthesis (Figure 3.18). By replicating the conditions published by Yu et al.<sup>16</sup> we were able to synthesize ZnO dumbbell structures (Figure 3.18A), with the same general morphology (twinned structure) in

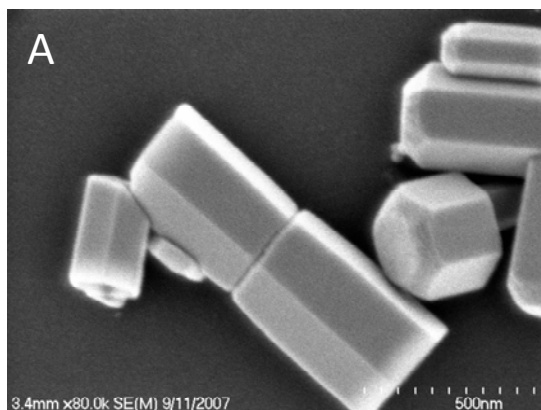
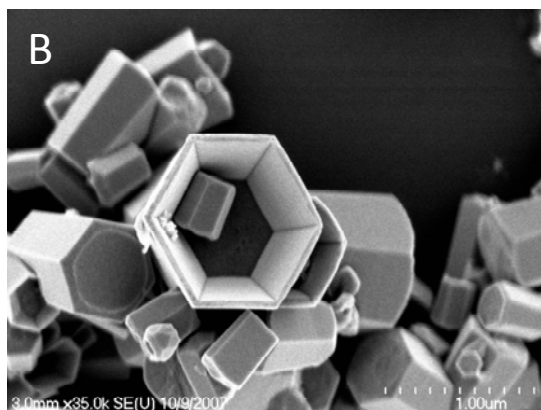


**Figure 3.18:** Results from solution phase synthesis give rise to dumbbell shaped structures, both solid (A) and hollow (B). This same reaction, conducted at a lower temperature, yields the ribbons shown in (C).



their publication (a twinned rod with a grain boundary in the center). Additionally, work published by Tang et al.<sup>18</sup> using a similar method, showed that increasing reactant concentration led to the formation of both solid and hollow nanorods, with hollow rods populating the air-water interface. We therefore increased the concentration of reactants in the dumbbell preparation and obtained a similar result, with a population of both hollow and

solid dumbbell structures (Figure 3.18B). While these results show promise, the variation in the dumbbell sample was great and made finding consistent structures to study difficult. We found that decreasing the temperature of the reaction led to the formation of ribbon-like structures (Figure 3.18C). Initial photophysical measurements conducted on the ribbons with the microscope showed some potentially promising data, but the damage threshold of the structures was low making data collection difficult. Further experiments will be required to probe their characteristics.

The structures that have been imaged and studied spectroscopically in this dissertation are the ZnO needle-like rods grown using hydrothermal methods. These rods show interesting spectral properties and are photochemically robust. What follows are the results of a series of spectroscopic and microscopic experiments that characterize the carrier dynamics associated with defect states and electron-hole plasma formation from specific regions in a single structure.



### 3.4 References

1. C. N. Fleming, K. A. Maxwell, J. M. DeSimone, T. J. Meyer, J. M. Papanikolas, *Journal of the American Chemical Society* **2001**, *123*, 10336.
2. J. R. Lakowicz, *Principles of Fluorescence Spectroscopy*, 3rd ed., Springer, New York, **2006**.
3. A. Siegman, *Lasers*, University Science Books, Sausalito, **1986**.
4. W. Demtroder, *Laser Spectroscopy*, 3rd ed., Springer, Berlin, **2003**.
5. R. Paschotta, *Encyclopedia of Laser Physics and Technology*, Wiley-VCH, Weinheim, **2008**.
6. E. W. M. Born, *Principles of Optics*, University Press, Cambridge, **1999**.
7. P. Prasad, *Introduction to Biophotonics*, John Wiley & Sons, Hoboken, **2003**.
8. W. R. Zipfel, R. M. Williams, W. W. Webb, *Nature Biotechnology* **2003**, *21*, 1368.
9. H. Y. Sun, *Optical Engineering* **1998**, *37*, 2906.
10. S. A. Self, *Applied Optics* **1983**, *22*, 658.
11. D. C. Harris, *Quantitative Chemical Analysis*, 5th ed., W.H. Freeman and Company, **1998**.
12. M. K. Brennaman, University of North Carolina at Chapel Hill (Chapel Hill), **2004**.
13. A. B. Djuricic, Y. H. Leung, *Small* **2006**, *2*, 944.
14. B. Cheng, W. S. Shi, J. M. Russell-Tanner, L. Zhang, E. T. Samulski, *Inorganic Chemistry* **2006**, *45*, 1208.
15. F. Li, Z. Li, F. J. Jin, *Materials Letters* **2007**, *61*, 1876.
16. Q. J. Yu, C. L. Yu, H. B. Yang, W. Y. Fu, L. X. Chang, J. Xu, R. H. Wei, H. D. Li, H. Y. Zhu, M. H. Li, G. T. Zou, G. R. Wang, C. L. Shao, Y. C. Liu, *Inorganic Chemistry* **2007**, *46*, 6204.
17. C. Zhang, University of Chapel Hill at North Carolina (Chapel Hill), **2009**.
18. J. Tang, X. Q. Cui, Y. Liu, X. R. Yang, *Journal of Physical Chemistry B* **2005**, *109*, 22244.

## **CHAPTER 4**

### **Characterizing Charge Carrier Trapping in Single ZnO Rods**

## 4.1 Introduction

The ability to manipulate the shape of ZnO structures is enormous, and through a variety of facile synthetic methods many different forms, including nanorods with differing end morphologies, tetrapods and nanohelices have been created, to name a few.<sup>1-3</sup> The size of these structures, which can vary from tens of nanometers to many microns, provides for ultra-small scale electronic devices, and the prismatic shapes of the crystalline structures give rise to optical cavities that can be exploited in optoelectronic and photonic applications<sup>4-13</sup>.

Finite-sized structures introduce new phenomena not found in bulk materials. The electronic and photophysical behavior are strongly influenced by the surfaces and intrinsic defects, which trap mobile carriers, result in band bending and internal electric fields.<sup>14-16</sup> As a consequence, the spectroscopy often depends upon the size and shape of the particle,<sup>2</sup> and significant heterogeneity of the carrier dynamics from one object to the next is frequently observed.<sup>18, 19</sup> Carrier confinement and electric field enhancement associated with sharp features in high-aspect structures, or spatial variation in defect density across an object can influence carrier relaxation and result in a spatial variation in the dynamical behavior, leading to photophysical behaviors that differ from one point to another within an individual object. We have characterized the trap recombination dynamics in needle-like ZnO rods on ultrafast time scales using time-resolved two-photon emission microscopy. Our experiments excite a localized region (350 nm diameter) of a micron-size rod, and reveal that different points within the same structure (e.g. end vs. middle) can exhibit distinctly different trapping behaviors, thus providing a novel perspective of the role of native defects in the excited state trap recombination dynamics of ZnO nanostructures.

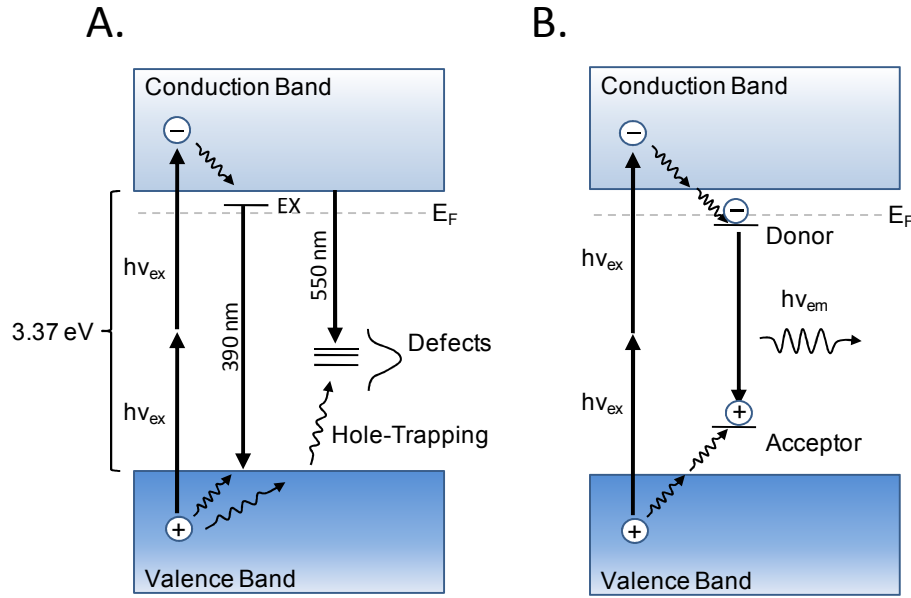


**Figure 4.1:** Band-diagram depicting the photophysical transitions that give rise to the emission bands in ZnO following a two-photon excitation. Electrons can either relax into excitonic states and recombine with a hole in the valence band, giving rise to band-edge emission centered around 390 nm, or fall into trap states localized within the band-gap giving rise to low-energy emission centered around 550 nm. A) Depicts recombination between an electron in the conduction band and a hole localized on an acceptor trap state. B) Depicts recombination between an electron localized on a shallow donor trap state and an electron bound to an acceptor trap state.

The general aspects of ZnO photophysics can be discussed using the band diagrams illustrated in Figure 1. ZnO is wide band-gap semiconductor ( $\sim 3.37$  eV) with a large exciton binding energy (60 meV), both of which make it attractive for technologies such as solar energy conversion and blue light emitting diodes, to name a few. Photoexcitation in the UV (or simultaneous two-photon excitation in the near infrared) promotes an electron from the valence band to the conduction band to create free carriers that can either relax into excitonic states that lie just below the conduction band edge or decay into trap states associated with defects in the crystal lattice or at the surface. Exciton recombination gives rise to UV-blue emission that is generally centered at  $\sim 390$  nm. Defect states, which are localized within the

band-gap offer additional pathways for electron-hole recombination and give rise to a broad visible emission band extending from 500-650 nm.

There are several types of transitions that can give rise to trap emission, including donor recombination with a hole in the valence band ( $D \rightarrow h^+$ ), acceptor recombination with an electron in the conduction band ( $A \rightarrow e^-$ ) and recombination between an electron localized on a donor with a hole localized on an acceptor. The latter mechanism is known as donor-acceptor pair (DAP) recombination,<sup>20</sup> occurring between donor and acceptor defects that are in close proximity within the crystal lattice. Since ZnO is an intrinsic n-type semiconductor,<sup>21</sup> the Fermi energy lies close to the conduction band, therefore all acceptor defects will be in a fully ionized state. The overall negative charge attracts and traps photogenerated holes, making the probability for donor recombination with the valence band unlikely.<sup>3, 22</sup> The most likely transition mechanisms are therefore between DAPs (Figure 4.1A) and  $A \rightarrow e^-$  (Figure 4.1B). The main focus of this chapter is the temporal evolution of the defect emission band and the carrier trapping that occurs following photoexcitation.

Time-resolved photoluminescence spectra reveal a dynamic red shift in the trap emission spectrum that is attributed to donor/acceptor pair (DAP) recombination. Annealing at high temperatures causes a blue-shift in the static spectrum, consistent with reduction in the DAP density giving rise to higher energy emission from trap recombination between acceptor bound holes with electrons in the conduction band. The defect emission spectrum is therefore described as a superposition of two bands, a low energy component due to DAP recombination and a higher energy component due to  $A \rightarrow e^-$  transitions. Experiments performed at different points in the same structure (e.g. end vs. middle) exhibit evidence for

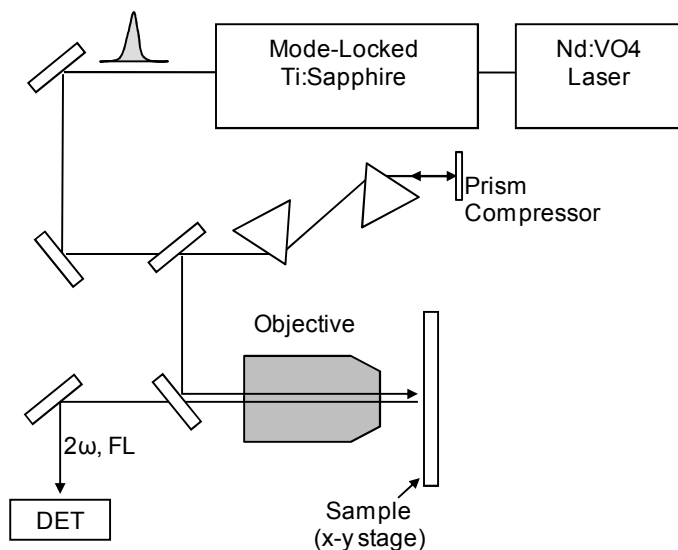


**Figure 4.2:** Schematic depiction of the two-photon microscope setup. Pulsed light exiting the laser system is sent through a prism compressor to control pulse dispersion. Excitation light is reflected off a dichroic mirror and excites the sample at the focal point of the objective. The resulting fluorescence is collected back through the objective, focused into the entrance slit of a monochromator and detected using a photomultiplier tube.

different trap recombination dynamics that is attributed to a spatial variation in the defect density.

## 4.2 Experimental

*Materials:* The ZnO rods were grown using a hydrothermal method adapted from work conducted by Cheng et al. and Li et al. The procedure, which involves heating a 0.05 M reaction solution of  $\text{Zn}(\text{NO}_3)_2$  and methenamine ( $(\text{CH}_2)_6\text{N}_4$ ) in a closed bomb, typically yields needle shaped rods ranging from 5-30  $\mu\text{m}$  in length and 0.5 to 2  $\mu\text{m}$  in width. The size is controlled by varying reaction temperature, time and/or concentration. After completion of the reaction, structures are harvested and sonicated in ethanol (200 proof) to break up aggregates and form a suspension. Microscopy samples are prepared by drop-casting  $\sim 250$   $\mu\text{L}$  of the suspension onto a microscope slide with an etched reference grid. The reference

grid facilitated the relocating of the rod for subsequent experiments in the optical microscope or structural characterization via scanning electron microscopy imaging. Once the ethanol evaporates, the slide is placed on the scanning stage with the ZnO rods facing the objective lens. Imaging is performed without a cover-slip under ambient conditions.

*Two-Photon Microscopy:* The microscope consists of a mode-locked Ti:Sapphire laser (Spectra Physics Tsunami) pumped by a 5W frequency doubled continuous-wave diode laser (Spectra Physics Millennia). The system produces pulses with an 80 fs width at a repetition rate of 76 MHz, and a tuning range between 720-850 nm with a maximum power output of approximately 1 W. The output is sent through a Faraday isolator and then directed through a prism-pair compressor operated in a double pass configuration (Figure 4.2). The pulse energy entering the microscope is reduced using a variable attenuator constructed from a half wave-plate and polarizing cube to between 0 and 1 nJ/pulse.

The microscope employs an inverted design with its objective located below the sample plane. The femtosecond laser beam is expanded by a lens pair, reflected off a dichroic mirror (R: 680-1000 nm, T: 360-650 nm) and then directed into the objective (Olympus MSPlan 50x, NA 0.8), overfilling its input aperture. The sample is raster-scanned across the focal point of the objective using a piezoelectric x-y translation stage (Queensgate NPS3330 Controller/Stage System) with a step-size and reproducibility that are both less than 20 nm. Two-photon emission and second harmonic light emanating from the sample are collected by the objective. Light transmitted through the dichroic beamsplitter is focused onto the entrance slit of a monochromator and detected by a photomultiplier tube (PMT) operated in a photon-counting mode. Under typical experimental conditions, the sample emits or generates a signal photon every 500 to 1000 laser pulses. The PMT output is sent to a discriminator and

a counter located on a data acquisition card (Model PCI 6602, National Instruments). In addition to the photon counting detection used for imaging, the emitted light can be directed into a time-correlated single-photon counting instrument to obtain time-resolved emission data with an approximately 100 ps instrument response or a streak camera with approximately 20 ps time resolution. The pulse repetition rate is reduced for time resolved emission measurements by a factor of 10 using an acousto-optic modulator.

The lateral resolution of the microscope is determined by the size of the laser beam at the focal point of the objective. Since the probability of two-photon excitation and second harmonic generation scales with the square of the laser intensity, efficient excitation occurs only at the focal point, resulting in confocal-like behavior and a lateral resolution that is smaller than the diffraction limit. The diameter of the excitation region is estimated to be approximately 350 nm. Images obtained from 100 nm fluorescent beads yield a point spread function width of  $\sim 400$  nm. Samples are placed on a glass substrate with an etched grid so that individual objects examined in the optical microscope can also be located in a scanning electron microscope (SEM) to obtain high-resolution structural images.

Although the images were not sensitive to the pulse energy, other spectroscopic measures (e.g. emission spectra and lifetimes) were intensity dependent, indicating that the photophysics of these materials depend upon carrier concentration at high excitation intensities. To avoid intensity dependent effects, the experiments discussed in this chapter were performed at successively lower pulse energies until a limiting value of the photoluminescence lifetime was obtained. This was typically less than 0.3 nJ/pulse. All experiments were performed in this low-pulse energy regime.



### 4.3 Results and Discussion

The discussion of the experimental results is divided into three sections. Section 4.3.1 describes the two-photon imaging of individual structures that is achieved by raster scanning the sample across the focal point of the objective. The rods are excited with a near infrared laser pulse focused to a diffraction limited spot by a microscope objective. Because the resulting two-photon excitation region is small (350 nm) compared to the rod's size (5-10  $\mu\text{m}$  in length), only a portion of the rod is excited. Spectroscopic measurements at specific points (e.g. middle or end of the rod) are performed by positioning the excitation spot over a specific part of the structure and monitoring the photoluminescence in either a time-integrated or time-resolved fashion. Section 4.3.2 describes photoluminescence spectroscopy and Section 3.3 reports the results of time-resolved measurements that probe the carrier percolation through defect sites and subsequent trap mediated recombination dynamics.

#### 4.3.1 Two-Photon Imaging

Photoluminescence images obtained via collection of the band-edge (390 nm) and trap emission (550 nm) following two-photon excitation of a single ZnO needle-shaped structure at 730 nm are shown in the right two panels of Figure 4.3. Upon completion of the two-photon emission imaging, the samples are removed from the optical microscope and detailed structural images are obtained in a scanning electron microscope (SEM), Figure 4.3 (left). The SEM image of this rod, which is typical of the size and shape of the ZnO rods used in this experiment, shows it to be a crystalline structure  $\sim 10\ \mu\text{m}$  in length ( $\sim 1.5\ \mu\text{m}$  at its widest point), with a hexagonal cross-section that tapers to approximately 300 nm at the ends. The two-photon emission images in the exciton and trap emission channels show significant variation in the emission intensity across the structure. Evident in both images are

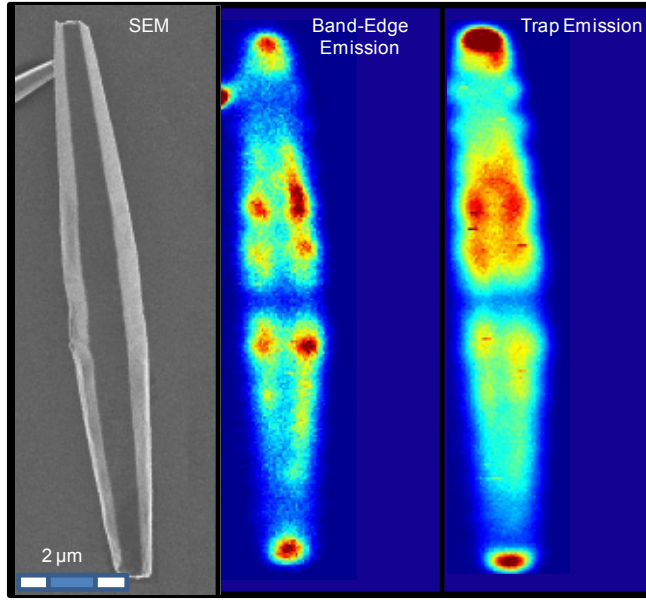


**Figure 4.3:** (Left) A scanning electron microscopy image of a typical ZnO rod used in our experiments. The structure is  $\sim 10\ \mu\text{m}$  in length and  $\sim 1.5\ \mu\text{m}$  in the center, tapering down to  $\sim 500\ \text{nm}$  at the end. (Middle) Band-edge emission (390 nm) and (Right) trap (550 nm) emission images. Each image shows enhanced intensity at the ends of the structure, due to a greater propensity for light to couple into optical cavity modes at that location (see text). The dark area in the center is attributed to the presence of a grain boundary. The enhanced intensity at the facet vertices may be due to light coupling into whisper gallery modes (see Figure 4.4 and text).

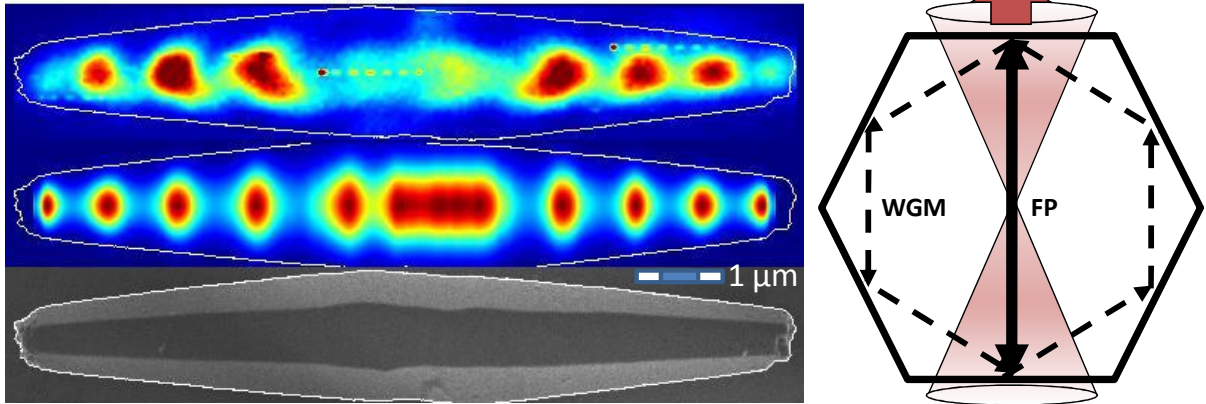


**Figure 4.4:** (Left) A second harmonic image of the ZnO rod shown in the lower panel. The image in the center represents the results of modeling the process giving rise to the periodic pattern. The rod's cross-sections supports Fabry-Perot and whispering gallery modes. The degree of coupling into the modes depends on cross-sectional diameter which changes as the rod taper from the middle to the ends. Refer to Mehl et al.<sup>17</sup> for further detail.

areas of low intensity in the middle of the rod, enhanced emission along the hexagonal corners adjoining each facet and high intensity at the ends of the structure.

The darkened region near the rod center is observed in the band-edge and trap emission images of  $\approx 60$ -70% of the rods examined. Its location at the rod midpoint, and its extension across the rod seems to indicate the presence of a grain or twinning boundary that is not apparent in the SEM image. A grain boundary would increase the defect density, which could impact the band-edge and trap recombination in a couple of different ways. First, the defects will trap mobile carriers and bend the bands upward, resulting in a depletion of the mobile carriers that would suppress recombination of the band-edge electrons with the trapped holes, as well as exciton recombination. The high defect density would also provide additional non-radiative relaxation pathways that would compete with the radiative trap recombination events and decrease the photoluminescence lifetime and quantum yield of the trap emission. Lifetime measurements (Section 4.3.2) reveal faster trap emission decay at the rod midpoint relative to other positions within the rod, consistent with the presence of enhanced non-radiative decay at the midpoint. Both mechanisms would reduce the photoluminescence in the vicinity of the defect boundary, and could give rise to the darker region in the trap emission image. While it is unclear why the remaining 30-40% of the rods do not show this dark region, it could be a consequence of a difference in the nature of the grain boundary that was formed as the crystal grew in solution.

The enhanced intensity at the vertices suggests that the emission images are influenced by a complex optical mode structure. Similar intensity variation is observed in the second harmonic images,<sup>17</sup> where it is linked to the presence of optical cavity modes oriented transverse to the rod axis. The rod's cross-section supports both Fabry-Perot (FP) modes

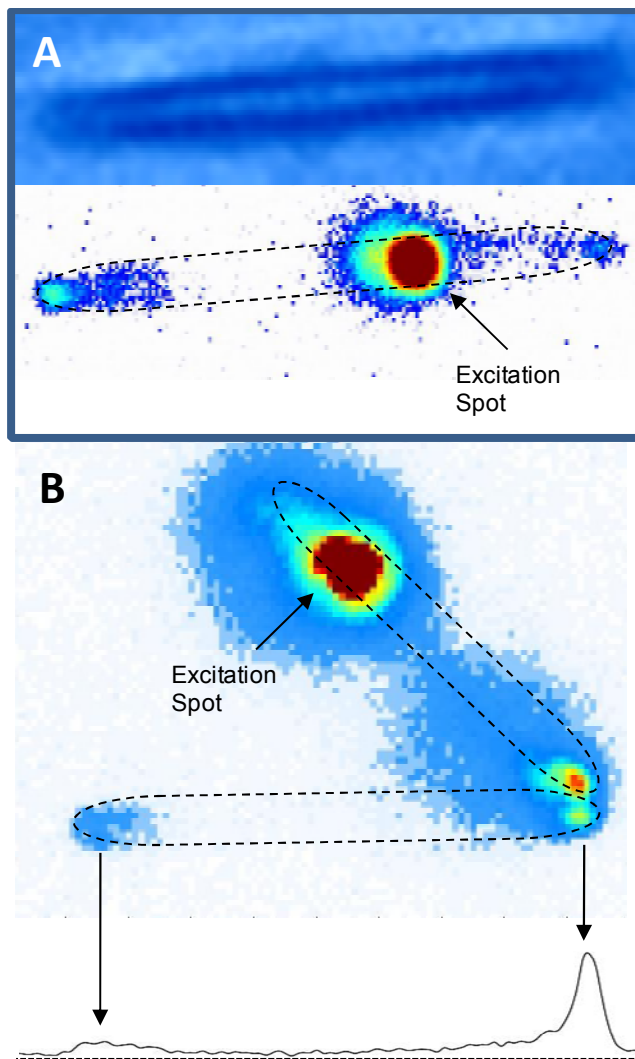


**Figure 4.5:** (A) Brightfield and corresponding fluorescence image (350 nm) collected using a CCD camera. The bright spot in the fluorescence image represents emission from the excitation region. Fluorescence emanating from the ends of the structure may be due to light coupling into wave-guiding modes in the cavity. (B) This observation is supported by two rods in close proximity at one end. Emission generated at one structure propagates and couples into the nearby structure, where it is further wave-guided to the opposing end. While wave-guiding is evident, the dominating process appears to be due to light coupling into the cavity at the excitation region.

between the parallel facets and ring-like cavity modes arising from total-internal reflection off each of the six facets, called whispering gallery modes (WGM). Because the cross-sectional diameter of the needle-like structures changes along the long axis of the rod, optical resonances will appear at distinct locations along the rod (Figure 4.4). It is this periodic variation that suggests that the intensity modulation is the result of optical cavity modes and not simple prism effects that redirect light back towards the objective. In principle either resonance type (FP or WGM) could influence the emission images; however the enhanced

intensity at the vertices suggests that it is the whispering gallery modes that give rise to the intensity modulation observed in these images.

To ascertain the extent of wave-guiding in our structures we imaged the fluorescence onto a CCD detector while the excitation spot is held fixed (Figure 4.5). The emission images shown in Figures 4.3 and 4.4, on the other hand, were obtained by scanning the excitation spot across the structure and collecting all of the emission in the objective's field of view. The bright spot in the middle of the rod is due to the intense emission created by the focused laser beam, while the two dimmer spots on either side represent photoluminescence that is emanating remotely from the rod ends. This emission could arise from either carrier transport or photoluminescence that is wave-guided from the excitation region to the ends of the rod. Enhanced emission at the rod ends has been observed in the images obtained by other groups,<sup>13, 23</sup> and attributed to wave guiding along the longitudinal axis of the structure. However, those images were obtained using an experimental arrangement in which the entire rod was excited and the resulting photoluminescence collected by the objective was imaged on a CCD detector. The relative absence of emission from the interior of the rod (other than the excitation point) suggests that it's the latter. This is corroborated by similar images obtained from closely spaced objects. The bottom of Figure 4.5, for example, shows a loose network of two rods in close proximity at one end. Emission created at the excitation point of one rod propagates along that structure, couples into the nearby rod and is further wave-guided to its far end, underscoring the ability of these nanostructures to propagate light. Despite the obvious presence of wave-guiding in these images, the majority of the emission collected by the objective emanates from the location of the laser excitation, indicating that it does not appear to dominate the photonic properties of these structures. Given our

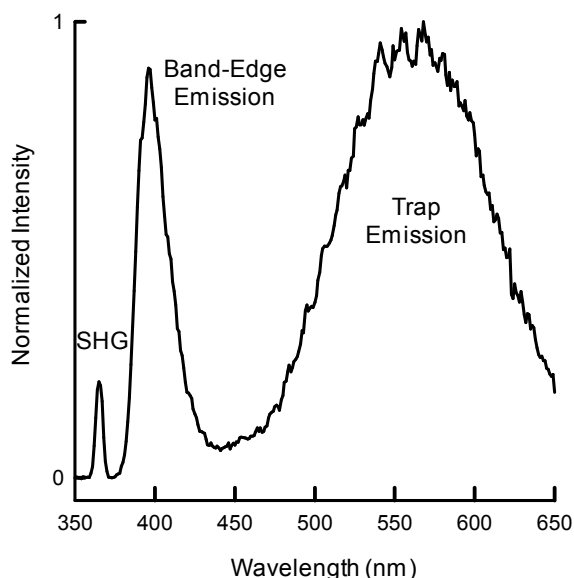


**Figure 4.6:** ZnO emission spectrum following a two photon excitation in the center of the rod shown in Figure 4.3. The sharp feature centered around 365 nm corresponds to second harmonic generation. The emission band centered around 390 nm represents exciton and free-carrier recombination between the valence and conduction bands. The broad emission centered around 560 nm corresponds to recombination events involving trap states that are localized within the band-gap and arise due to defects in the crystal lattice.

experimental arrangement, the increased emission observed at the ends of the rods in the scanning two-photon image (Figure 4.3) more likely reflects a propensity of excitation light to couple into the structure at that location than a wave-guiding phenomenon.

#### 4.3.2 Photoluminescence Spectra

Figure 4.6 shows the photoluminescence spectrum obtained following localized 730 nm two-photon excitation in the midpoint of the rod depicted in Figure 3 under low laser fluence conditions. The two most prominent features in the spectrum are the narrow band-edge emission around 390 nm that is characteristic of exciton fluorescence and the much broader visible emission (500-650 nm) that arises from the trapping of charge carriers at defect sites. (The sharp feature centered at  $\sim 365$  nm corresponds to second harmonic that is generated by the ZnO.<sup>17</sup> The relative intensity of the trap emission compared with the band-edge emission at lower pulse energies is suggestive of a fairly high defect density.

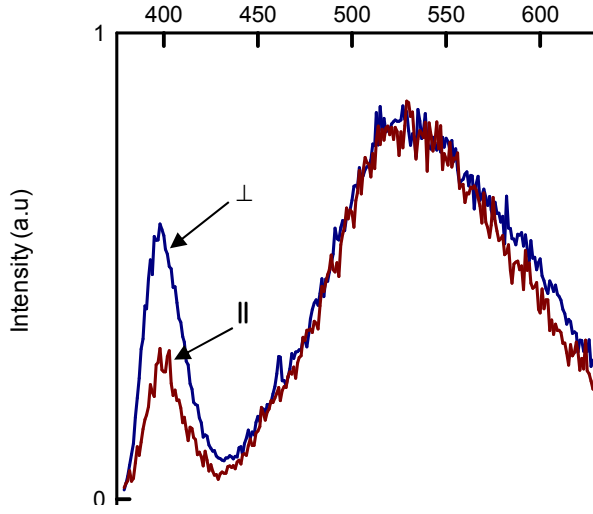
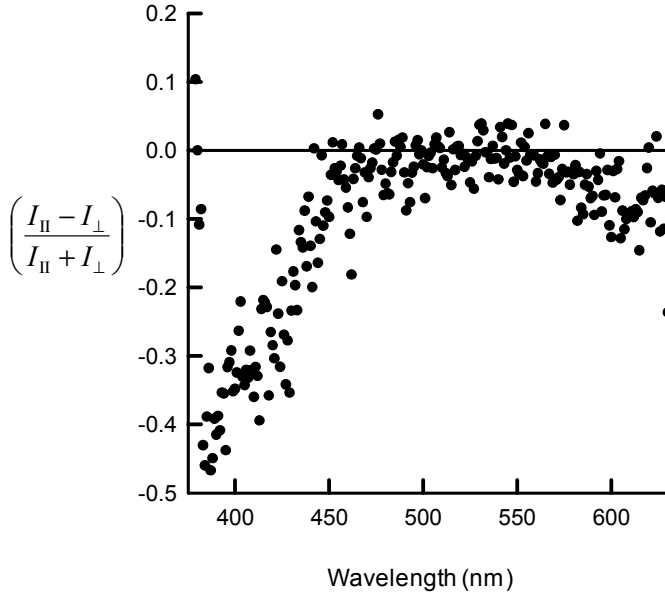


**Figure 4.7:** Polarization character of the band-edge and trap emission. Band-edge emission is predominantly generated perpendicular to the  $c$ -axis of the rod, with a -0.43 polarization ratio of. The trap emission shows no dependence on polarization.



The precise mechanisms that give rise to the broad defect emission in ZnO remains highly controversial. This is exacerbated by the dependence of visible emission on particle shape, size<sup>18</sup> and synthetic procedure.<sup>1, 21, 24</sup> The most common defects in ZnO are extrinsic impurities, intrinsic lattice defects and surface atom dangling bonds<sup>21, 24, 25</sup>. The point defects commonly occurring in the lattice are either oxygen or zinc vacancies, each of which can exist in neutral, single or doubly ionized states. The extrinsic defects can arise as a result

of intentional doping or reaction conditions during synthesis and/or annealing. Extrinsic impurities commonly cited in the literature include lithium, copper, nitrogen and hydrogen. Given their large surface-to-volume ratio, the visible emission from smaller structures has generally been attributed to surface states. Surface emission has also been implicated in the photoluminescence of larger structures, which is a reasonable assignment given the shallow penetration depth of the UV light ( $\approx 100$  nm) used in single-photon absorption experiments.<sup>13, 18, 26, 27</sup> However, since near infrared light is not absorbed by ZnO, two-photon excitation is not limited to being near the surface and can occur anywhere within the structure. As a consequence, the majority of the defect emission in our experiments probably originates from photogenerated holes trapped at the lattice defects (most likely zinc vacancies) with mobile carriers located near the Fermi energy ( $E_F$ ).

The band edge and trap emission spectra also have different polarization characteristics. Figure 4.7 shows the photoluminescence spectra detected either parallel or perpendicular to the  $c$ -axis of the rod. The band-edge emission is polarized preferentially perpendicular to the rod with a polarization ratio,  $\rho_{||}=(I_{||}-I_{\perp})/(I_{||}+I_{\perp})$ , of -0.43. This is consistent with measurements performed on bulk crystals that show the exciton transition dipole to be oriented perpendicular to the  $c$ -axis.<sup>26-28</sup> The trap emission in our structures is unpolarized ( $\rho_{||} = 0.04$ ). This is in contrast to several reports of anisotropic trap emission observed in high surface-to-volume structures, which would seem to implicate the role of surface states in the trap mediated recombination. The lack of anisotropy observed in our data is consistent with our expectation that the defect emission arises from the interior of the structure.



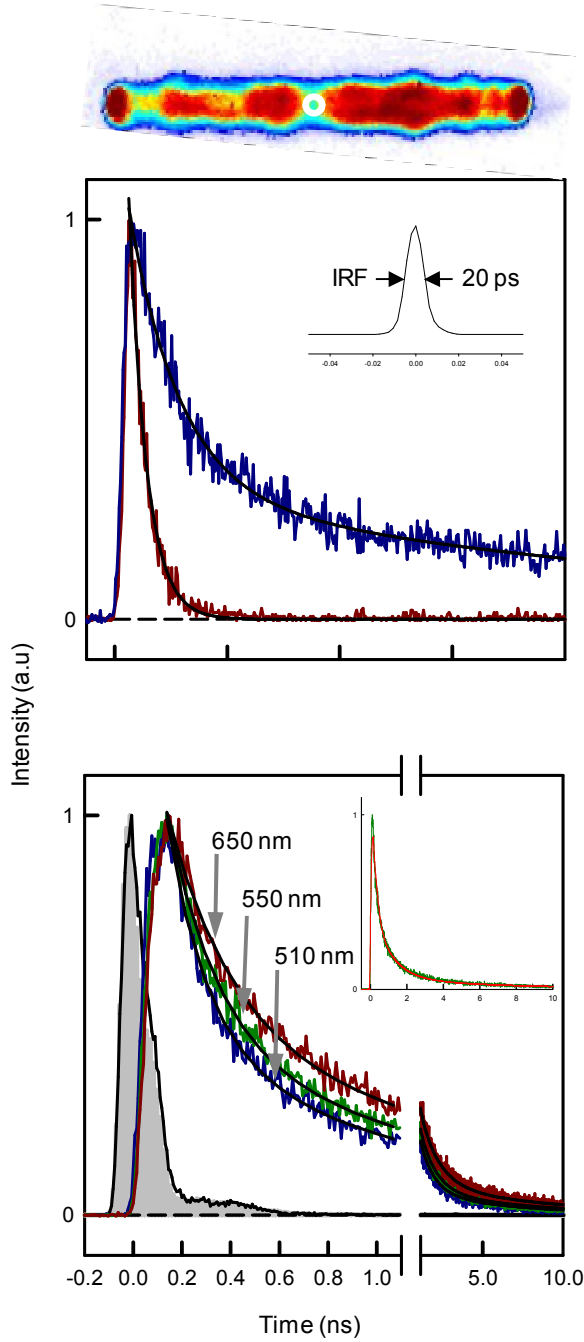


**Figure 4.8:** Time-resolved photoluminescence measurements collected using a streak camera (*top panel*) and time-correlated single-photon counting (TCSPC) instrumentation. The streak-camera time resolution is  $\sim 20$  ps (shown in the inset) enabling us to time resolve the band-edge emission. Although a delayed rise in the trap-emission band appears to exist in the TCSPC data, the streak camera data suggests it does not. Convoluting the TCSPC trap emission transient with the instrument response function confirmed the appearance of the delayed rise is an experimental artifact (shown in the inset with the TCSPC data). The transients are consistent with reports in the literature that report the band-edge emission decays within 50-100 ps. The trap emission bands are multi-exponential, displaying a fast sub-nanosecond component, followed by slower components that decay in 10-100's of nanoseconds. The data were collected from the center of the structure shown above, as indicated by a white circle.

#### 4.3.3 Time Resolved Photoluminescence

The carrier recombination dynamics in individual structures were characterized using ultrafast emission methods, including time-correlated single photon counting (100 ps time resolution) and streak camera detection (20 ps time resolution). Figure 4.8 shows the decay

of the band-edge (390 nm) and trap emission (550 nm) following the excitation of a localized spot in a single ZnO structure with a 730 nm laser pulse. The band edge emission decays with an approximately 30 ps lifetime (Figure 4.8, top). This is consistent with experiments conducted on bulk or thin film ZnO by other groups that show a band-edge emission lifetime of 50-100 ps resulting from free exciton recombination. The decay of the trap emission is multiexponential, with time components ranging from sub-nanosecond ( $\sim 100$ -250 ps) to 10-100's of nanoseconds (Figure 4.8, bottom), the longer of which are consistent with previous reports.<sup>29, 30</sup> The absence of a delayed rise in the trap emission (Figure 4.8, top) suggests that the initial trapping events occur within the first 20 ps following excitation.

Measurements performed at different locations within individual structures exhibit different decay kinetics, indicative of a spatial heterogeneity in the trap recombination dynamics. Shown in the top of Figure 4.9 are defect emission transients collected at 550 nm from three different locations (middle, left middle and end) in a single ZnO rod, whose trap emission image is shown as the inset. The faster emission decay in the middle of the rod compared to the two other locations indicates the presence of faster trap recombination in that region. In the image, this region corresponds to the area of low intensity that extends across the midpoint of the structure. The faster decay kinetics at this location indicates an increase in the non-radiative rate and is consistent with a greater defect density in the vicinity of the grain boundary. This may arise due to an increased density of trap states, perhaps due to a twinning boundary that enhances the non-radiative relaxation pathways.

Closer inspection of the three transients at early times ( $<1$  ns) shows that the end and middle of the rod decay at similar rates, whereas at longer times the end resembles the decay

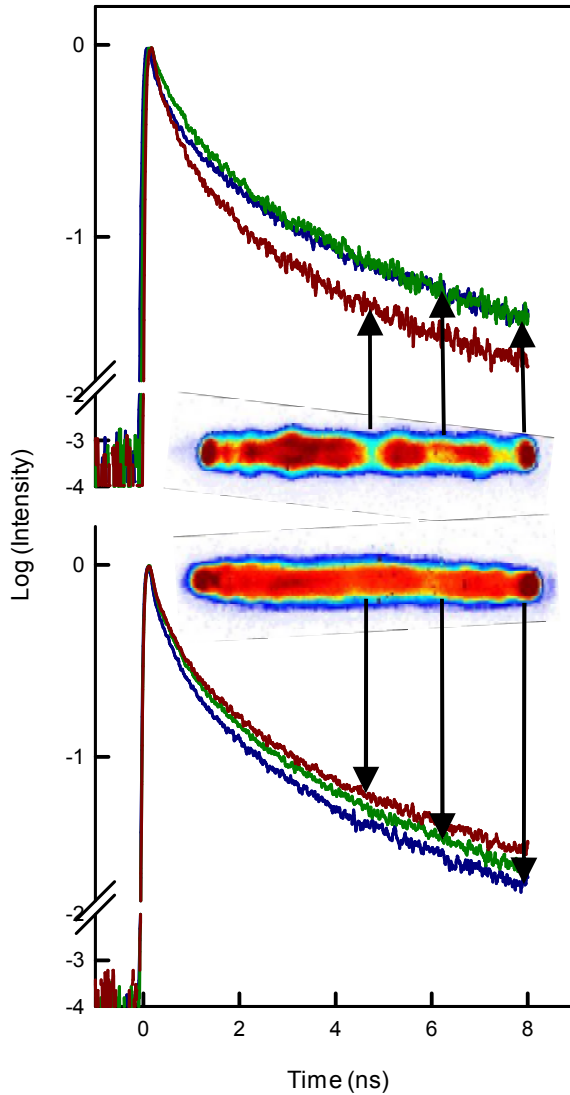


**Figure 4.9:** Defect emission kinetics depend on local structural region. Examples of data collected from the middle, left middle and end of structures with (*top*) and without (*bottom*) a grain boundary in the center are shown. In the structure with a grain boundary the emission decays faster in the center consistent with an increase in the non-radiative rate due to the increased defect density around the grain boundary. The kinetics from the left-middle resembles the transient from the middle at early times, and the end position at later times. The structure with no grain boundary displays different behavior. Here the kinetics from the end is faster than the middle, consistent with a lower defect density in the middle of the structure.

of the right-middle. The interpretation of this is not entirely clear, but suggests a similarity in initial recombination events between the two different regions.

While the majority of rods (60-70%) show the decreased intensity in the trap emission image at the rod mid-point, in the rest the dark region is less apparent or absent altogether. The lower panel shows a similar set of transients obtained from such a rod. In these rods the emission decay occurs slowest in the middle of the structure and more rapidly at the end, suggesting a lower defect density at the rod midpoint. Together these results

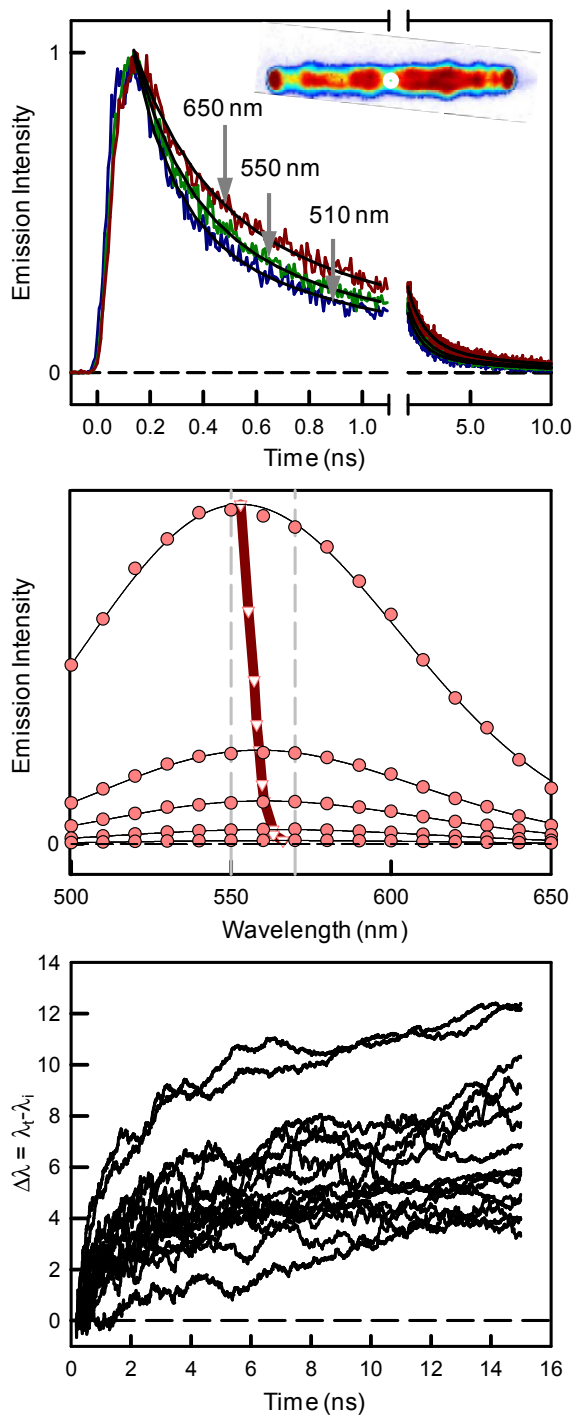


**Figure 4.10:** Time-resolved data before annealing. The top panel shows the emission kinetics, with a faster decay observed at higher energies. The time-dependent spectra shown in the middle row reveals an 8-10 nm red-shift before annealing. The rate of the shift from 16 rods is displayed in the bottom panel. The red shift varies in magnitude between 4 and 10 nm and occurs within the first 4-6 ns following photoexcitation.

underscore the potential for different dynamical behaviors to occur at different locations within the same structure.

#### 4.3.4 Trapping Dynamics

Comparison of trap emission transients collected at different wavelengths show that the emission decays more slowly at the red edge of the emission band (Figure 4.10). Emission spectra at different times were reconstructed from emission decays obtained at a series of detection wavelengths collected every 10 nm between 470 and 600 nm (Figure 4.10 top). The individual points correspond to the emission intensity observed at 0.2, 1, 2, 5 and 15 ns after photoexcitation; the solid lines show the result of fitting each spectrum to a stretched Gaussian function:

$$f(x) = a * \exp\left(\frac{-0.5(x - x_0)^2}{b + d(x - x_0)}\right) \quad (42)$$

The emission spectra show a time-dependent red-shift of ~10 nm during the first 15 ns after photoexcitation, as depicted by the bold line connecting the maximum of each of the spectra.

The magnitude of the spectral shift in the emission maximum ( $\Delta\lambda = \lambda_t - \lambda_i$ ) taken from 16 different rods, is displayed as a function of time in the bottom panel of Figure 4.10. We consistently observe the red-shift in all the structures and the magnitude generally ranges from 3 nm to 12 nm, with the majority shifting between 4 and 8 nm. The shift exhibits multiple kinetic components, with a rapid shift of the band occurring at early times (~2 ns), followed by a slower shift (~4-6 ns) to its asymptotic wavelength.

We attribute this time-dependent spectral shift to the presence of a high defect density that gives rise to donor-acceptor pairs (DAPs) in close proximity to each other within the crystal lattice. The recombination energy (i.e. emission energy) of DAPs can be described by the following:<sup>20</sup>

$$\Delta E = E_g - E_D - E_A + \frac{e^2}{(\epsilon d)} \quad (43)$$

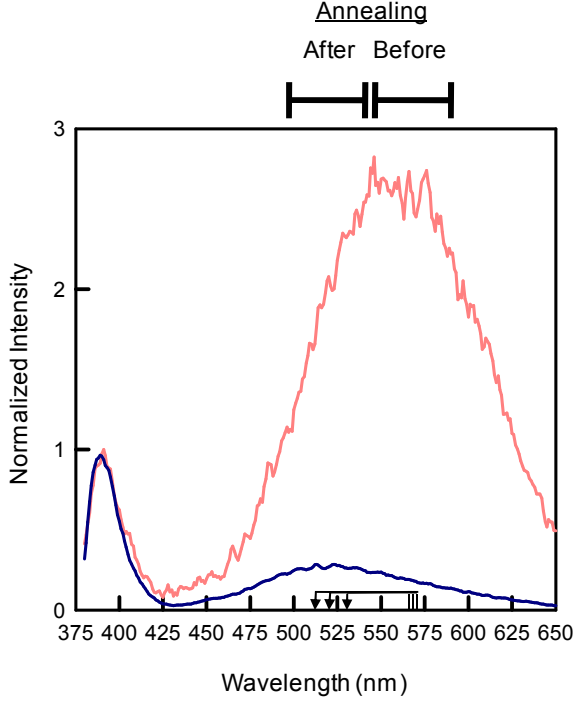


**Figure 4.11:** Steady-state spectrum from the same position in the same rod, collected before and after annealing. The graphs are normalized to the maximum of the band-edge emission. We observe an  $\sim 40$  nm blue-shift in the spectrum following annealing, in addition to a drastic reduction in the overall intensity of the trap emission band. The magnitude of the spectral shift from four other structures is displayed by a series of arrows originating at the spectral maximum before annealing and terminating at the maximum following annealing.

Annealing crystalline materials at high temperatures is a well-established method of reducing the defect density in semiconductor systems. Figure 4.11 shows emission spectra acquired from a single ZnO rod before and after annealing. First, the emission spectrum was obtained from the as-grown structure. The rod was then annealed at  $550^{\circ}\text{C}$  for 4 hours and subsequently allowed to cool to room temperature, at which point the spectrum from the

where  $E_g$  is the band gap energy,  $E_D$  and  $E_A$  are the donor and acceptor energy respectively,  $\epsilon$  is the dielectric constant and  $d$  is the average distance between the donor and acceptor. This equation dictates that there is an inverse relationship between the DAP energy ( $\Delta E$ ) and the separation ( $d$ ). Because pairs that are in close spatial proximity experience greater wave function overlap, they recombine faster than those that are further apart. The result is an initially blue photoemission that shifts to the red as time progresses.

*Affect of Annealing:* If the interpretation above is correct, then decreasing the defect density should decrease the DAP concentration, shutting down the time-dependent red-shift of the trap emission.

*same* location in the *same* rod was measured. Annealing alters both the position and intensity of the emission band. Before annealing, the trap emission intensity is 130% that of the band edge emission, which decreases to 15% after annealing. This reduction in the intensity of the trap emission is indicative of an overall reduction in the defect density.

Annealing also alters the position of the emission band. The two spectra shown in the figure display a distinct blue shift from about 560 nm before annealing to approximately 520 nm afterwards. While the  $\sim 40$  nm ( $\sim 0.2$  eV) blue-shift occurs with little change in the width of the spectrum, there appears to be a slight distortion of the spectrum with a tail extending towards longer wavelengths. A similar (10-40 nm) blue-shift has been observed in the majority of rods we have analyzed, with a minority displaying a shift of lesser magnitude ( $\sim 5$  nm). The magnitude of the spectral shift observed in four additional structures is depicted in the figure as a series of arrows that originate at the maximum wavelength before annealing and terminate at the spectral maximum after annealing.

Red-shifts in the trap emission spectra following annealing of a variety of nanostructures (rods, needles and shells) have been reported, in contrast to the blue shift reported here.<sup>18</sup> Those experiments found that the shift in the spectrum depended on shape, with results ranging from no shift (in the case of nanoshells) to a large shift in nanorods. The difference between the affect of annealing observed in that work (red shift) and that observed here (blue shift) may stem from the population of surface versus interior trap states. The combination of UV excitation and small nanometer scale structures in those experiments likely results in the predominant population of surface defects. Two-photon excitation on the other hand generates carriers throughout the crystal, not just near the surface. The difference in observations may ultimately stem from different behavior in the surface and sub-surface

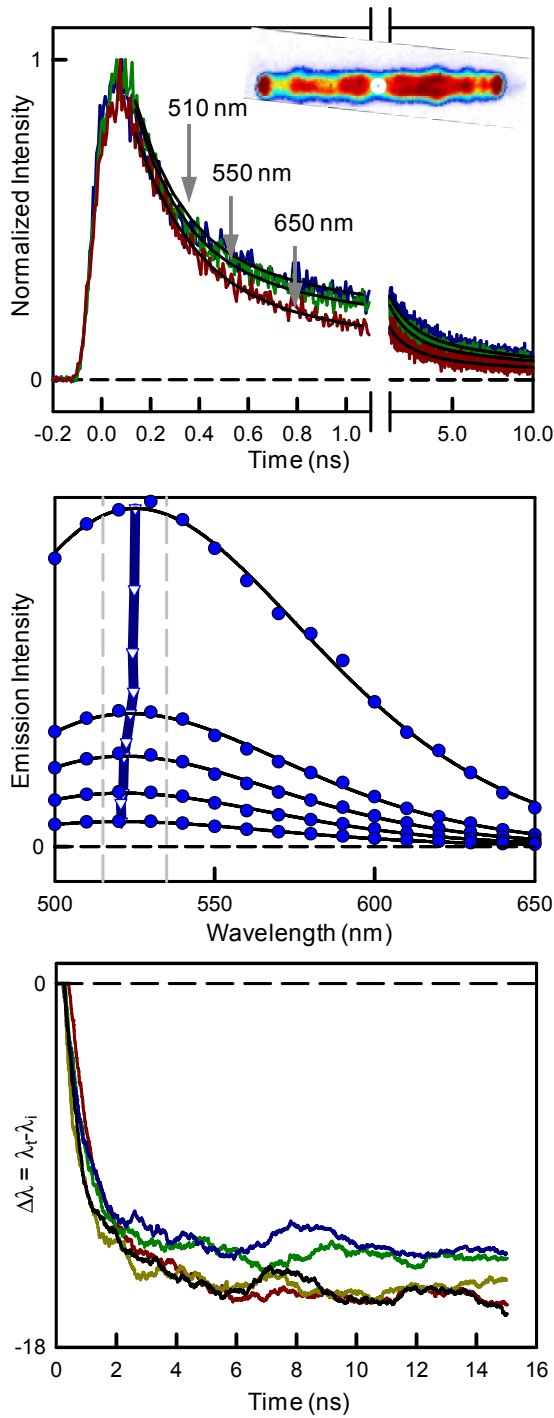


**Figure 4.12:** Time-resolved data taken after annealing. The top panel shows the emission kinetics have a faster decay at lower energies, in contrast to our observations before annealing. The time-dependent spectra shown in the middle row reveals an  $\sim 15$  nm blue-shift. The rate of the shift from 5 rods is displayed in the bottom panel. There is an  $\sim 15$  nm blue shift in each structure that occurs within the first 2 ns following photoexcitation.

regions of the object. Initial results probing different focal planes in the needle-like rods suggest that this may indeed be the case.



The blue-shift in the static spectrum is consistent with a reduction in low energy defects. Given the n-type character of native ZnO, the two most likely transitions giving rise to the trap emission band are between DAPs and acceptor-bound holes with the conduction band ( $A \rightarrow e^-$ ). Since the DAP transitions occur between localized states lying within the band-gap, they will be lower in energy compared to  $A \rightarrow e^-$  transitions. Furthermore, shallow defects cited in the literature, such as zinc and hydrogen interstitials, have low migration barriers and are therefore likely to be annealed from the structure at high temperature, disrupting the DAP transition. Given our synthetic procedure, these defects could also represent likely candidates for shallow donor states in our structures. We therefore assign the static spectrum to a superposition of two bands. The high band is attributed to  $A \rightarrow e^-$  transitions and the low energy band to DAP transitions. The blue-shift arises following the annealing of shallow donors from the structure, drastically reducing the DAP contribution and enhancing the  $A \rightarrow e^-$  emission.

The decay kinetics are also affected by annealing. The panel on the top of Figure 4.12 shows time resolved data collected from the same point in the same rod as depicted in Figure 10 after a 4 hour anneal at 550 °C. Analysis of the time-dependent data reveals the multi-exponential behavior is conserved in the transients, with a 200-250 ps fast time component and a slower  $\sim 1$  ns component, which are similar in magnitude to the faster decay components before annealing. However, in contrast to the data observed before annealing, the decay kinetics of the long time component are twice as long ( $>15$  ns), indicating trapping events that are occurring over a longer time. Furthermore, the transients at lower energies decay faster than those at higher energies, exactly opposite to our observations before annealing. Reconstruction of the emission spectrum (Figure 4.12 *middle*) reveals that it shifts

to higher energy over time, contrasting with the dynamic red-shift we observe before annealing. Data collected on five rods (Figure 4.12 *bottom*) show that the trap emission band shifts by  $\sim 15$  nm within the first 2-3 ns after excitation.

Given the differing reports in the literature, precise assignment of our spectroscopic observations is difficult. Among the different types of intrinsic defects (vacancies, interstitials and substitutions), perhaps the two most heavily cited for giving rise to the defect emission are oxygen ( $V_O$ ) and zinc vacancies ( $V_{Zn}$ ).<sup>21, 24</sup> In ZnO,  $V_O$  represents a donor type defect, and  $V_{Zn}$ , an acceptor. There have been numerous reports that attribute the defect emission to single ionized  $V_O$ .<sup>31-36</sup> If they are true, our observations could be explained by the photogenerated hole first localizing at this defect site (i.e.  $V_O^+ + h^+ \rightarrow V_O^{++}$ ) to produce a deep trap state that lies  $\approx 2$  eV below the conduction band edge;<sup>25</sup> photon emission occurs when the trapped hole recombines with a mobile carrier ( $e^-$ ) near the conduction band or in a shallow trap, i.e.  $V_O^{++} + e^- \rightarrow V_O^+ + h\nu$ . The latter would correspond to a DAP transition and would be consistent with the time-dependent red-shift. This would also result in a  $\sim 620$  nm photon, consistent with the low energy emission in the spectrum. However it should be noted that under n-type conditions, it is uncertain that  $V_O$  would exist in a singly ionized state ( $V_O^+$ ). Furthermore, the existence of  $V_O^+$  has been found to be thermodynamically unstable.<sup>21, 24</sup>

Another possibility is recombination with  $V_{Zn}$ . Since it is an acceptor defect and ZnO is intrinsically an n-type material, it will be doubly ionized in its native state ( $V_{Zn}^{--}$ ).<sup>21, 24, 25</sup> Upon photoexcitation, a hole in the VB edge ( $h^+$ )<sub>VB</sub> could localize on a  $V_{Zn}^{--}$  and recombine with an electron from the CB or a shallow donor, resulting in the emission of a photon ( $V_{Zn}^{-+} + (e^-)_{CB} \rightarrow V_{Zn}^{--} + h\nu$ ). There are discrepancies in the literature on the ionization energy of

$V_{\text{Zn}}^{--}/V_{\text{Zn}}^{-+}$  with reports placing it either 0.9 eV<sup>21, 37</sup> or 2.8 eV<sup>2, 25</sup> above the VB edge. Our data would be consistent with the former assignment, resulting in a ~500 nm photon which falls within the higher energy portion of the defect spectrum. Before annealing, the predominant transition would therefore favor DAP recombination between  $V_{\text{Zn}}^{-+}$  and a shallow donor. After annealing the ~0.2 eV blue-shift in the static spectrum would correspond to a depletion in the shallow donor population and the predominant transition would be between the conduction band and  $V_{\text{Zn}}^{-+}$ . Therefore, the drastic reduction in DAP concentration following annealing suggests that the time-dependent blue-shift is predominantly due to the  $A \rightarrow e^-$  transition.

There are several mechanisms that could give rise to this behavior. Given ZnO's rich defect chemistry,<sup>21, 24, 25</sup> it is probable that the high energy portion of the static spectrum arises from a superposition of two bands. Given our reaction conditions and the annealing atmosphere (air), a potential candidate (in addition to  $V_{\text{Zn}}^{-+}$ ) that is also an acceptor defect is Nitrogen.<sup>21, 24</sup> In this model, emission would arise from two different transitions, between carriers in the conduction band and two different acceptor defects that are separated by ~0.1 eV (the magnitude of the blue-shift). Following photoexcitation, carriers associated with the low energy transition recombine first, followed by the higher energy transition, giving rise to a time dependent blue-shift.

An alternative model can be described as follows. Immediately following photoexcitation an excess of free carriers are generated. Exchange interactions and correlated effects between free carriers cause the band-gap to renormalize to a lower energy.<sup>38, 39</sup> With exchange interactions, this occurs because the Pauli exclusion principle forbids two carriers with parallel spin to occupy the same unit cell. This increases the distance between carriers,

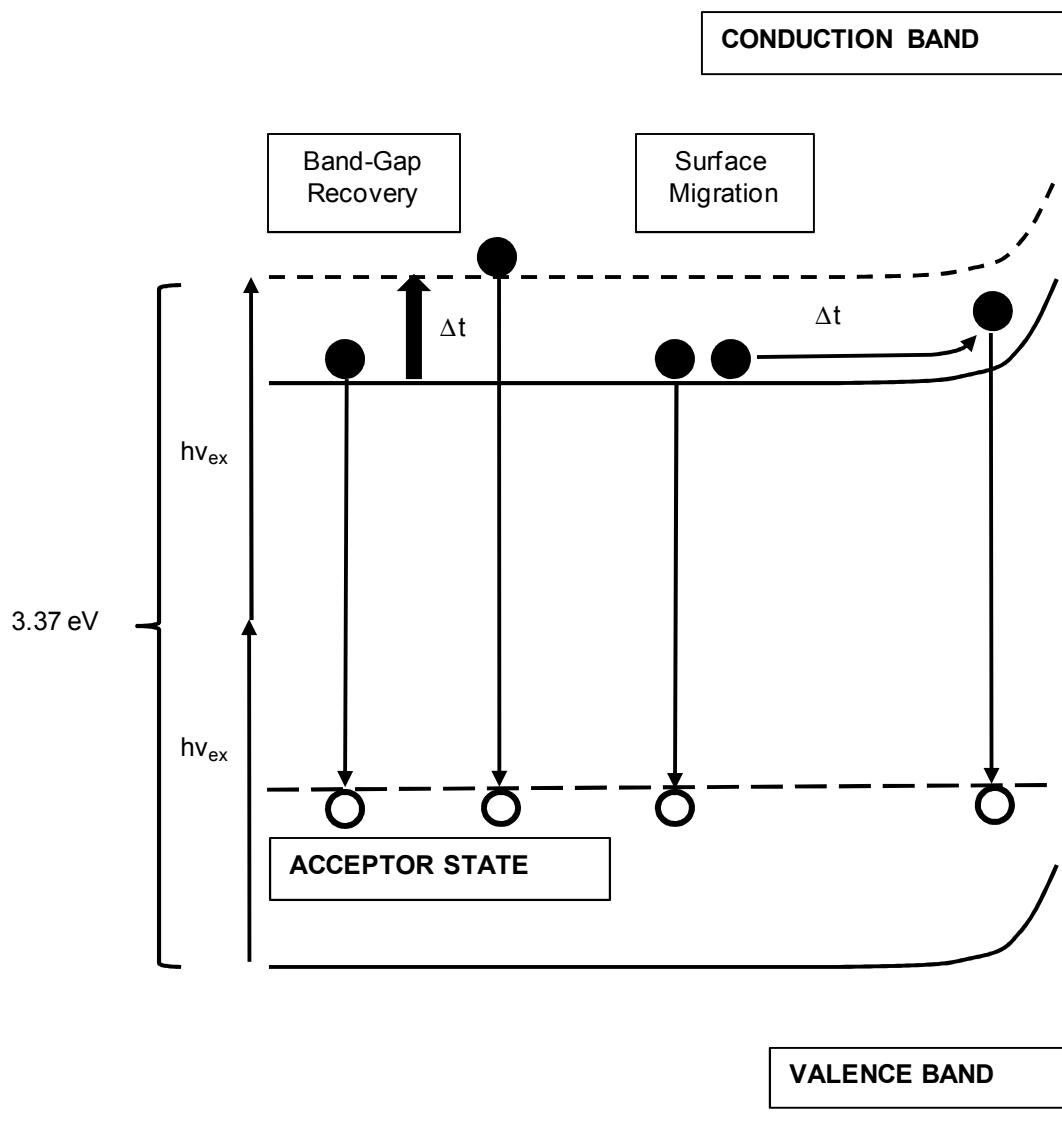


**Figure 4.13:** Schematic depiction of the proposed models that give rise to the time-dependent blue-shift. Follow photoexcitation, the excess free carriers that are generated cause a renormalization of the band gap. As the carriers begin to recombine, the band-gap recovers to its initial state (dashed line), and gives rise to a time-dependent blue-shift. Note the shift shown here is exaggerated for clarity. Additionally, those photoexcited carriers that migrate to the structure surface will move higher in energy as the bands bend upwards. This transition will only occur occasionally because of the depletion region at the surface. Therefore those carriers in the bulk will tend to recombine first, followed by the higher energy transitions on the surface.

thereby decreasing the Coulomb repulsive forces between them and lowering the total energy of the system. This can be enhanced since the probability of finding two oppositely charged particles in close proximity are higher than finding like charges (correlated effect). The Coulombic forces between the opposite charges stabilizes the carriers, which further reduces the system energy.<sup>38</sup> As carriers recombine and the free carrier density is depleted the system recovers to its initial state.

This recovery, from low to high energy causes the  $A \rightarrow e^-$  transition energy to increase with time, giving rise to the blue-shift in the transient spectrum (Figure 4.13). Additionally, as carriers migrate to the surface or grain boundary, the bands bend upwards to higher energy.<sup>40</sup> The trap state is not affected by the band bending,<sup>40</sup> so that the  $A \rightarrow e^-$  transition at the surface occurs at a higher energy (Figure 4.13). Since holes migrate slower than electrons, those that get trapped in the interior will recombine first (low energy), followed by the surface recombination (high energy), giving rise to the time dependent blue shift. This seems particularly relevant because of the observed grain boundary in the center of the rod where these measurements were taken (Figure 4.8). Furthermore, because the band-bending gives rise to a depletion zone, the hole will remain trapped longer before recombination, leading to the slow decay kinetics at longer times following annealing.

#### **4.4 Conclusion**

We utilize nonlinear microscopy methods to study the trap emission dynamics in single needle-shaped ZnO rods. Analysis of trap emission decays obtained using two-photon emission microscopy reveals a time-dependent spectral red shift in the trap band during the first 10-15 ns after photoexcitation, with a majority of the shift occurring at early times. We attribute these observations to a high DAP density that gives rise to differing recombination

rates. Following annealing, we observe a blue-shift in the spectral maximum of the steady-state trap band as well as a reduction in the trap emission intensity. We propose several models to explain this behavior.

#### 4.5 References

1. Z. L. Wang, *Journal of Physics-Condensed Matter* **2004**, *16*, R829.
2. A. B. Djuricic, Y. H. Leung, *Small* **2006**, *2*, 944.
3. U. Ozgur, Y. I. Alivov, C. Liu, A. Teke, M. A. Reshchikov, S. Dogan, V. Avrutin, S. J. Cho, H. Morkoc, *Journal of Applied Physics* **2005**, *98*.
4. S. H. Ju, K. Lee, D. B. Janes, *Nano Letters* **2005**, *5*, 2281.
5. H. T. Ng, J. Han, T. Yamada, P. Nguyen, Y. P. Chen, M. Meyyappan, *Nano Letters* **2004**, *4*, 1247.
6. W. I. Park, J. S. Kim, G. C. Yi, M. H. Bae, H. J. Lee, *Applied Physics Letters* **2004**, *85*, 5052.
7. Y. R. Ryu, T. S. Lee, J. A. Lubguban, H. W. White, B. J. Kim, Y. S. Park, C. J. Youn, *Applied Physics Letters* **2006**, *88*.
8. X. D. Wang, J. Zhou, J. H. Song, J. Liu, N. S. Xu, Z. L. Wang, *Nano Letters* **2006**, *6*, 2768.
9. Y. F. Chen, D. Bagnall, T. F. Yao, *Materials Science and Engineering B-Solid State Materials for Advanced Technology* **2000**, *75*, 190.
10. M. Law, D. J. Sirbuly, J. C. Johnson, J. Goldberger, R. J. Saykally, P. D. Yang, *Science* **2004**, *305*, 1269.
11. Y. R. Ryu, T. S. Lee, J. A. Lubguban, H. W. White, Y. S. Park, C. J. Youn, *Applied Physics Letters* **2005**, *87*.
12. H. C. Zeng, *Journal of Materials Chemistry* **2006**, *16*, 649.
13. J. C. Johnson, H. Q. Yan, P. D. Yang, R. J. Saykally, *Journal of Physical Chemistry B* **2003**, *107*, 8816.
14. E. Irene, *Electronic Materials Science*, John Wiley & Sons, Hoboken, **2005**.
15. M. W. Allen, C. H. Swartz, T. H. Myers, T. D. Veal, C. F. McConville, S. M. Durbin, *Physical Review B*, *81*.
16. Y. Y. Tay, T. T. Tan, M. H. Liang, F. Boey, S. Li, *Physical Chemistry Chemical Physics*, *12*, 6008.

17. B. P. Mehl, R. L. House, A. Uppal, A. J. Reams, C. Zhang, J. R. Kirschbrown, J. M. Papanikolas, *Journal of Physical Chemistry A*, **114**, 1241.
18. A. B. Djuricic, Y. H. Leung, K. H. Tam, Y. F. Hsu, L. Ding, W. K. Ge, Y. C. Zhong, K. S. Wong, W. K. Chan, H. L. Tam, K. W. Cheah, W. M. Kwok, D. L. Phillips, *Nanotechnology* **2007**, *18*.
19. U. Ozgur, A. Teke, C. Liu, S. J. Cho, H. Morkoc, H. O. Everitt, *Applied Physics Letters* **2004**, *84*, 3223.
20. F. Williams, *Physica Status Solidi* **1968**, *25*, 493.
21. A. Janotti, C. G. Van de Walle, *Physical Review B* **2007**, *76*.
22. M. A. Reshchikov, R. Y. Korotkov, *Physical Review B* **2001**, *64*.
23. J. K. Song, U. Willer, J. M. Szarko, S. R. Leone, S. Li, Y. Zhao, *Journal of Physical Chemistry C* **2008**, *112*, 1679.
24. M. D. McCluskey, S. J. Jokela, *Journal of Applied Physics* **2009**, *106*.
25. L. Schmidt-Mende, J. L. MacManus-Driscoll, *Materials Today* **2007**, *10*, 40.
26. R. Guo, M. Matsumoto, T. Matsumoto, M. Higashihata, D. Nakamura, T. Okada, *Applied Surface Science* **2009**, *255*, 9671.
27. N. E. Hsu, W. K. Hung, Y. F. Chen, *Journal of Applied Physics* **2004**, *96*, 4671.
28. S. F. Chichibu, T. Sota, G. Cantwell, D. B. Eason, C. W. Litton, *Journal of Applied Physics* **2003**, *93*, 756.
29. J. C. Johnson, K. P. Knutsen, H. Q. Yan, M. Law, Y. F. Zhang, P. D. Yang, R. J. Saykally, *Nano Letters* **2004**, *4*, 197.
30. S. A. Studenikin, M. Cocivera, *Journal of Applied Physics* **2002**, *91*, 5060.
31. K. Vanheusden, W. L. Warren, C. H. Seager, D. R. Tallant, J. A. Voigt, B. E. Gnade, *Journal of Applied Physics* **1996**, *79*, 7983.
32. Y. Li, G. W. Meng, L. D. Zhang, F. Phillipp, *Applied Physics Letters* **2000**, *76*, 2011.
33. B. X. Lin, Z. X. Fu, Y. B. Jia, *Applied Physics Letters* **2001**, *79*, 943.
34. X. L. Wu, G. G. Siu, C. L. Fu, H. C. Ong, *Applied Physics Letters* **2001**, *78*, 2285.



35. M. Liu, A. H. Kitai, P. Mascher, *Journal of Luminescence* **1992**, 54, 35.
36. S. C. Lyu, Y. Zhang, H. Ruh, H. J. Lee, H. W. Shim, E. K. Suh, C. J. Lee, *Chemical Physics Letters* **2002**, 363, 134.
37. H. J. Egelhaaf, D. Oelkrug, *Journal of Crystal Growth* **1996**, 161, 190.
38. C. Klingshirn, *Semiconductor Optics*, Third ed., Springer-Verlag, Berlin, **2007**.
39. H. Ando, H. Oohashi, H. Kanbe, *Journal of Applied Physics* **1991**, 70, 7024.
40. A. van Dijken, E. A. Meulenlamp, D. Vanmaekelbergh, A. Meijerink, *Journal of Luminescence* **2000**, 87-9, 454.

## **CHAPTER 5**

### **Characterization of Spatially Specific Carrier Behavior along a Single ZnO Rod**

## 5.1 Introduction

The past decade has seen intensive research efforts directed towards the synthesis and characterization of novel semiconductor materials for use in microscaled optoelectronic and photonic technologies.<sup>1-6</sup> Of the many systems that have been reported, ZnO ranks as one of the most studied, due in part to its wide band-gap ( $\sim 3.7$  eV) and strong exciton binding energy (60 meV), making it a likely candidate for novel technologies associated with solar energy conversion and light emitting diodes, for example.<sup>7-12</sup> Additionally, a variety of nanostructural shapes can be readily synthesized, including nanohelices, shells, tetrapods, nanowires and nanorods.<sup>13, 14</sup> In general, the fluorescence from each structure gives rise to a narrow UV emission band ( $\sim 390$  nm) which corresponds to carrier recombination from the band-edge, and a broad visible emission band arising due to carriers trapped in low energy defect states localized within the band-gap (Ref Figure 4.1) However, despite being composed of the same material, each shape is characterized by different photophysical properties.<sup>13, 15</sup> This suggests the underlying structure of the object gives rise to different dynamical properties.

While the differences between objects have been studied, there are relatively few reports<sup>16-18</sup> that characterize the photophysical differences that arise due to changes in the local shape of a single structure. This is probably due in part to the nanometer size of many structures which fall below the diffraction limit of light, thereby preventing excitation of spatially specific structural regions. While techniques such as near-field scanning optical microscopy (NSOM) have been utilized to study ZnO nanostructures,<sup>19</sup> they often utilize a one-photon excitation which lacks the resolution to characterize differences between contributions from the surface and interior of the structure. To more effectively characterize the dependence of carrier behavior on object shape, we utilize a two-photon microscope to analyze structures with length scales greater

than the instrument's optical resolution. Doing this enables us to accurately probe different regions within a single structure. Furthermore, two-photon excitation only occurs at the focal point of the objective, enabling us to study different regions in both the interior and surface of a structure.

The existence of intrinsic and extrinsic defects is ubiquitous among semiconductor crystals. They affect both the electronic and photophysical behavior of ZnO, but the precise mechanism by which this occurs remains unclear.<sup>20-22</sup> Here we present how changes in object shape can affect the ultrafast dynamics associated with carrier trapping and recombination. By studying ZnO rods annealed at different temperatures, we correlate changes in the trap emission spectra with the defect densities from specific regions of a single structure. The differences observed at each location are attributed to the tapered shape of the rods used in our study, giving rise to greater surface contributions at the ends of the structure. Collectively, our results characterize how changes in the local shape of an object shape can influence the electronic and photophysical behavior of a material.

## 5.2 Experimental

*Materials:* The synthetic procedure for the ZnO rods used in our experiments has been described in Chapter 2. Briefly, the rods are grown using a hydrothermal method, which involves heating a 0.05 M reaction solution of  $\text{Zn}(\text{NO}_3)_2$  and methenamine ( $(\text{CH}_2)_6\text{N}_4$ ) in a closed bomb. The resulting structures are bath sonicated in ethanol to disperse aggregates and drop-cast onto a microscope slide with an etched reference grid to identify structures before and after annealing. The sample is placed on a microscope scanning stage for analysis prior to annealing. Following this, the sample is removed and placed in an oven to anneal in air at either 350°C (600 K), 450°C (700 K), or 550°C (800 K).

*Two-Photon Microscopy:* Details of our experimental setup (Ref Figure 3.1) have also been described in Chapter 3. Briefly, two-photon excitation is achieved using a mode-locked Ti:Sapphire laser (Spectra Physics Tsunami) pumped by a 5 W frequency doubled continuous-wave diode laser (Spectra Physics Millennia). The system generates pulses that are 80 fs wide with a 76 MHz repetition rate. The tuning range is between 720-850 nm and the maximum output power is  $\sim 1$  W. Pulse dispersion is corrected by passing the beam through a prism compressor in a double pass configuration. The pulse energy entering the microscope is controlled using a variable attenuator constructed from a half wave-plate and polarizing cube. Following this, the beam is expanded by a factor of four to insure the input aperture of the objective is overfilled.

The microscope is a home-built system with  $\sim 350$  nm resolution that follows an inverted design. Light is directed into the objective (Olympus MSPlan 50x, NA 0.8) using a dichroic mirror (R:680-1000 nm, T:360-650 nm). The sample is then raster scanned across the focal point of the objective, and the resulting fluorescence is collected back through the objective and detected using a photomultiplier tube (PMT) operated in a single photon counting regime. Spectral filtering is achieved using a monochromator placed in front of the PMT. Spatially specific regions of the structure are identified by first collecting a fluorescence image to identify coordinates of interest. The sample region is then spectroscopically analyzed by orienting it over the objective focal point for a user-defined period of time. To conduct time-resolved experiments, the emission is directed into a time-correlated single photon counting instrument with  $\sim 100$  ps time resolution. We found that the static and time-dependent spectra were sensitive to the pulse energy indicating that ZnO photophysics are dependent on carrier concentrations at high excitation intensities. We therefore utilized an excitation regime that was determined to

yield a limiting value for the photoluminescence lifetime. This was typically less than 0.3 nJ/pulse.

### **5.3 Results and Discussion:**

The band-edge and trap emission images following two-photon excitation of typical a structure used in our experiments is shown in Figure 1. The images show areas of enhanced intensity at the ends of the rods, low intensity in the middle, and enhanced emission along the vertices of each facet. We attribute the enhanced emission at the vertices to light coupling into transverse optical cavity modes. We observe similar behavior in second harmonic images, where the effect was attributed predominantly to whispering gallery modes.<sup>16</sup> The area of low intensity in the middle of the structure may indicate the presence of a grain or twinning boundary. We observe this in ~60% of the structures that are analyzed, and its presence or lack there-of may be due to differences in the nature of the grain boundary that forms during crystal growth.

Enhanced emission intensity at the ends of the structure has also been observed by other groups who attribute it to light coupling into longitudinal optical cavity modes which gives rise to wave-guided emission. Analysis of the band-edge images collected from our structures using a CCD camera (Ref Figure 4.5) reveals that, while a portion of light is wave-guided, a majority of the collected emission emanates from the excitation region (Chapter 4). This suggests that wave-guiding is not the predominant mechanism in our structures, and given our experimental geometry, the enhanced emission at the ends of the rod is more likely due to the propensity of light to couple into the structure at the excitation region.

The fluorescence images in Figure 5.1 were collected by raster scanning the structure over the focal point of the objective. Once an image has been processed, it can serve as a map to

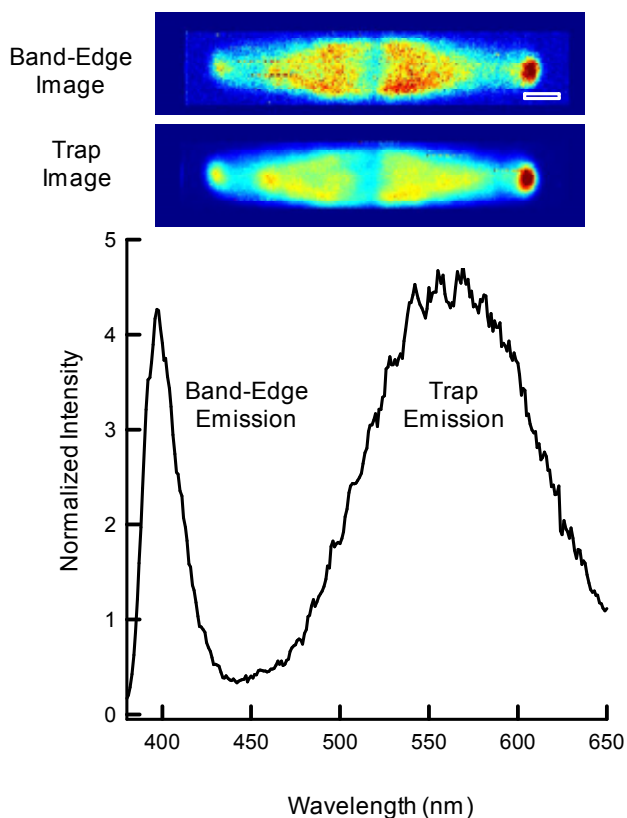


**Figure 5.1:** Examples of band-edge and trap emission images (scale bar 1  $\mu\text{m}$ ). The band-edge emission represent exciton or free carrier recombination between the valence and conduction bands. This correlates with the narrow band in the emission spectrum that is centered around 390 nm. The trap emission arises due to defects in the structure whose energy states are localized within the band-gap. The distribution of these state gives rise to a broad low energy band centered around 550 nm. Both images show areas of high intensity at the ends of the structure and low intensity in the middle. The emission patterns are discussed further in the text.

identify coordinates of interest for further analysis. Parking the objective between the end and middle of the structure in Figure 1 enabled us to collect the ZnO emission spectrum shown in the lower panel. The peak centered around 390 nm is attributed to carrier relaxation from the conduction band edge, and the broad lower energy peak arises due to defects in the crystal lattice. The relative intensities of the two peaks in the spectrum are suggestive of a high defect density in this region of the structure. The precise assignments for defects that give rise to this emission band are still largely controversial. In ZnO, intrinsic donors include oxygen vacancies and zinc interstitials, and acceptor defects have been assigned to zinc vacancies, oxygen interstitials and oxygen substituted in a zinc lattice site. Since no dopants were intentionally added to the reaction mixture, we presume this peak arises predominantly from these defect

types. It is also possible that extrinsic donors or acceptors, such as hydrogen and nitrogen impurities (respectively) arise in the lattice from components in the reaction mixture.

In a previous report we suggested that the static spectrum is a superposition of a high and low energy band (Chapter 4). Transitions between a hole-bound acceptor and electron in the conduction band were attributed to the high energy portion of the spectrum. The low energy portion was attributed to donor-acceptor pair (DAP) transitions, where a hole bound to an acceptor recombines with an electron bound to a shallow donor (Ref Figure 4.1). The purpose of the work described herein is to extend these observations by:

- 1) Comparing the behavior of carriers in the presence of a steadily decreasing trap state manifold. This is accomplished by studying the time-integrated spectra from samples annealed at different temperatures.
- 2) Analyzing the spectroscopic differences at spatially specific regions within a single structure following annealing.

We anticipate that the trap emission band will vary across different regions within a single structure due to the redistribution of defects as the annealing temperature is increased. This section is therefore split into three parts. Section 5.3.1 presents the effects of annealing at different temperatures on the time-integrated defect emission spectrum. Section 5.3.2 describes our observations on the corresponding time-dependent kinetics, and Section 5.3.3 reports the results of time-resolved and steady state measurements collected from different regions within a single structure.

#### *5.3.1 Effect of annealing temperature on the steady-state spectrum*

The scanning electron microscopy (SEM) image shown above the steady-state spectra in Figure 5.2 corresponds to a structure that has been annealed at 550°C. The image is



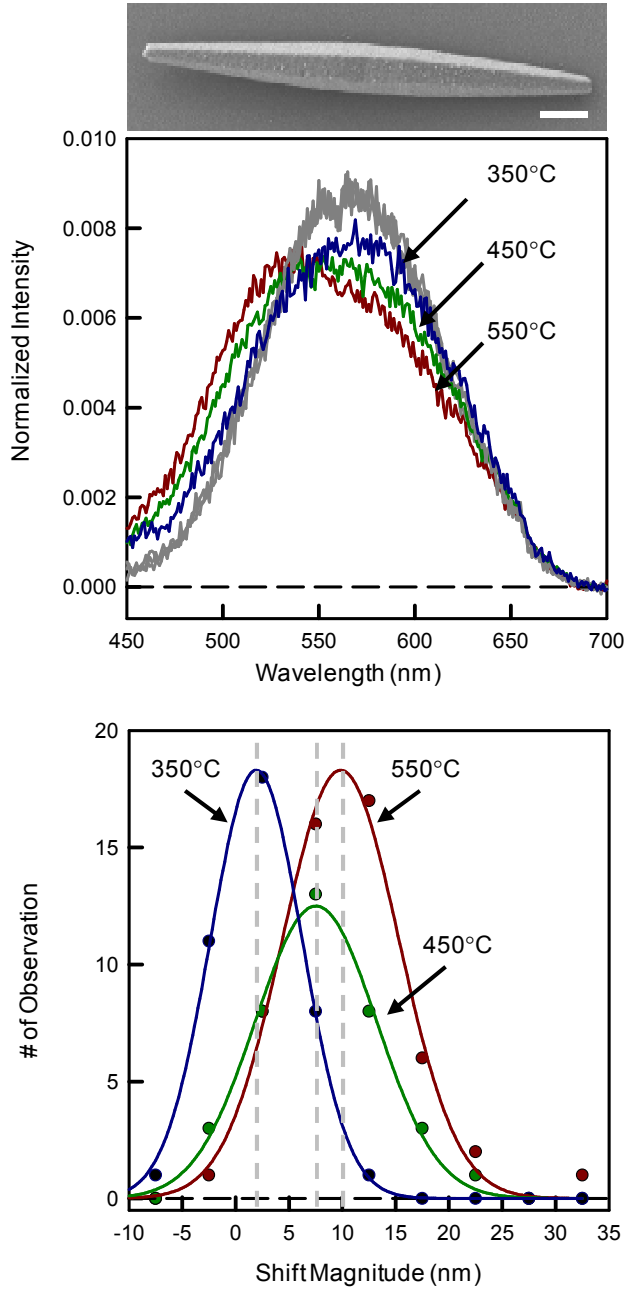


**Figure 5.2:** (*Top*) A scanning electron microscopy image of a rod annealed at 550°C. The rod is typical of the structures used in our experiments and shows no signs of thermal damage (Scale bar is 1  $\mu\text{m}$ ). The trap emission spectrum collected between the end and middle corresponds to the 550°C spectrum shown in the middle panel. (*Middle*) Comparison of time-integrated spectra collected before (grey) and after annealing. The spectra are normalized to their overall area to facilitate comparison. The remarkable agreement in the spectra before annealing indicates little variation in defect signatures between each rod. A gradual blue-shift is observed with increasing annealing temperature. The analysis was conducted on approximately 15 structures at three different locations, per annealing temperature. The magnitude of the blue-shift from each structure was determined by subtracting the spectral maximum following annealing, from the value before annealing. The distribution of results is shown in the bottom panel and indicates that the structures generally follow the same trend show in the spectra above.

representative of a typical structure used in our experiments, with an approximately 10  $\mu\text{m}$  length, and 1  $\mu\text{m}$  diameter in the center that tapers to 300 nm at the ends. Most importantly, the hexagonal crystalline structure does not appear to be affected by the highest temperature anneal (550°C), with clearly defined facets devoid of any surface damage (the particulate matter on the

surface is due to a thin layer of gold that is applied to the sample for SEM analysis). Similarly, no damage was observed in the structures annealed at 350 and 450°C.

The trap emission spectra following annealing at 350 (blue), 450 (green) and 550°C (red) are shown in the top panel of Figure 5.2, compared to the corresponding emission spectrum before annealing (grey). The spectra have been normalized to their overall area to facilitate their comparison. The 550°C spectrum was collected from the rod shown in the SEM image. The spectra were collected from the same position in the same structure (between the end and middle), before and after annealing. However, to ensure their integrity each rod was annealed at just one temperature, so that each spectrum represents a different structure. Despite being collected from different rods, there is remarkable agreement in the spectra collected before annealing (grey), indicating little variation in the types of defects across the samples we analyzed. As the annealing temperature is increased, the spectra gradually shift to higher energy, with an overall shift of ~12 nm at 550°C. The spectral blue-shift is in agreement with our previous observations, although the magnitude of the shift is lower (in Chapter 4 the shift ranged between 20-40nm). This discrepancy may be due to subtle changes in reaction environment or the degree of defect incorporation during crystal growth. Nevertheless, the appearance of the blue-shift is consistent with our assignment of the low energy band to DAP recombination. Shallow donors, such as zinc and hydrogen interstitials have low migration barriers and are highly mobile. Upon annealing, their density in the lattice would be steadily decreased with increasing annealing temperature. The result would be a depletion in the DAP concentration and a drastic reduction in the intensity of the low energy emission band, as observed in Figure 5.2.

To test if the gradual blue-shift is consistent over a larger population of structures, we repeated the procedure described above on three different positions from ~15 different rods at

each annealing temperature. The average wavelength ( $\lambda_{\text{avg}}$ ) of the normalized spectra, before ( $\lambda_b$ ) and after ( $\lambda_a$ ) annealing were then subtracted from each other ( $\lambda_b - \lambda_a$ ) to determine the magnitude of the shift. The distributions of the results at each temperature are shown in the lower panel of Figure 5.2. While the magnitude of the shift varies between each population, the majority tend to follow the same trend as the individual spectra shown in the top panel. At 550°C the magnitude of the shift is, on average, between 10 and 15 nm, at 450°C it is between 5 and 10 nm, and at 350°C it is between 0 and 5 nm. The distribution appears to be broader at 450°C, which may indicate a transition temperature where a certain type of defect becomes mobile, or has not been completely annealed from the structure.

These results are in contrast to observations reported by groups who observe a red shift in the defect spectrum following annealing in air at similar temperatures.<sup>15</sup> In their paper, Djurisić et al. studied the effect of annealing temperature on nanostructured shells, rods and needles. The effect of annealing varied between each structure, with no spectral difference in the shells and a large shift occurring in the nanorods. The large variation in the spectral characteristics suggest the observed effects are highly dependent on object shape. Additionally, there are two major differences between their experiment and ours.

First, the size of our structures is much larger, with length scales in the micron range, as opposed to the nanometer sized structures used in their experiment. Since two-photon excitation only occurs at the focal point of the objective, the majority of the emission we observe is arising from within our focal volume in the crystal interior, as opposed to the surface. Given the greater surface area of nanorods, the contributions from surface defects to the overall emission will be much greater and are indeed cited as giving rise to their observations.

Second, the spectral characteristics of the trap emission differ from the structures we analyze. While the growth of both spectra begins around 500 nm, their trap band extends beyond 700 nm, differing from ours which terminates around that wavelength. This indicates that the defect types in their samples are not present in our structures. It is therefore not surprising that the results we observe differ from Djurisić et al., and indeed, may not be directly comparable given the differences in trap signatures and structure dimensions.

Over 90% of the structures we analyzed had an increase in the band-edge to trap emission ratio (BE:T) following annealing. However, the overall difference in intensity between the two bands varied largely at each temperature, and in contrast to the spectral shift, we did not observe a BE:T dependence on temperature. This suggests that at the lowest annealing temperature there is already a drastic reduction in the defect density, despite no significant shift in the spectrum. Therefore, while a significant portion of defects have been annealed out of the structure, there is still sufficient density at 350°C to give rise to the low energy emission portion of the static spectrum.

There are significant differences in the literature over which defect types give rise to the trap emission, and the subject remains controversial.<sup>20, 23</sup> It is therefore difficult to assign the precise defect types that give rise to the observed effects of temperature on trap emission. As stated earlier, likely donor defects involved in the DAP transition include zinc and hydrogen interstitials, due to their high mobility and shallow energy levels. However, these defects only represent one component of the DAP transition. Of the different types of defects that have been attributed to the trap emission in ZnO, perhaps the two most commonly cited are Zn ( $V_{Zn}$ ) or O vacancies ( $V_O$ ).<sup>13, 20-22, 24</sup>

The  $V_O$  defect has been extensively studied in ZnO, but the collective reports on its role in trap emission remain inconclusive. Results obtained from a variety of experimental techniques, such as electron paramagnetic resonance and positron annihilation spectroscopy, attribute their observations to this defect.<sup>25-28</sup> Conversely, a recent study suggests that  $V_O$  are deep traps with transitions  $\sim 1$  eV below the conduction band, and are therefore unlikely to contribute to the emission.<sup>21</sup> Additionally, ZnO is intrinsically an n-type material, resulting in a high  $V_O$  formation energy, making its overall concentration in the lattice low.<sup>23</sup> There is however, growing consensus that recombination with  $V_{Zn}$  potentially gives rise to defect emission.<sup>21, 22, 29-31</sup> In this case, ZnO's n-type character facilitates  $V_{Zn}$  formation, and while values vary in the literature, a recent study reported that the calculated transition between the -1 and -2  $V_{Zn}$  charge state is  $\sim 0.9$  eV above the valence band.<sup>23</sup> Radiative recombination from either the conduction band or a shallow donor would therefore result in  $\sim 2.5$  eV (500 nm) photons, in agreement with the emission spectrum observed in our samples. To further probe the effects of different annealing temperatures on carrier dynamics, we followed the emission kinetics using time-correlated single-photon counting.

### *5.3.2 Effect of annealing temperature on the time-dependent kinetics*

A comparison of the emission decay transients collected from the same region in the same structure, before and after annealing at 450°C is shown in Figure 5.3. Each curve displays multi-exponential kinetics, but the lifetimes of each component differ considerably.

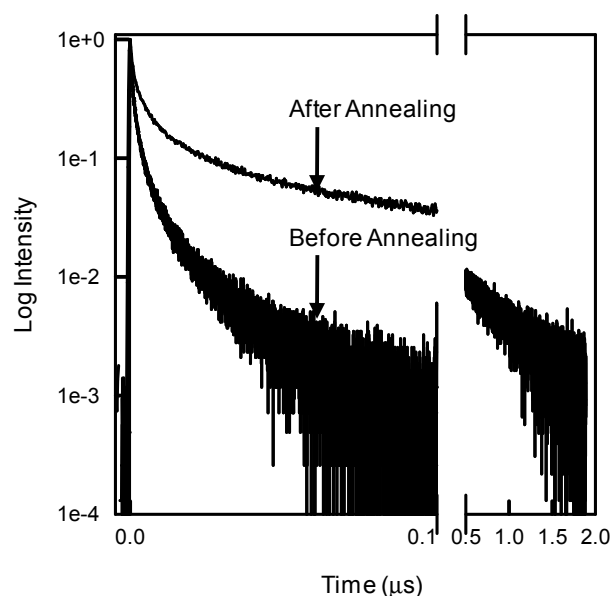


**Figure 5.3:** Emission (550 nm) decay kinetics before and after annealing at 450°C. Each transient displays multiexponential kinetics, but the lifetimes differ drastically. Before annealing, the emission decays to zero in 100 ns, after annealing, the decay lengthens to 2  $\mu$ s. This is attributed to increased trapping time following annealing as discussed further in the text.

Before annealing, the transient is characterized by time components ranging from sub-nanosecond ( $\sim 100$ -500 ps) to slower 1-10's of nanoseconds, decaying to zero in  $\sim 100$  ns. Following annealing, the lifetimes become much longer, with time components ranging from 1-10 ns to slower 10-100's of nanoseconds, decaying to zero in  $\sim 2$   $\mu$ s. These data are consistent with a reduction in the defect density following annealing. When the defect density is high trap recombination is facilitated by the greater proximity of DAPs, leading to faster decay kinetics. Annealing initializes defect migration and reduces the overall trap state density. Thus carriers remain trapped in defect states for a longer period of time before encountering an avenue for recombination. Additionally, with a reduction in defect density more carriers are able to migrate to the surface. In this region, an electron depletion layer exists due to bands bending upwards in n-type materials. Therefore, holes that become trapped on the surface must wait longer before encountering a corresponding electron to recombine with, which gives rise to longer emission lifetimes. These observations are consistent with a reduction in the low energy portion of the

static spectrum (Figure 5.2), giving rise to greater contributions from higher energy transitions following annealing.

We previously showed that before annealing, rods display an 8-10 nm red-shift in the time-dependent spectra (Figure 4.10). This was attributed to the differing distances between DAPs. The relationship between a DAP's spatial distance and transition energy ( $\Delta E$ ) can be described by:<sup>32</sup>

$$\Delta E = E_g - E_D - E_A + \frac{e^2}{(\epsilon d)} \quad (1)$$

where  $E_g$  is the band gap energy,  $E_D$  and  $E_A$  are the donor and acceptor energy respectively,  $\epsilon$  is the dielectric constant and  $d$  is the average distance between the donor and acceptor. This equation dictates an inverse relationship between the DAP energy ( $\Delta E$ ) and their spatial proximity ( $d$ ), and is therefore consistent with the assigned red-shift.

After annealing, the depletion of the DAP population means that contributions from the higher energy transitions (between the acceptor and conduction band) will dominate the overall emission. This gives rise to a blue-shift in the time-dependent spectrum (Figure 4.12). The precise mechanism for this behavior may arise due to several processes. It is possible that the high energy portion of the static spectrum is a superposition of two bands, due to transitions between the conduction band and two different acceptor types. In addition to  $V_{Zn}$ , one possible acceptor type could be nitrogen.<sup>22, 23</sup> This is an attractive candidate because it has been shown to give rise to high energy emission and is closest in atomic size to oxygen, so that its incorporation would result in minimal strain to the lattice. Our data would therefore be consistent with the low energy transition occurring first, followed by the higher energy transition. The blue-shift may also arise due to a band-gap renormalization initially created by photoexcited free carriers

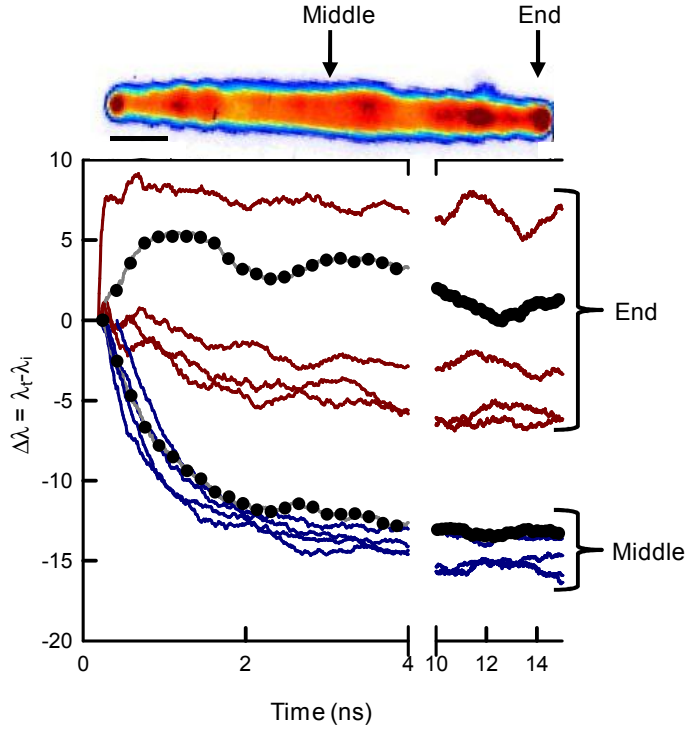


**Figure 5.4:** Time-dependent shift in the spectral maximum collected from the end and middle of five rods. The data corresponding to the rod shown above are displayed as grey lines with every 25<sup>th</sup> point marked in black. The scale bar corresponds to 1  $\mu\text{m}$ . The data shows that the blue-shift is greatest in the middle of the structure and least at the end. Interestingly we occasionally observe a rapid red-shift in the spectrum at the end of the structure. Mechanisms for this behavior are discussed in detail in the text.

As carriers begin to recombine the band-gap recovery gives rise to higher energy transitions and a blue-shift in the time-dependent spectrum. Additionally, with a lower defect density, carriers migrate to the surface. Here band-bending increases the energetic distance between the conduction band edge and acceptor state. Since electrons are depleted in this region, a radiative transition takes longer to occur (as described above) and will therefore also give rise to a time-dependent blue-shift. These processes are depicted in Figure 4.13. The different photophysical properties of various ZnO structures, suggests that the mechanisms we previously described could differ depending on the local shape of a single object. We therefore analyzed the time-dependent and steady state spectra from different structural regions.

### 5.3.3 Comparison of the photophysics from different structural regions

Since we observed a blue shift in the spectra from rods annealed at 450 and 550°C, we focused on these structures to analyze the differences between local structural regions. The magnitude of the spectral shift in the emission maximum ( $\Delta\lambda = \lambda_t - \lambda_i$ ) taken from the end, and



middle of five different rods annealed at 550°C, is displayed as a function of time in Figure 5.4. The trap emission image from one of the structures analyzed is shown above the graph, identifying the precise location that each dataset was collected from. In agreement with our previous observations in Chapter 4, there is a blue-shift in the time-dependent spectra at each region in the structure. However, the kinetics shows a clear dependence on location. Data obtained from the end of the structure generally only shifts by 3-5 nm, and occasionally we observe a rapid red-shift at early times (within the first 2 ns) followed by a steady, albeit small, shift to the blue. In contrast, the data obtained from the middle of the rod shifts between 10 and 15 nm to the blue in the first 2 ns after photoexcitation. While there is a clear difference between the dynamics at the end and middle of the structures, the magnitude of the shift in the interior is more variable, shifting between 5 and 20 nm, depending on the structure (data not shown). Since the end and middle clearly define different structural and photophysical properties, the interior represents a transition between these regions. The variation may therefore be due to this area being more sensitive to the position of the objective, displaying more of the properties from the location the objective is proximal to.

The blue-shift is consistent with our previous observations; however, the precise origin of the difference between the end and middle is currently unclear. Comparison of the static spectrum at these positions shows no differences, indicating that the DAP population has been equally affected by annealing. Since the blue-shift may be due in part to a reduction in free carrier density, it is possible that carriers are able to migrate out of the focal region faster in the middle of the structure, due to a greater volume of material. Carriers generated at the end are limited to migrating in one direction (towards the structure interior). This may significantly slow the band-gap recovery in this location. The reduced volume at the end of the structure may also

be giving rise to greater surface interactions that are less prevalent in the middle, complicating the dynamics. It is therefore possible that the rapid red-shift observed at the ends of some structures, may be due to non-radiative recombination of the hole with surface states. This would deplete the concentration of hole-bound acceptors at the surface, dampening the blue-shift created by band-bending, as described above.

The results from the steady-state measurements described in Section 4.1 led us to conclude that annealing at 450°C represented a transition temperature where certain defects either hadn't begun to migrate or hadn't been completely annealed from the structure. If this is true, we would expect to see a difference in the static spectrum depending on the local defect concentration at different regions in the structure. Shown in Figure 5.5 are spectra collected from a structure annealed at 450°C (*right*), and from one that wasn't (*left*). Each spectrum is from a different focal plane perpendicular to the rod  $c$ -axis, as depicted by the hexagonal cross-section above each graph. Before annealing, there is no difference between the spectra from each focal plane. However, following annealing there is ~30 nm blue-shift in the center of the structure relative to either surface.

These results suggest that the defects giving rise to the DAP emission migrate perpendicular to the  $c$ -axis of the rod, while the higher energy defects either do not migrate at this temperature, or do so isotropically (the latter being more likely as we observe an overall decrease in the trap emission intensity following annealing). There have been several experimental and theoretical descriptions of defect diffusion in ZnO, but there is still general disagreement in the literature.<sup>23, 33-37</sup> Several groups have suggested that  $V_{Zn}$  diffusion is

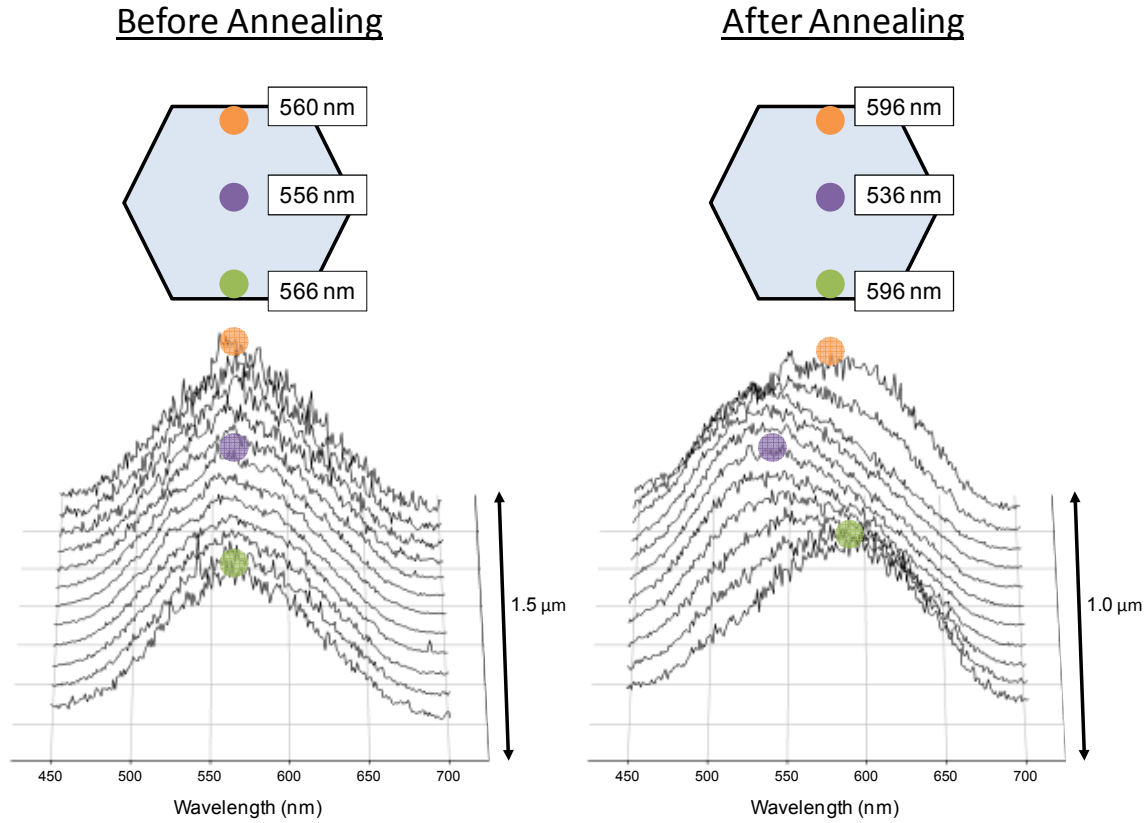


**Figure 5.5:** Comparison of the steady-state spectra collected from different focal planes between the interior and surface of a single structure. Data collected before annealing (*left*) shows no shift in the spectral maximum with position. However, the data after annealing at 450°C shows that the spectra in the interior is blue-shifted by ~30 nm, relative to either surface. Note that the data was taken from two separate structures.

isotropic.<sup>23</sup> Since we attribute the higher energy trap emission in our structures in part to  $V_{Zn}$  (as discussed above), our observations of a blue-shift in the center of the structure are consistent with these reports. Studies have also suggested that zinc interstitials migrate perpendicular to the rod axis following an interstitial migration mechanism (between lattice interstice).<sup>37</sup> It is therefore likely that donor defects giving rise to the DAP emission in our structures (such as zinc and hydrogen interstitials) follow a similar mechanism and propagate towards the surface.

Therefore, these results indicate that at 450°C the defects have not been completely annealed from the structure but have begun to migrate away from the rod interior. Experiments are currently being conducted to further elucidate the differences that exist between the bulk and surface of the crystal at different positions along the structure, as well as the dynamics at the rod surface.

#### **5.4 Conclusions:**

Monitoring the photophysical changes in single structures annealed at different temperatures enabled us to characterize the nature of the defects giving rise to the trap emission in ZnO. Comparison of the trap emission kinetics at different regions within a structure revealed markedly different behavior, with a rapid blue-shift in the middle of the rod compared to a slower change at the end that is smaller in magnitude. We propose that these differences are ultimately due to decreased material volume at the end of the structure, which hinders carrier migration and increases surface interactions. Our initial studies, comparing the structure surface with the bulk show that the static spectrum is red-shifted at the surface relative to the interior. This result is in agreement with several studies characterizing defect migration mechanisms in ZnO. Our results show that different regions in a single structure can have differing effects on the trapping dynamics of carriers and this is ultimately due to local object shape. Given the various nanostructure shapes currently described in the literature, the observations reported herein suggest that local regions within a single object can influence recombination dynamics and result in a spatial variation of carrier behavior across the structure.

## 5.5 References

1. D. J. Kim, J. H. Hyung, D. W. Seo, D. I. Suh, S. K. Lee, *Journal of Electronic Materials* **2010**, 39, 563.
2. M. Li, H. Y. Zhang, C. X. Guo, J. B. Xu, X. J. Fu, P. F. Chen, *Chinese Physics B* **2009**, 18, 5020.
3. J. J. Schneider, R. C. Hoffmann, J. Engstler, A. Klyszcz, E. Erdem, P. Jakes, R. A. Eichel, L. Pitta-Bauermann, J. Bill, *Chemistry of Materials* **2010**, 22, 2203.
4. X. S. Fang, Y. Bando, U. K. Gautam, T. Y. Zhai, H. B. Zeng, X. J. Xu, M. Y. Liao, D. Golberg, *Critical Reviews in Solid State and Materials Sciences* **2009**, 34, 190.
5. Y. F. Hu, Y. L. Chang, P. Fei, R. L. Snyder, Z. L. Wang, *Acs Nano* **2010**, 4, 1234.
6. M. Ohtsu, T. Kawazoe, T. Yatsui, M. Naruse, *Ieee Journal of Selected Topics in Quantum Electronics* **2008**, 14, 1404.
7. X. L. Guo, J. H. Choi, H. Tabata, T. Kawai, *Japanese Journal of Applied Physics Part 2-Letters* **2001**, 40, L177.
8. D. C. Look, B. Claftin, *Physica Status Solidi B-Basic Research* **2004**, 241, 624.
9. A. H. Macdonald, P. Schiffer, N. Samarth, *Nature Materials* **2005**, 4, 195.
10. J. B. Baxter, E. S. Aydil, *Applied Physics Letters* **2005**, 86.
11. W. J. E. Beek, M. M. Wienk, R. A. J. Janssen, *Advanced Materials* **2004**, 16, 1009.
12. M. Law, D. J. Sirbuly, J. C. Johnson, J. Goldberger, R. J. Saykally, P. D. Yang, *Science* **2004**, 305, 1269.
13. A. B. Djuriscic, Y. H. Leung, *Small* **2006**, 2, 944.
14. Z. L. Wang, *Journal of Physics-Condensed Matter* **2004**, 16, R829.
15. A. B. Djuriscic, Y. H. Leung, K. H. Tam, Y. F. Hsu, L. Ding, W. K. Ge, Y. C. Zhong, K. S. Wong, W. K. Chan, H. L. Tam, K. W. Cheah, W. M. Kwok, D. L. Phillips, *Nanotechnology* **2007**, 18.
16. B. P. Mehl, R. L. House, A. Uppal, A. J. Reams, C. Zhang, J. R. Kirschbrown, J. M. Papanikolas, *Journal of Physical Chemistry A* **2010**, 114, 1241.
17. Y. M. Oh, K. M. Lee, K. H. Park, Y. Kim, Y. H. Ahn, J. Y. Park, S. Lee, *Nano Letters* **2007**, 7, 3681.

18. Y. H. Yang, X. Y. Chen, Y. Feng, G. W. Yang, *Nano Letters* **2007**, 7, 3879.
19. J. C. Johnson, H. Q. Yan, R. D. Schaller, P. B. Petersen, P. D. Yang, R. J. Saykally, *Nano Letters* **2002**, 2, 279.
20. L. Schmidt-Mende, J. L. MacManus-Driscoll, *Materials Today* **2007**, 10, 40.
21. A. Janotti, C. G. Van de Walle, *Reports on Progress in Physics* **2009**, 72.
22. M. D. McCluskey, S. J. Jokela, *Journal of Applied Physics* **2009**, 106.
23. A. Janotti, C. G. Van de Walle, *Physical Review B* **2007**, 76.
24. U. Ozgur, Y. I. Alivov, C. Liu, A. Teke, M. A. Reshchikov, S. Dogan, V. Avrutin, S. J. Cho, H. Morkoc, *Journal of Applied Physics* **2005**, 98.
25. L. S. Vlasenko, G. D. Watkins, *Physical Review B* **2005**, 71.
26. F. Tuomisto, K. Saarinen, D. C. Look, G. C. Farlow, *Physical Review B* **2005**, 72.
27. F. H. Leiter, H. R. Alves, A. Hofstaetter, D. M. Hofmann, B. K. Meyer, *Physica Status Solidi B-Basic Research* **2001**, 226, R4.
28. D. M. Hofmann, D. Pfisterer, J. Sann, B. K. Meyer, R. Tena-Zaera, V. Munoz-Sanjose, T. Frank, G. Pensl, *Applied Physics a-Materials Science & Processing* **2007**, 88, 147.
29. F. Tuomisto, V. Ranki, K. Saarinen, D. C. Look, *Physical Review Letters* **2003**, 91.
30. F. Tuomisto, K. Saarinen, D. C. Look, *Physica Status Solidi a-Applications and Materials Science* **2004**, 201, 2219.
31. S. M. Evans, N. C. Giles, L. E. Halliburton, L. A. Kappers, *Journal of Applied Physics* **2008**, 103.
32. F. Williams, *Physica Status Solidi* **1968**, 25, 493.
33. B. K. Meyer, H. Alves, D. M. Hofmann, W. Kriegseis, D. Forster, F. Bertram, J. Christen, A. Hoffmann, M. Strassburg, M. Dworzak, U. Haboeck, A. V. Rodina, *Physica Status Solidi B-Basic Research* **2004**, 241, 231.
34. G. W. Tomlins, J. L. Routbort, T. O. Mason, *Journal of Applied Physics* **2000**, 87, 117.
35. R. Schaub, E. Wahlstrom, A. Ronnau, E. Laegsgaard, I. Stensgaard, F. Besenbacher, *Science* **2003**, 299, 377.

36. M. A. N. Nogueira, A. C. S. Sabioni, W. B. Ferraz, in *Diffusion in Materials: Dimat 2004, Pt 1 and 2, Vol. 237-240* (Eds.: M. Danielewski, R. Filipek, R. Kozubs, W. Kucza, P. Zieba, Z. Zurek), **2005**, pp. 163.
37. G. Y. Huang, C. Y. Wang, J. T. Wang, *Solid State Communications* **2009**, 149, 199.

## **CHAPTER 6**

### **Spatially Specific Electron-Hole Plasma Formation in a Single ZnO Rod**



## 6.1. Introduction

The technological importance of ZnO for novel optoelectronic and photonic devices at the nanoscale is due to many of its intrinsic properties. In addition to a large band-gap (3.4 eV) and strong exciton binding energy (60 meV), ZnO is particularly attractive because of the ease by which many different nanocrystal shapes can be synthesized. Unlike any other semiconductor, the variety of shapes range from, nanorods, wires, shells, helices, spheres and tetrapods, to name a few.<sup>1-3</sup> Each shape gives rise to different physical and photophysical properties, and the technological potential of some of these structures has already been realized.<sup>4-19</sup>

Understanding the differences between various structural shapes requires analyzing each object individually. There are several reports in the literature that have accomplished this,<sup>20-22</sup> and while the differences between single objects is generally understood, there remain relatively few studies<sup>22-25</sup> that characterize how the changing shape along a single structure can affect its dynamic and electronic properties. This is important, because the few studies that do exist show they can be greatly affected.

Several groups have shown that ZnO nanostructures can form optical cavities that enhance stimulated emission.<sup>26-30</sup> This is due to increasing collisions between excitons, resulting in the dissociation of the electron-hole pairs and the eventual formation of an electron-hole plasma.<sup>31</sup> Here we show that this mechanism is highly dependent on the local shape of the object in the vicinity of the excitation.

## 6.2 Experimental

Structures were synthesized using a hydrothermal technique with a 1:1 molar ratio of  $\text{Zn}(\text{NO}_3)_2$  and hexamine ( $(\text{CH}_2)_6\text{N}_4$ ), the details of which have been described elsewhere.<sup>22</sup>

Samples are prepared for microscopic analysis by drop casting a suspension of ZnO rods in ethanol, onto a glass microscope slide. The experiment is conducted at room temperature without the use of a coverslip.

Single structure analysis is conducted using a home-built two-photon microscope. Excitation is achieved using a mode-locked Ti:Sapphire laser (Spectra Physics Tsunami) pumped by a 5 W frequency doubled continuous-wave diode laser (Spectra Physics Millennia). The system produces pulses with an 80 fs width at a 76 MHz repetition rate. The repetition rate can be varied by sending the output through an acousto-optic crystal operated in a single pass configuration. Light generated by the laser system can be tuned between 720-850 nm with a maximum output of  $\sim 1$  W at 800 nm. The excitation intensity incident on the sample can be adjusted between 0 and 1 nJ/pulse using a variable attenuator consisting of a half wave-plate and polarizing cube. The pulse energies used in these experiments varied between 0.3 and 0.8 nJ/pulse.

Light is directed into the objective (Olympus MSPlan 50x, NA 0.8) using a dichroic mirror (R:680-1000 nm, T: 360-650 nm) and is focused to an approximately 350 nm spot. The sample is raster-scanned across the focal point of the objective with a piezoelectric x-y translation stage (Queensgate NPS 3330 Controller/Stage System) with  $< 20$  nm resolution. Fluorescence from the sample is collected back through the objective and transmitted through the dichroic mirror. The emission can either be directed to a monochromator and detected by a photomultiplier tube, or to a nitrogen-cooled CCD camera (Princeton Instruments) for spectral measurements. Imaging is also conducted with a standard CCD camera (Basler Scout).

### 6.3 Results and Discussion

An example of the ZnO emission spectrum following a two-photon excitation (730 nm) of the rods utilized in this study is shown in the top panel of Figure 6.1. The spectrum consists of two emission bands, one narrow peak centered  $\sim 390$  nm that corresponds to exciton or electron/hole recombination from the band-edge (BE), and a broad low energy peak centered  $\sim 550$  nm that arises from defects in the crystal lattice that create localized trap states (T). An example of the emission profiles across a single structure is shown above the spectrum, with the corresponding scanning electron microscopy image. The rod is typical of the size and shape of the ZnO structures used in this study, displaying a needle-like morphology with a single-crystalline hexagonal cross-section. Structures generally vary between 10-20  $\mu\text{m}$  in length with 1-2  $\mu\text{m}$  diameter in the middle and 300-500 nm at the ends.

The periodic intensity pattern in the images arises due to light coupling into different optical cavity modes. We have observed similar behavior in second-harmonic images<sup>22</sup> where it was attributed to Fabry-Perot modes between the parallel facets, and whispering gallery modes due to total-internal reflection off each of the six facets (Ref Figure 4.4). Light coupling into the Fabry-Perot modes give rise to the single spots observed as the structure begins to taper, while the whispering gallery modes are observed as light emanating from the facet vertices in the center of the structure. The emission images also show increased areas of intensity at the ends of the structure. This due to a greater propensity for light to couple into the cavity at this particular region (Chapter 4).

A similar enhancement of the BE emission at the ends of nanowires has been reported by van Vugt et al., and attributed to greater excitation probabilities in this region, due to

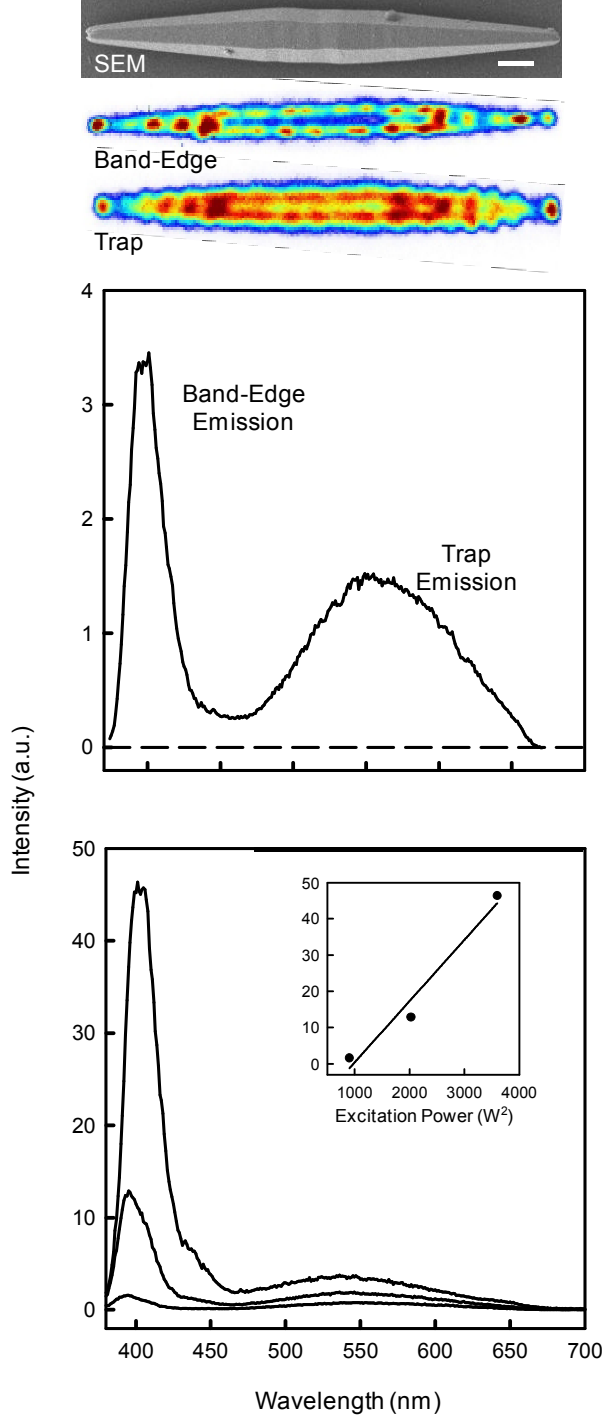


**Figure 6.1:** (Top) Band-edge (BE) and trap (T) emission images of the rod shown in the scanning electron microscopy image (Scale bar corresponds to 1  $\mu\text{m}$ ). The images show areas of enhanced intensity at the end of the structure and along the facet vertices. This behavior has been attributed to coupling into various transverse and longitudinal optical modes. (Middle) ZnO emission spectrum taken from the interior of the structure shown above. The narrow peak centered around 390 nm corresponds to BE emission, and the broad peak in the visible region is due to trap states that arise from lattice defects. (Bottom) ZnO emission spectrum collected at increasing excitation intensities. The BE emission broadens and shifts to lower energies with an increase in the BE:T emission ratio. The inset shows that this relation is linear with the square of the excitation power. Here the excitation is squared to account for the quadratic dependence of emission on two-photon excitation intensity.

polariton modes,<sup>25</sup> which arise from the strong coupling of excitons with optical cavity modes.<sup>25, 31</sup> In their experiment, the enhanced emission intensity decreased with increasing excitation intensity, which was attributed to exciton dissociation, either through local heating,

Coulombic screening or exciton-exciton scattering. This confirmed that the enhanced intensity was due to the strong coupling of the exciton dipoles with optical cavity modes. The spectral dependence of the emission with increasing laser power taken from a typical structure used in our experiments is shown on the bottom panel of Figure 6.1. Since we observe an increase in emission with excitation intensity, our results are not consistent with their mechanism, confirming our assignment of a greater propensity for light (not excitons) to couple into optical cavity modes at the ends of the structure.

The spectra in the bottom panel of Figure 6.1 shows that the increase in the BE emission intensity is correlated with a spectral red-shift. The inset also shows that the BE emission scales quadratically with the square of the average laser power (the laser power is squared to account for the quadratic dependence of emission intensity on two-photon excitation), but the trap emission scales linearly. The linearity in the trap emission indicates spontaneous emission, and the non-linearity in the BE, may be stimulated emission.

Previously we reported observing differences in the static and time-dependent spectral signatures between different regions in a single structure (Chapter 4).<sup>22</sup> These observations led us to analyze if there is a dependence on EHP formation with local object shape. To answer this question we positioned the objective over specific regions within a single structure and collected the excitation dependent emission spectra from each individual region. An example of the results of our analysis from the end, interior (i.e. between the end and middle) and middle of a needle-shaped rod is shown in Figure 6.2. The spectra are normalized to their maximum intensity to highlight the shift, and display ~16 nm red-shift with increasing power at the end of the structure, ~10 nm shift in the interior, and ~2 nm shift

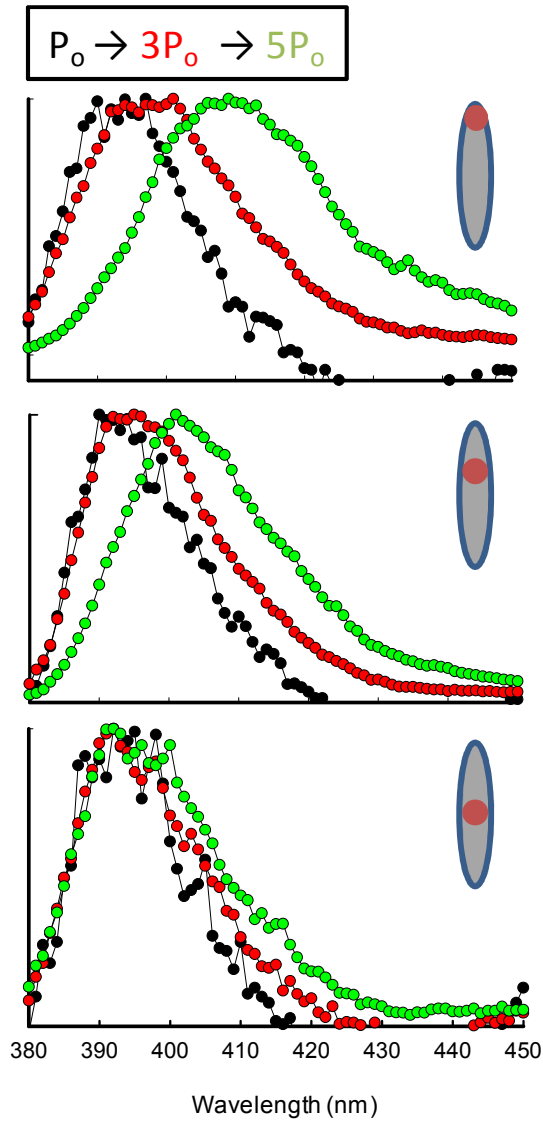


**Figure 6.2:** Spectra collected from the end, interior and middle of a single structure, as indicated by the schematic juxtaposed with each graph. Spectra were collected at increasing excitation power (here  $P_0$  corresponds to 5 mW average power). The shift is largest at the end of the structure ( $\sim 16$  nm) with only a minor shift in the middle ( $\sim 2$  nm). This is attributed to the smaller dimensions at the end of the structure, as well as a greater propensity for light to couple into optical cavity modes in that region.

in the middle. We have analyzed an additional 9 structures, and consistently observe this behavior, although the magnitude of the shift generally ranges between 5-20 nm at the end of the structure, between 3-10 nm at the interior and between 0-5 nm in the middle. The magnitude of the red-shift reported by different groups in the literature also vary, with larger shifts in agreement with our observations at the end of the structure<sup>29, 30, 32</sup> and smaller shifts in agreement with the middle.<sup>28</sup>

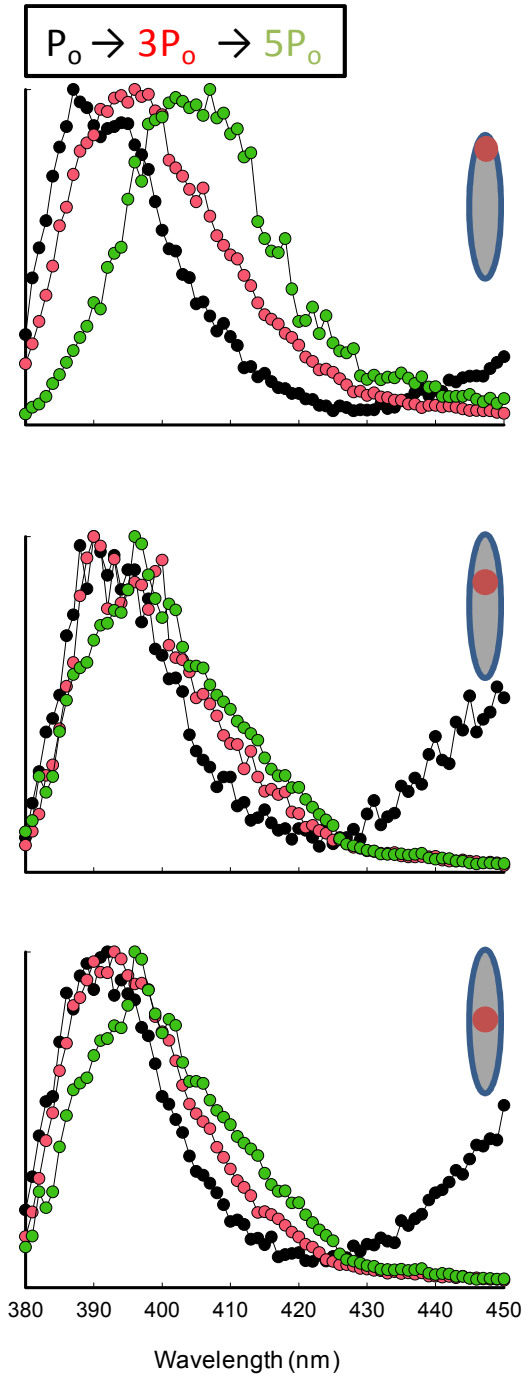


**Figure 6.3:** A similar experiment to Figure 6.2 conducted at a 7.6 MHz repetition rate (here  $P_0$  corresponds to 2 mW average power). We observe similar behavior to that shown in Figure 6.2. The shift is largest at the end of the structure ( $\sim 14$  nm) with only a minor shift in the middle ( $\sim 2$  nm). This is agreement with the formation of an electron hole plasma and shows the shift in our structures is not due to local heating effects.

Our observations can be explained as follows: Since there is a gradual convergence from the middle to both ends, the volume of material at the end of the structure is generally much smaller than the middle (Figure 6.1). This limits the number of paths carriers can take

to diffuse out of the focal volume, thereby increasing the density of free carriers and facilitating the formation of an EHP in this region. In contrast, the greater material in the middle enables carriers to access more avenues for diffusion. The large range in the magnitude of the shift observed at the end of different rods is therefore probably due to variation in the structural dimensions that occur in this region.

There have been several studies that observe a similar red-shift in the BE emission band, but attribute to local heating effects. In particular, a recent study conducted by Voss et al.<sup>33</sup> measured the change in the BE emission spectrum as a function of time, under constant illumination. They observed a red-shift in the BE spectrum that evolved over 27 s. This was attributed to local heating of the structure caused by multiphoton absorptions deep within the conduction band that generate excess kinetic energy carried by LO phonons.<sup>33</sup> The heat increases the refractive index of the material and leads to a red-shifted spectrum. Indeed, there are reports that suggest the heat generated within a single structure can be determined as a function of the shift in the BE emission spectrum.<sup>34, 35</sup>

Given that we observe the greatest red-shift at the end of the structure, where the lateral heat conductivity in the rod would be limited to one direction, we performed two experiments to insure that our observations were not simply due to local heating. First, if the effect we observe is due to local heating, the spectral shift should correlate with average laser power, whereas a carrier density effect (e.g. EHP) should scale with excitation intensity. We therefore repeated the experiment above using a laser repetition rate that had been reduced by an order of magnitude (76 MHz  $\rightarrow$  7.6 MHz). In this configuration, the pulse energy is the same, but the average power is reduced. The results shown in Figure 6.3 are identical to our observations at 76 MHz (Figure 6.2), consistent with an intensity dependent effect. Second,



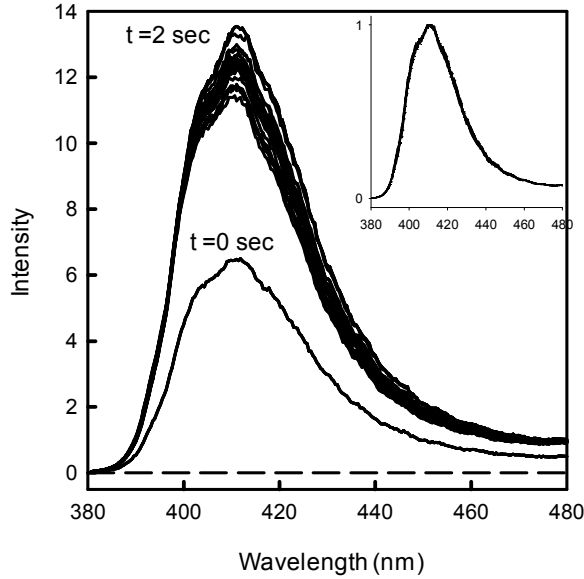


**Figure 6.4:** Time-resolved spectra collected with a nitrogen-cooled CCD camera with 100 ms resolution. We observe no shift in the emission band with time (corroborated by the normalized spectra in the inset). This indicates that the shift occurs within the first 100 ms, consistent with EHP formation and in stark contrast to reports that attribute the red-shift to local heating effects.

we employed a fast-shuttered nitrogen cooled CCD camera to measure the time-dependent evolution of the spectrum with 100 ms resolution. The results shown in Figure 6.4, confirm that the red-shift in the spectrum occurs faster than 100 ms, in stark contrast to the 27 s evolution reported by Voss et al., and is therefore consistent with the formation of an EHP.

Experiments conducted by others have shown that lasing can be achieved in ZnO structures under high excitation intensities,<sup>26-28, 36-39</sup> due in part, to light coupling into longitudinal optical cavity modes.<sup>25, 26</sup> To directly visualize the coupling efficiency of emission at the end of the structure, we collected emission images of rods excited in different regions using a CCD camera (Basler Scout). The results are shown in Figure 6.5. The brightest spot in each image corresponds to fluorescence from the two-photon excitation volume. Also apparent are areas of enhanced intensity at the ends of the structure. Previously we observed wave-guiding of BE emission between two rods in close proximity at one end (Figure 4.5). Since the highest excitation intensity of the rod shown in Figure 6.5 is sufficient to form an EHP, the light observed at the ends may be due to spontaneous emission coupling

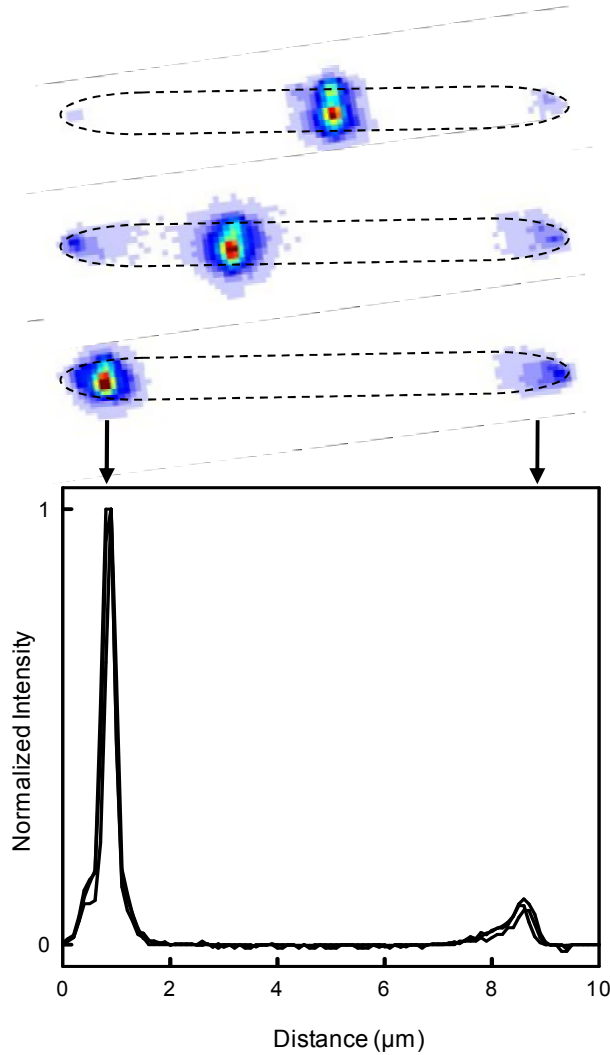


**Figure 6.5:** Band-edge emission images collected using a CCD camera. The bright spot in each image represents fluorescence emanating from the focal volume. Apparent in each image are regions of enhanced intensity at the ends of the structure. A longitudinal cross-section from the rod following increasing excitation is shown in the graph (the plots are normalized to the maximum intensity). We do not observe an increase in the emission from the end opposite to the excitation which suggests we are observing spontaneous and not stimulated EHP emission.

into optical wave-guiding modes or to stimulated emission. To test which mechanism is responsible, we plotted a cross section of the normalized intensity along the rod's optical axis, with increasing excitation power (Figure 6.5 *bottom*). If the dominating mechanism is stimulated emission along the longitudinal axis, the intensity at the opposing end should increase with excitation power, but we observe no change. This suggests that light observed at each end is not due to stimulated emission. Given the experimental geometry of our setup (Figure 3.1 & 3.2), it is more probable that light is coupling into transverse optical modes and stimulating emission perpendicular to the longitudinal axis. This would be consistent with the

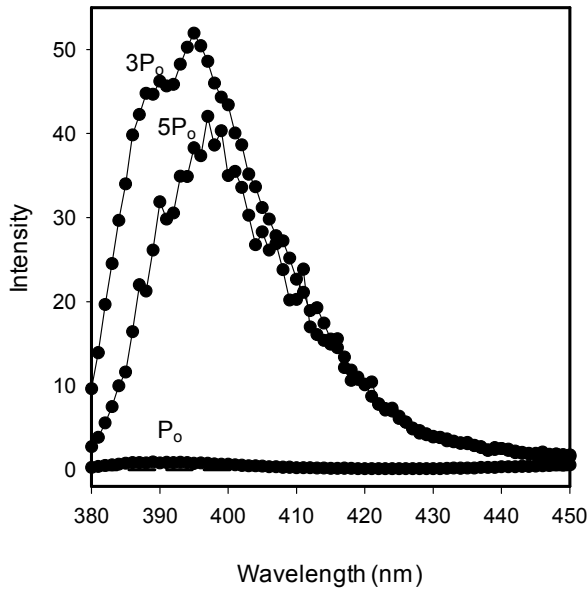


**Figure 6.6:** Power-dependent BE emission spectra collected at a 7.6 MHz repetition rate (here  $P_0$  corresponds to 2 mW). The spectrum decreases at the highest intensity, correlated with increased band broadening and BE:T emission ratio. The decreased emission may be due to stimulated emission propagating along the longitudinal axis. Given our experimental geometry, this would direct light away from the objective and not be detected by our system, consistent with the observed decrease.

broadening and red-shift of the emission band, as well as the quadratic growth in emission intensity with increasing excitation intensity.

Additionally, in  $\sim 30\%$  of the structures we analyze spectroscopically, there is a *decrease* in the BE emission intensity at the end of the structure using the highest excitation power (Figure 6.6). This is also correlated with an *increase* in the width of the band and the BE:T emission ratio, which is consistent with stimulated emission as described above. However, the decreased intensity may be due to stimulated emission propagating along the longitudinal axis of the structure. Given our experimental geometry, light propagating in this direction would be directed away from the objective and result in an overall decrease of the BE emission detected by our system. We also observe increased structure in the spectrum which may indicate stimulated emission due to exciton-exciton collisions.<sup>25, 29</sup> If this were true however, the peaks would be spaced periodically, and while this possibility cannot be ruled out, the spectra shown in Figure 6.6 lack the resolution to definitively make this

assignment. The precise reason why we observe this in only a few rods is currently unclear, and may be due to the differences in end size between different structures.

#### **6.4 Conclusion**

The dependence of ZnO emission on excitation intensity is characterized by a red-shift in the band-edge emission spectrum and an increase in the BE:T ratio. This has been attributed to collisions between excitons existing in a high density that eventually leads to the formation of an EHP. While this observation has been described by several groups, to our knowledge, this is the first report that details the dependence of EHP formation on local object shape. Our results suggest that this process is more efficient at the end of the structure than the middle, due to a greater propensity of light to couple into optical cavity modes and the decreased volume in this region. While we generally do not observe stimulated emission in the results reported here, data from a few of the analyzed structures suggest this is possible.

## 6.5 References

1. A. B. Djuricic, Y. H. Leung, *Small* **2006**, 2, 944.
2. Z. L. Wang, *Journal of Physics-Condensed Matter* **2004**, 16, R829.
3. U. Ozgur, Y. I. Alivov, C. Liu, A. Teke, M. A. Reshchikov, S. Dogan, V. Avrutin, S. J. Cho, H. Morkoc, *Journal of Applied Physics* **2005**, 98.
4. L. Schmidt-Mende, J. L. MacManus-Driscoll, *Materials Today* **2007**, 10, 40.
5. J. B. Baxter, E. S. Aydil, *Applied Physics Letters* **2005**, 86.
6. W. J. E. Beek, M. M. Wienk, R. A. J. Janssen, *Advanced Materials* **2004**, 16, 1009.
7. X. L. Guo, J. H. Choi, H. Tabata, T. Kawai, *Japanese Journal of Applied Physics Part 2-Letters* **2001**, 40, L177.
8. Y. F. Hu, Y. L. Chang, P. Fei, R. L. Snyder, Z. L. Wang, *Acs Nano*, 4, 1234.
9. D. J. Kim, J. H. Hyung, D. W. Seo, D. I. Suh, S. K. Lee, *Journal of Electronic Materials*, 39, 563.
10. M. Law, L. E. Greene, J. C. Johnson, R. Saykally, P. D. Yang, *Nature Materials* **2005**, 4, 455.
11. D. C. Look, *Materials Science and Engineering B-Solid State Materials for Advanced Technology* **2001**, 80, 383.
12. D. C. Look, B. Claftin, *Physica Status Solidi B-Basic Research* **2004**, 241, 624.
13. M. Ohtsu, T. Kawazoe, T. Yatsui, M. Naruse, *Ieee Journal of Selected Topics in Quantum Electronics* **2008**, 14, 1404.
14. J. J. Schneider, R. C. Hoffmann, J. Engstler, A. Klyszcz, E. Erdem, P. Jakes, R. A. Eichel, L. Pitta-Bauermann, J. Bill, *Chemistry of Materials*, 22, 2203.
15. H. T. Ng, J. Han, T. Yamada, P. Nguyen, Y. P. Chen, M. Meyyappan, *Nano Letters* **2004**, 4, 1247.
16. W. I. Park, J. S. Kim, G. C. Yi, M. H. Bae, H. J. Lee, *Applied Physics Letters* **2004**, 85, 5052.
17. Y. F. Chen, D. Bagnall, T. F. Yao, *Materials Science and Engineering B-Solid State Materials for Advanced Technology* **2000**, 75, 190.

18. S. M. Al-Hilli, M. Willander, A. Ost, P. Stralfors, *Journal of Applied Physics* **2007**, *102*.
19. M. Grundmann, H. Frenzel, A. Lajn, M. Lorenz, F. Schein, H. von Wenckstern, *Physica Status Solidi a-Applications and Materials Science*, *207*, 1437.
20. A. B. Djuriscic, Y. H. Leung, K. H. Tam, Y. F. Hsu, L. Ding, W. K. Ge, Y. C. Zhong, K. S. Wong, W. K. Chan, H. L. Tam, K. W. Cheah, W. M. Kwok, D. L. Phillips, *Nanotechnology* **2007**, *18*.
21. J. C. Johnson, H. Q. Yan, R. D. Schaller, P. B. Petersen, P. D. Yang, R. J. Saykally, *Nano Letters* **2002**, *2*, 279.
22. B. P. Mehl, R. L. House, A. Uppal, A. J. Reams, C. Zhang, J. R. Kirschbrown, J. M. Papanikolas, *Journal of Physical Chemistry A*, *114*, 1241.
23. Y. M. Oh, K. M. Lee, K. H. Park, Y. Kim, Y. H. Ahn, J. Y. Park, S. Lee, *Nano Letters* **2007**, *7*, 3681.
24. Y. H. Yang, X. Y. Chen, Y. Feng, G. W. Yang, *Nano Letters* **2007**, *7*, 3879.
25. L. K. van Vugt, S. Ruhle, P. Ravindran, H. C. Gerritsen, L. Kuipers, D. Vanmaekelbergh, *Physical Review Letters* **2006**, *97*.
26. J. C. Johnson, H. Q. Yan, P. D. Yang, R. J. Saykally, *Journal of Physical Chemistry B* **2003**, *107*, 8816.
27. J. K. Song, U. Willer, J. M. Szarko, S. R. Leone, S. Li, Y. Zhao, *Journal of Physical Chemistry C* **2008**, *112*, 1679.
28. Y. H. Leung, W. M. Kwok, A. B. Djuriscic, D. L. Phillips, W. K. Chan, *Nanotechnology* **2005**, *16*, 579.
29. J. Takeda, S. Kurita, Y. F. Chen, T. F. Yao, *International Journal of Modern Physics B* **2001**, *15*, 3669.
30. P. Zu, Z. K. Tang, G. K. L. Wong, M. Kawasaki, A. Ohtomo, H. Koinuma, Y. Segawa, *Solid State Communications* **1997**, *103*, 459.
31. C. Klingshirn, *Semiconductor Optics*, Third ed., Springer-Verlag, Berlin, **2007**.
32. B. C. Cheng, X. M. Yu, H. J. Liu, M. Fang, L. D. Zhang, *Journal of Applied Physics* **2009**, *105*.
33. T. Voss, I. Kudyk, L. Wischmeier, J. Gutowski, *Physica Status Solidi B-Basic Solid State Physics* **2009**, *246*, 311.

34. C. Klingshirn, R. Hauschild, H. Priller, M. Decker, J. Zeller, H. Kalt, *Superlattices and Microstructures* **2005**, 38, 209.
35. R. Hauschild, H. Lange, H. Priller, C. Klingshirn, R. Kling, A. Waag, H. J. Fan, M. Zacharias, H. Kalt, *Physica Status Solidi B-Basic Solid State Physics* **2006**, 243, 853.
36. J. Dai, C. X. Xu, P. Wu, J. Y. Guo, Z. H. Li, Z. L. Shi, *Applied Physics Letters*, 97.
37. D. J. Gargas, M. C. Moore, A. Ni, S. W. Chang, Z. Y. Zhang, S. L. Chuang, P. D. Yang, *Acs Nano*, 4, 3270.
38. H. Kalt, J. Fallert, R. J. B. Dietz, J. Sartor, D. Schneider, C. Klingshirn, *Physica Status Solidi B-Basic Solid State Physics*, 247, 1448.
39. A. Stassinopoulos, R. N. Das, S. H. Anastasiadis, E. P. Giannelis, D. Anglos, *Journal of Optics*, 12.

## **CHAPTER 7**

### **Conclusion**



Trap states, which arise from defects in a crystal lattice, are an intrinsic property of every semiconductor material. Their presence and overall composition can have large effects on a material's properties and role in device design. Therefore, understanding defects will be central to a material's implementation in novel technologies. This observation is well recognized in the scientific community and has resulted in a flurry of research, yet much controversy still remains on the subject of defects. This is due in part to different synthetic methods and the inherent complexity of nanocrystalline systems. For example, variation in the size and shape of particles in a nanostructure population can give rise to different behaviors between each structure. This observation is well established. It therefore seems equally plausible that differences in the size and shape of a single structure can also give rise to different properties. The question thus arises: Can similar heterogeneous behaviors be observed at spatially distinct locations in a single object? This question is the overriding theme in this dissertation and we show that intra-object heterogeneity does exist. This is accomplished through the methodical exploration of the trap emission signatures in ZnO (Chapter 4) and their differences between regions within a single structure (Chapter 5), as well as the influence of shape in the formation of an electron-hole plasma (Chapter 6).

While many different semiconducting materials have recently been developed and characterized, perhaps one of the most promising is ZnO. The technological potential of this material in novel photonic and optoelectronic devices is great. Properties such as a large band-gap and strong exciton binding energy make ZnO an ideal candidate for technologies such as photovoltaics and blue light-emitting diodes. In addition to its technological relevance, ZnO has several key qualities that made it amenable to the experiments described in this dissertation. In particular: 1) It has a high potential for synthetic manipulation, with a

variety of nano- and micro-scale shapes, including nanoparticles, nanowires, ribbons and more complicated tetrapod and flower-shaped structures. 2) Wet chemistry methods can produce single crystal wires with length scales ranging from nanometers to microns, the larger of which are well-matched for the microscopy projects proposed herein. 3) ZnO nanowires have a large  $\chi^{(2)}$ , resulting in efficient SHG, a large two-photon cross-section that provides flexibility in experimental design, and are photochemically robust enabling them to withstand intense optical fields.

Using a home-built two-photon microscope, we explored how changes in shape within a single needle-like ZnO structure can affect trap state dynamics and the formation of an electron-hole plasma. Analysis of trap emission decays revealed a time-dependent spectral red shift in the trap band during the first 10-15 ns after photoexcitation, with a majority of the shift occurring at early times. We attributed these observations to a high DAP density that gives rise to differing recombination rates. Following annealing, we observed a blue-shift in the spectral maximum of the steady-state trap band as well as a reduction in the trap emission intensity. We proposed several models to explain this behavior (Chapter 4).

Monitoring the photophysical changes in single structures annealed at different temperatures enabled us to characterize the nature of the defects giving rise to the trap emission in ZnO. Comparison of the trap emission kinetics at different regions within a structure revealed markedly different behavior, with a rapid blue-shift in the middle of the rod compared to a slower change at the end that is smaller in magnitude. We propose that these differences are ultimately due to decreased material volume at the end of the structure, which hinders carrier migration and increases surface interactions. Our initial studies, comparing the structure surface with the bulk show that the static spectrum is red-shifted at

the surface relative to the interior. Our results show that different regions in a single structure can have differing effects on the trapping dynamics of carriers and this is ultimately due to local object shape (Chapter 5).

The dependence of ZnO band-edge emission on excitation intensity has been characterized and attributed to collisions between a high density of excitons that eventually lead to the formation of an EHP. While this observation has been described by several groups, to our knowledge, this is the first report that details the dependence of EHP formation on local object shape. Our results suggest that this process is more efficient at the end of the structure than the middle, due to a greater propensity of light to couple into optical cavity modes and the decreased volume in this region. While we generally do not observe stimulated emission in the results reported here, data from a few of the analyzed structures suggest this is possible (Chapter 6).

Given the various nanostructure shapes currently described in the literature, the observations reported herein suggest that local regions within a single object can influence recombination dynamics and result in a spatial variation of carrier behavior across a structure. The characterization of intra-object heterogeneity is fundamentally important to many problems in nanoscience and nanotechnology and will ultimately have broad implications to the understanding of nanodevice performance. Therefore, understanding these issues requires that we forge a connection between the dynamics exhibited by an object and its underlying shape. The experiments described in this dissertation are an initial step towards accomplishing this goal. Future work conducted in the Papanikolas group will continue to explore this phenomenon using novel techniques and a variety of technologically relevant materials. The results from these experiments will have a broad impact on our fundamental

understanding of defects in semiconductor nanocrystals and how their presence can impact the role of these materials in novel devices.